UNIVERSIDADE FEDERAL DE MINAS GERAIS
Escola de Engenharia
Programa de Pós-Graduação em Engenharia Metalúrgica, Materiais e de Minas

Felipe Missagia dos Anjos Cardoso

ASSESSMENT OF THROUGH-THICKNESS VARIATIONS IN HYDROGEN EMBRITTLEMENT BEHAVIOR OF API 5L X65 AND X70 PIPELINE STEELS

Belo Horizonte
2025

Felipe Missagia dos Anjos Cardoso

ASSESSMENT OF THROUGH-THICKNESS VARIATIONS IN HYDROGEN EMBRITTLEMENT BEHAVIOR OF API 5L X65 AND X70 PIPELINE STEELS

Versão Final

Dissertação apresentada ao Programa de Pós-Graduação em Engenharia Metalúrgica, Materiais e de Minas da Escola de Engenharia da Universidade Federal de Minas Gerais, como requisito parcial para obtenção do Grau de Mestre em Engenharia Metalúrgica, Materiais e de Minas

Área de concentração: Metalurgia Física

Orientadora: Prof. Augusta Cerceau Isaac Neta

Belo Horizonte
2025

C268a

Cardoso, Felipe Missagia dos Anjos.
Assessment of through-thickness variations in hydrogen embrittlement behavior of API 5L X65 and X70 Pipeline Steels [recurso eletrônico] / Felipe Missagia dos Anjos Cardoso. – 2025.
1 recurso online (105 f. : il., color.) : pdf.

Orientadora: Augusta Cerceau Isaac Neta.

Dissertação (mestrado) - Universidade Federal de Minas Gerais, Escola de Engenharia.

Bibliografia: f. 99-105.
Exigências do sistema: Adobe Acrobat Reader.

1. Engenharia metalúrgica - Teses. 2. Metalurgia física - Teses. 3. Aço - Teses. 4. Hidrogênio - Teses. 5. Eletroquímica - Teses. I. Isaac Neta, Augusta Cerceau. II. Universidade Federal de Minas Gerais. Escola de Engenharia. III. Título.

CDU: 669(043)

Ficha catalográfica elaborada pela Bibliotecária Ângela Cristina Silva CRB/6 2361
Biblioteca Prof. Mário Werneck, Escola de Engenharia da UFMG

UNIVERSIDADE FEDERAL DE MINAS GERAIS
ENGENHARIA - COLEGIADO DE PÓS-GRADUAÇÃO EM ENGENHARIA METALÚRGICA MATERIAIS E DE MINAS - SECRETARIA

ATA DE DEFESA DE DISSERTAÇÃO

Às 9h horas do dia 08 (oito) de agosto de 2025, na sala 2240 do Bloco II do Prédio da Escola de Engenharia da UFMG, realizou-se a sessão pública da defesa de dissertação de Mestrado do aluno Felipe Missagia dos Anjos Cardoso, para a obtenção do grau de Mestre em Engenharia Metalúrgica, Materiais e de Minas, na área de concentração de Metalurgia Física e de Transformação. A presidente da sessão, Profª Augusta Cerceau Isaac Neta, orientadora do aluno, apresentou a comissão examinadora, composta pelos seguintes membros: Luciano Andrey Montoro - Dr. (UFMG) e Daniel Bojikian Matsubara - Dr. (Gerdau Ouro Branco). Na sequência, o candidato realizou a apresentação de sua Dissertação de Mestrado, intitulada "Assessment of Through-thickness Variations in Hydrogen Embrittlement Behavior of Api 5l X65 and X70 Pipeline Steels". Após a apresentação, os examinadores procederam à arguição do candidato. Concluída essa etapa, a comissão reuniu-se em caráter reservado, sem a presença do candidato e do público, e decidiu por APROVAR a Dissertação de Mestrado. O resultado foi comunicado publicamente ao candidato pelo presidente da sessão. Não havendo mais nada a tratar, o presidente encerrou a sessão e lavrou a presente ata, que, após lida, foi assinada pelos membros da comissão examinadora e pelo coordenador do Programa.

Belo Horizonte, 08 de agosto de 2025.

Assinatura dos membros da banca examinadora:

Documento assinado eletronicamente por **Luciano Andrey Montoro**, **Professor do Magistério Superior**, em 12/08/2025, às 10:59, conforme horário oficial de Brasília, com fundamento no art. 5º do Decreto nº 10.543, de 13 de novembro de 2020.

Documento assinado eletronicamente por **Augusta Cerceau Isaac Neta**, **Professora do Magistério Superior**, em 12/08/2025, às 13:55, conforme horário oficial de Brasília, com fundamento no art. 5º do Decreto nº 10.543, de 13 de novembro de 2020.

Documento assinado eletronicamente por **Daniel Bojikian Matsubara**, **Usuário Externo**, em 13/08/2025, às 08:56, conforme horário oficial de Brasília, com fundamento no art. 5º do Decreto nº 10.543, de 13 de novembro de 2020.

Documento assinado eletronicamente por **Eduardo Henrique Martins Nunes**, **Coordenador(a) de curso de pós-graduação**, em 10/11/2025, às 13:02, conforme horário oficial de Brasília, com fundamento no art. 5º do Decreto nº 10.543, de 13 de novembro de 2020.

---

acao=documento_conferir&id_orgao_acesso_externo=0, informando o código verificador **4431246** e o código CRC **967760A1**.

Dedicatória

Ao meu cão, Pepe, por me trazer carinho
em momentos de desalento.

RESUMO

Os aços microligados de alta resistência (HSLA) da classe API são amplamente utilizados na fabricação de dutos destinados ao transporte de petróleo e gás contendo compostos agressivos, como o gás sulfeto de hidrogênio (H_2S). Nesses ambientes, a fragilização por hidrogênio (HE) representa um risco significativo à integridade estrutural, podendo levar à falha prematura dos componentes. Este estudo avaliou a suscetibilidade à fragilização por hidrogênio de três variantes do aço API 5L X65 e de um aço API 5L X70, com foco na influência da microestrutura ao longo da espessura de chapas grossas (32 mm). As microestruturas foram caracterizadas por microscopia óptica e eletrônica de varredura em diferentes posições através da espessura (superfície, ¼ de espessura e meio da espessura). O comportamento de transporte de hidrogênio foi avaliado por ensaios de permeação eletroquímica, a partir dos quais se determinaram a difusividade efetiva (D_{eff}) e a concentração aparente de hidrogênio subsuperficial (C_0). Ensaios padronizados de trincamento induzido por hidrogênio (HIC) e de tração em baixa taxa de deformação (SSRT) foram realizados em condições com e sem carregamento de hidrogênio. Os três aços X65 apresentaram microestruturas ferríticas relativamente homogêneas ao longo da espessura, resultando em comportamento de permeação estável (com pouca variação de D_{eff} e C_0) e boa resistência à fragilização por hidrogênio: não foram detectadas trincas por HIC e o carregamento de hidrogênio produziu apenas efeitos secundários nas propriedades mecânicas. Em contraste, o aço X70 exibiu forte segregação central de Mn, matriz bainítica granular com constituintes martensita-austenita (M/A) na região central, redução acentuada em D_{eff} e aumento em C_0 nessa região. Essa microestrutura atuou como sítio de aprisionamento de hidrogênio e de iniciação de trincas, levando a intensa fragilização e redução da ductilidade sob exposição ao hidrogênio. Este estudo ressalta a importância do controle microestrutural e da minimização da segregação química no desenvolvimento de aços com maior resistência à fragilização por hidrogênio, especialmente para aplicações em ambientes contendo H_2S e ricos em hidrogênio. Além das aplicações convencionais, esta pesquisa possui relevância disruptiva no contexto do transporte de hidrogênio verde, um dos principais desafios da transição energética global. Um aspecto crítico reside em fornecer amostras homogêneas em termos de suscetibilidade à fragilização por hidrogênio, considerando que heterogeneidades podem ocorrer não apenas entre diferentes aços, mas também dentro de um mesmo aço ao longo de sua espessura.

Palavras-chave: fragilização por hidrogênio; aços API 5L; microestrutura; SSRT; permeação eletroquímica.

ABSTRACT

High-strength low-alloy (HSLA) steels of the API grade are widely used in the manufacturing of pipelines for transporting oil and gas containing aggressive compounds such as hydrogen sulfide gas (H_2S). In such environments, hydrogen embrittlement (HE) poses a significant risk to structural integrity, potentially leading to premature component failure. This study evaluated the hydrogen embrittlement susceptibility of three API 5L X65 steel variants and one API 5L X70 steel, with a focus on the influence of microstructure through the thickness of steel plates (32 mm thick). The microstructures were characterized using optical and scanning electron microscopy at different through-thickness positions (surface, ¼-thickness, and mid-thickness). Hydrogen transport behavior was assessed through electrochemical permeation tests, from which effective diffusivity (D_{eff}) and apparent subsurface hydrogen concentration (C_0) were determined. Standard hydrogen-induced cracking (HIC) tests and slow strain rate tensile (SSRT) tests were conducted under both hydrogen-charged and uncharged conditions. The three X65 steels exhibited relatively homogeneous ferritic microstructures through the thickness, resulting in stable permeation behavior (with little variation in D_{eff} and C_0) and good resistance to hydrogen embrittlement: no significant HIC was detected, and hydrogen charging produced only minor effects on mechanical properties. In contrast, the X70 steel showed strong central Mn segregation, a granular bainitic matrix with martensite-austenite (M/A) constituents at mid-thickness, a pronounced decrease in Deff, and an increase in C_0 in that region. This microstructure acted as hydrogen traps and crack initiation sites, leading to severe cracking and reduced ductility under hydrogen exposure. This study highlights the importance of microstructural control and the minimization of chemical segregation in the development of steels with improved hydrogen embrittlement resistance, especially for applications in H_2S-containing and hydrogen-rich environments. Beyond conventional applications, this research carries disruptive relevance in the context of green hydrogen transportation, a key frontier in the global energy transition. One of the main challenges lies in providing homogeneous samples in terms of hydrogen embrittlement susceptibility, as significant heterogeneities may exist not only between different steels but also within the same steel along its thickness.

Keywords: hydrogen embrittlement; API 5L steels; microstructure; SSRT; electrochemical permeation.

Lista de Figuras

Lista de tabelas

Lista de abreviaturas

A	Ampere
A	Area
A_0	Initial area
A_F	Final area
AF	Acicular ferrite
AIDE	Adsorption-Induced Dislocation Emission
Ag	Silver
AgCl	Silver chloride
API 5L	American Petroleum Institute specification for line pipe
ASTM	American Society for Testing and Materials
B_S	Bainite start temperature
BCC	Body Centered Cubic
CE	Carbon Equivalent
C_L	Concentration of lattice hydrogen
Cr	Cromium
C_T	Trapped hydrogen concentration
C_0	Hydrogen concentration at the charging surface
DS	Devanathan–Stachurski cell
D_{eff}	Effective hydrogen diffusion coefficient
D_L	Lattice hydrogen diffusion coefficient
DLB	Degenerate Lower Bainite
DUB	Degenerate Upper Bainite
Eq.	Equation
E_a	Activation energy for hydrogen diffusion
E_t	Binding energy of trapping sites
E_D	Hydrogen desorption energy
E_S	Hydrogen solution energy in the lattice
EDS	Energy Dispersive X-ray Spectroscopy
EBSD	Electron Backscatter Diffraction
f_C	Carbon fraction
f_{Cu}	Copper fraction
f_{Mo}	Molybdenum fraction
f_{Ni}	Nickel fraction
f_{Mn}	Manganese fraction
Fe–ε	Iron Epsilon
Fe	Iron
F	Faraday’s constant

g	Gram
GB	Grain Boundary
HEDE	Hydrogen-Enhanced Decohesion
HELP	Hydrogen-Enhanced Localized Plasticity
HESIV	Hydrogen-Enhanced Strain-Induced Vacancy Formation
H	Hydrogen
H_2	Hydrogen gas
Hg	Mercury
HgO	Mercury(II) oxide
HSLA	High-Strength Low-Alloy steel
H_2S	Hydrogen Sulfide
HE	Hydrogen Embrittlement
HIC	Hydrogen-Induced Cracking
H_2SO_4	Sulfuric Acid
HTP	High-Temperature Processing
h_p	Final rolling thickness
HV	Vickers Hardness
ID	Inside Diameter
I_{ss}	Steady-state hydrogen permeation current
kJ	Kilojoule
K	Degrees Kelvin
L	Liter
L	Length
L_0	Initial lenght
LB	Lower Bainite
Log	Base-10 logarithm function
Mo	Molybdenum
mL	Millilitre
M	Molar
M/A	Martensite–Austenite constituent
mA	Milliampere
mm	Millimetre
Mn	Manganese
MPa	Megapascal
N_T	Density of trapping sites
Nb	Niobium
N_2	Nitrogen gas
Nb[C + (12/14)N]	Niobium carbonitride
NaCl	Sodium chloride

Ni	Nickel
NaOH	Sodium hydroxide
NVC	Nanovoid Coalescence
NbC	Niobium Carbide
OM	Optical Microscopy
OD	Outside Diameter
PF	Polygonal Ferrite
psi	Pound per square inch
pH	Negative logarithm of hydrogen ion concentration
Pd	Defect pressure
QPF	Quasi Polygonal Ferrite
R	Gas Constant
RA	Reduction of Area
s	Second
Si	Silicon
$\sinh^{-1}$	Inverse hyperbolic sine function
SiC	Silicon Carbide
SEM	Scanning Electron Microscope
SSRT	Slow Strain Rate Test
SWC	Stepwise Cracking
T	Temperature
Ti	Titanium
(Ti,Nb)(C,N)	Complex carbonitride
T_{nr}	Non-recrystallization temperature of austenite during hot rolling (°C)
T_{A3}	Austenite-to-ferrite transformation start temperature (°C)
TEM	Transmission Electron Microscopy
TDS	Thermal Desorption Spectroscopy
TRIP	Transformation-Induced Plasticity
TMCP	Thermomechanical Controlled Processing
t_L	Time lag in hydrogen permeation
UB	Upper Bainite
UFMG	Federal University of Minas Gerais
US	Ultrasonic scanning
UTS	Ultimate Tensile Strength
V	Vanadium
VC	Vanadium Carbide
V_H	Partial molar volume of hydrogen
wt.%	Weight percent
YS	Yield strenght

θ_L	Fraction of occupied lattice sites
°C	Celsius degrees
°	Angular degree
σ_h	Hydrostatic stress (MPa)
ε_p	Equivalent plastic strain
∇	Divergence operator in vector calculus
∂t	Partial derivative with respect to time
∂	Partial-derivative operator
$\Delta t_{8/5}$	time taken to cool the microstructure from 800°C to 500°C
µm	Micrometre
µA	Microampere
¼-T	One-quarter thickness location in a plate
½-T	Mid-thickness location in a plate

Sumário

1.INTRODUCTION

The use of petroleum as a source of energy and chemical compounds necessitates its transportation from regions with active oil wells to refineries, where the crude oil is distilled into byproducts such as gasoline, kerosene, diesel oil, asphalt, and other derivatives.

New oil reserves, such as those in the pre-salt fields on the Brazilian coast, contain high levels of hydrogen sulfide, a compound that, when in contact with the water used to reduce the viscosity of oil in pipelines, creates an acidic environment capable of reacting with the inner surface of the pipes and producing hydrogen gas.

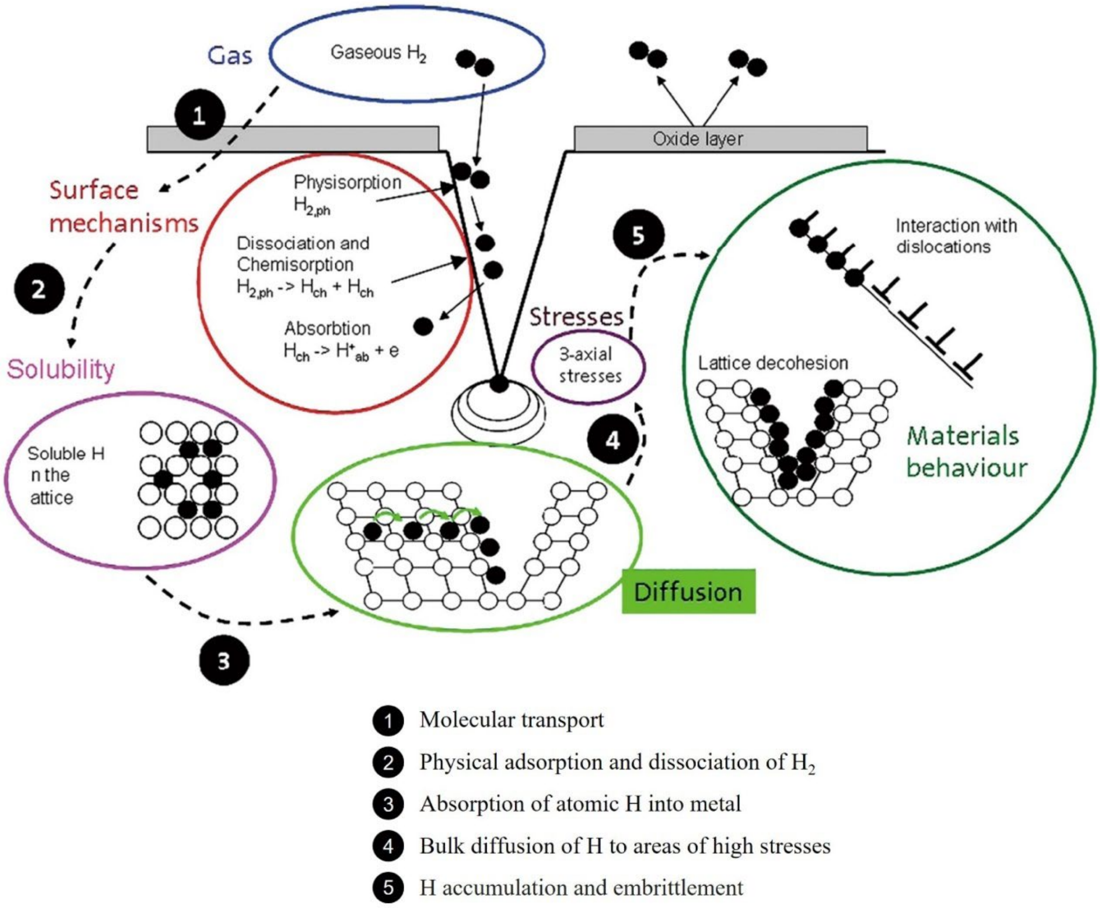

Figure 1.1 – H path from gaseous phase to interaction with dislocations, passing through physisorption, dissociation, absorption and diffusion. [1]

The hydrogen generated by the reactions of hydrogen sulfide with water and steel in the pipelines is adsorbed on the inner wall and dissociates into atomic hydrogen, process shown on figure 1.1. Hydrogen sulfide acts as a poison for the recombination of dissociated atomic hydrogen into H_2, stabilizing the atomic form of the element and promoting its diffusion in the ferrite lattice. While in solid solution, the H atoms promote hydrogen embrittlement, a phenomenon in which the mechanical properties of the metal are affected and fracture conditions are modified [1].

$$\frac{C_L+C_T(1-\theta_T)}{C_L}\frac{\partial C_L}{\partial t} - \nabla \cdot (D_L \nabla C_L) + \nabla \cdot \left(\frac{D_L C_L V_H}{RT}\nabla \sigma_h\right) + \theta_T \frac{dN_T}{d\varepsilon_p}\frac{\partial \varepsilon_p}{\partial t} = 0 \qquad [1.1]$$

The model of Krom and Bakker [2] shown in equation 1.1 is based on the balance between lattice and trapped hydrogen, and on hydrogen transport driven by concentration gradients, stress triaxiality and plastic strain rate. where C_L and C_T are lattice and trapped hydrogen concentration, t represents time, θ_T is the occupancy of hydrogen on trapping sites, θ_L is the occupancy of lattice sites, D_L is the lattice diffusion coefficient, V_H the partial molar volume of hydrogen in hydrogen in solid solution (2.103 mm^3/mol for iron based alloys, R is the gas constant (8.314 J/mol.K), T absolute temperature, σ_h is hydrostatic stress ($\sigma_{ii}/3$), ε_p is equivalent plastic strain and N_T the number of hydrogen traps per unit volume.

$$\frac{C_L+C_T(1-\theta_T)}{C_L}\frac{\partial C_L}{\partial t} \qquad [1.2]$$

The term 1.2 represents the temporal variation of the total hydrogen concentration (in both the crystal lattice and the trapping sites), expressed as a function of the lattice concentration. The factor (C_L +C_T(1-θ_T))/C_L arises from the Oriani equilibrium [3] between the two types of sites. It accounts for the relative contribution of mobile atoms (in solid solution) and trapped atoms (non-diffusive).

$$-\nabla \cdot (D_L \nabla C_L) \qquad [1.3]$$

The term 1.3 term corresponds to the traditional diffusive flux of hydrogen in solid solution, governed by the concentration gradient, that is, hydrogen tends to migrate from regions of high concentration to regions of low concentration.

$$+\nabla \cdot \left(\frac{D_L C_L V_H}{RT}\nabla \sigma_h\right) \qquad [1.4]$$

This term represents the migration of hydrogen induced by hydrostatic stress gradients. Physically, this term expresses the fact that hydrogen atoms are attracted to regions under tensile stress (where the chemical potential is lower). Thus, near a crack tip, hydrogen tends to accumulate in areas experiencing the highest tensile stresses. It was originally developed by Sofronis and McMeeking[4], derived from the expression of the chemical potential of hydrogen in a stressed solid, showing that tensile hydrostatic stress lowers the chemical potential, thus attracting hydrogen atoms toward regions of high triaxiality.

$$+\theta_T \frac{dN_T}{d\varepsilon_p} \frac{\partial \varepsilon_p}{\partial t} \qquad [1.5]$$

This is the additional term introduced by Krom and Bakker [2] commonly referred to as the plastic strain rate term. During plastic deformation, new trapping sites are continuously created, such as dislocations, vacancies, and grain boundaries. This term describes the flux of hydrogen from the lattice to newly formed traps, meaning that it consumes mobile hydrogen as the material plastically deforms. Without this term, the original model proposed by Sofronis and McMeeking [3] would not conserve mass hydrogen would artificially "appear" in the system as a numerical artifact, an inconsistency later corrected by Krom and Bakker [2].

The presence of hydrogen in solid solution at high concentrations, combined with the presence of internal stresses and the microstructure, leads to the formation of H_2 bubbles at the interface between the ferritic matrix and inclusions with high affinity for H[5]. These bubbles grow due to the recombination of H atoms into H_2 at the particle-matrix interface. High pressure is generated by the gaseous hydrogen formed, which causes a crack to nucleate and grow, eventually combining with other cracks, in a phenomenon known as Hydrogen Induced Cracking (HIC).

Hydrogen diffusion in metals can be evaluated through hydrogen permeation testing using a Devanathan–Stachurski (DS) cell, following the standards ISO 17081 [6] and ASTM G148 [7]. The DS setup consists of a double-cell apparatus in which the metal specimen (the permeation membrane) is placed between two electrolytic chambers. In the cathodic cell, hydrogen is introduced onto one side of the sample via electrochemical charging. At this surface, hydrogen atoms are adsorbed and subsequently enter the metal. These atoms then diffuse through the membrane and reach the opposite side, located in the anodic cell, where they are oxidized. The anodic side acts as the detection zone, where the hydrogen flux is quantitatively measured.

To assess the susceptibility of a metal to hydrogen embrittlement (HE), Slow Strain Rate Tensile (SSRT) tests can be performed according to ASTM A370 [8], in conjunction with ex-situ electrochemical hydrogen charging. The effects of HE on the fracture behavior of tested samples can be investigated via fractographic analysis. Characteristic features of hydrogen-assisted cracking-such as quasi-cleavage, microvoid coalescence, and intergranular fracture-may be identified [9]. Additionally, variations in mechanical properties, including yield strength, ultimate tensile strength, and total elongation, can be evaluated by comparing charged and uncharged specimens.

The hydrogen permeation procedure described in ISO 17081 [6] and ASTM G148 [7] provides a standardized electrochemical method for evaluating hydrogen uptake, transport, and diffusivity in metallic materials. This technique enables the quantification of key parameters such as the apparent diffusion coefficient of hydrogen, the maximum hydrogen solubility, and the density of hydrogen traps, based on controlled test conditions and electrochemical measurements.

During the rolling process of pipeline steels, the surface and central layers are subjected to non-uniform thermal and mechanical conditions, resulting in heterogeneous heating and deformation along the normal direction of the plate [10]. This inhomogeneity gives rise to variations in microstructure and stress/strain states across the thickness, which in turn influence the hydrogen permeation behavior in different layers. The primary objective of this study is to evaluate the influence of microstructural features and strain states at various depths on the hydrogen permeation behavior of rolled X65 and X70 pipeline steels.

This study aims to establish a correlation between microstructural features and the resistance of the studied steels to hydrogen-induced cracking and hydrogen embrittlement. Microstructural characterization will be performed using optical microscopy and scanning electron microscopy (SEM) on specimens subjected to testing according to the NACE TM0284 [11] standard, using NACE A solution.

2. OBJECTIVES

The primary objective of this study was to investigate the through-thickness variation in hydrogen embrittlement susceptibility of three API 5L X65 pipeline steels and one API 5L X70 pipeline steel. To achieve this, the study aimed to:

- Characterize the microstructural features across different thickness positions (near-surface, one-quarter thickness, and mid-thickness) of the steels using optical and scanning electron microscopy.

- Assess hydrogen transport behavior by measuring effective hydrogen diffusivity (D_{eff}) and apparent subsurface hydrogen concentration (C_0) through electrochemical permeation tests.

- Evaluate the susceptibility to hydrogen-induced cracking (HIC) via standard HIC testing protocols and correlate cracking behavior with microstructural and chemical characteristics.

- Analyze the mechanical response under hydrogen charging conditions through slow strain rate tensile (SSRT) testing, comparing the mechanical performance of hydrogen-charged and uncharged specimens.

- Establish correlations between microstructural attributes, hydrogen permeation properties, mechanical behavior, and cracking susceptibility, highlighting the role of microstructural in hydrogen embrittlement resistance.

Ultimately, the study seeks to provide insights into the key microstructural factors governing hydrogen resistance in high-strength pipeline steels and to guide the development of materials with enhanced durability in hydrogen-containing environments.

3. LITERATURE REVIEW

3.1. High-Strength Low-Alloy Steels

High-strength low-alloy (HSLA) steels are characterized by a unique combination of high mechanical strength, high tensile strength, good ductility, uniform elongation, good weldability, cost-effectiveness, and high strength-to-weight ratio. This class of steel was developed in the 1970s to produce large-diameter pipelines in the United States and have since been used in various industries, such as automotive, heavy equipment, wind power, shipbuilding, pressure vessels, and structural construction. HSLA steels are designed to have a minimum mechanical strength of 275 MPa [12], with significant variations in chemical composition allowed for specific standards, if the minimum and maximum tensile strength and yield strength requirements are met.

The steel plates used for manufacturing large-diameter pipes are high-value semi-finished products resulting from extensive industrial research. The alloy design of these steels aims to achieve high mechanical strength, ductility, good weldability, and superior corrosion resistance compared to carbon steels. This is accomplished by maintaining carbon levels below 0.1%, adding Mn, Mo, Ni, and Cr, microalloying with Nb, Ti, and V, controlling non-metallic inclusions, and employing desulfurization and dephosphorization processes.

Once cast, the slabs undergo a hot rolling process under thermomechanical control. The purpose of this process is to refine ferritic grains, achieved through the anchoring of austenitic grains by niobium carbonitride particles during finishing passes. Higher-strength steels are subjected to accelerated cooling by water spraying after rolling, a process that inhibits grain growth during cooling and promotes the transformation of austenite into bainite [13;14].

Heterogeneities in the microstructure of semi-finished products mainly originate from two stages: continuous casting and thermomechanically controlled rolling. During continuous casting, Fe-ε dendrites grow from the mold zone toward the center of the ingot, resulting in the segregation of elements such as Mn, P, and S into interdendritic and central regions. As carbon is practically insoluble in iron at low temperatures, it segregates into Mn-rich regions, leading to the formation of banded regions in the material's structure [15;16].

Hot rolling deforms austenitic grains anisotropically, elongating them in the rolling direction while maintaining their equiaxed shape in the width and thickness directions of the plate.

Although the transformation of austenite into ferrite promotes microstructural rearrangement due to nucleation and growth, anisotropic features remain in the final microstructure, such as prior austenitic boundaries, elongated inclusions, fragmented inclusions during rolling, and banding.

3.2. Thermomechanically Controlled Rolling

Thermomechanically controlled rolling (TMCP) is a rolling process for low-carbon steels microalloyed with niobium, where the load and temperature of each pass are designed based on process temperatures, niobium carbonitride solubilization temperature, non-recrystallization temperature, and the start temperature of austenite-to-ferrite transformation, as determined by the steel composition.

The solubility of carbonitrides with the formula Nb[C + (12/14)N] in steel is given by Equation 3.1, where M is the mass fraction of Nb, I is the mass fraction of C, and T is the absolute temperature [17]. Based on this equilibrium equation, the minimum temperature to which the slab must be heated before rolling can be calculated, ensuring that all carbonitride particles formed during continuous casting are solubilized.

$$Log([M][I]) = 2{,}26 - \frac{6670}{T} \tag{3.1}$$

The rolling passes are divided into two stages: roughing passes and finishing passes. During roughing, the passes are performed at temperatures above the non-recrystallization temperature, T_{nr}, given by Equation 3.2 [18], which relates to the mass fractions of alloying elements in the steels. With each pass in this stage, new austenite grains are nucleated and grow until the application of the next pass. The time between passes is kept as short as possible to ensure a reduction in grain size with each pass. After these passes, the plate is air-cooled until the entire material cools below the T_{nr}.

$$T_{nr} = 897 + 464f_c + \left(6446f_{Nb} - 644\sqrt{f_{Nb}}\right) + (732f_V - 320f_V) + 890f_{Ti} + 363f_{Al} - 357f_{S_i} \tag{3.2}$$

The finishing passes are performed below the T_{nr} and above the start temperature of the austenite-to-ferrite transformation, T_{A3}, given by Equation 3.3 [19], which relates the mass fraction of alloying elements and the final rolling thickness, hp. The application of these passes causes the austenite grains to elongate in the rolling direction, creating a pancaked structure containing twins.

$$T_{A3} = 910 - 310f_C - 80f_{Mn} - 20\,f_{Cu} - 15f_{Cr} - 55f_{Ni} - 80\,f_{Mo} + 0{,}35(h_p - 8)$$
[3.3]

After the completion of all passes, the rolled plate is cooled. The cooling rate will determine the final microstructure of the plate. Plates air-cooled will consist of fine equiaxed ferrite grains, nucleated from austenitic grain boundaries and twins, as well as fine pearlite. Plates subjected to accelerated cooling through water jet spraying will exhibit a microstructure containing bainite and acicular ferrite, which may also include islands of the MA (Martensite-Austenite) constituent. The bainitic transformation occurs on a range of temperatures, bellow B_s, shown on equation 3.4 [21], under accelerated cooling. In this model, proposed by Lotter, $\Delta t_{8/5}$ is the time taken to cool the microstructure from 800°C to 500°C.

$$B_s = 809.8 - 558C - 96.4Mn + 38.7Si - 111.1Cr - 76.3Mo - 723.2Nb - 530Ti + 6.12\ sinh^{-1}\left(\Delta t_{\frac{8}{5}}\right)$$
[3.4]

In low-carbon steels developed for high-strength applications (e.g., API X100–X120 linepipe), Zajac [21] proposed a refined classification system that includes five distinct bainitic morphologies: granular bainite (GB), upper bainite (UB), degenerate upper bainite (DUB), lower bainite (LB), and degenerate lower bainite (DLB). Each type exhibits unique morphological characteristics, carbide distribution, and transformation mechanisms, often influenced by chemical composition, cooling rate, and transformation temperature.

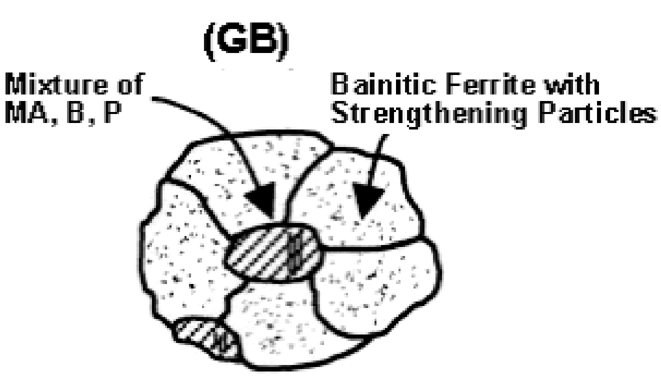

Figure 3.1 - Schematic illustration of GB morphology according to the classification by Zajac et al [21]

Granular bainite is characterized by irregular, quasi-equiaxed ferrite grains accompanied by various second-phase constituents situated between these grains. Notably, the ferrite grains lack the characteristic lath morphology seen in other bainitic types and display a dislocated substructure indicative of a diffusion-controlled growth mechanism. A defining feature of GB is the absence of intra-lath carbides, which contrasts with other bainitic forms. Instead, carbon partitioned from ferrite stabilizes residual austenite, potentially leading to subsequent transformation into martensite-austenite (MA) constituents, degenerated pearlite, or martensite depending on local conditions[21].

The morphology and volume fraction of the second phase in GB vary significantly with alloying strategy and thermal history. For instance, Mo-rich steels tend to form debris of cementite or degenerated pearlite, while high cooling rates promote fine bainitic or martensitic structures. Additionally, a previously undocumented phase—termed an “incomplete transformation product”—has been identified, comprising a chaotic mixture of fragmented ferrite, cementite, and MA constituents, particularly at the edges of irregular ferrite grains[21].

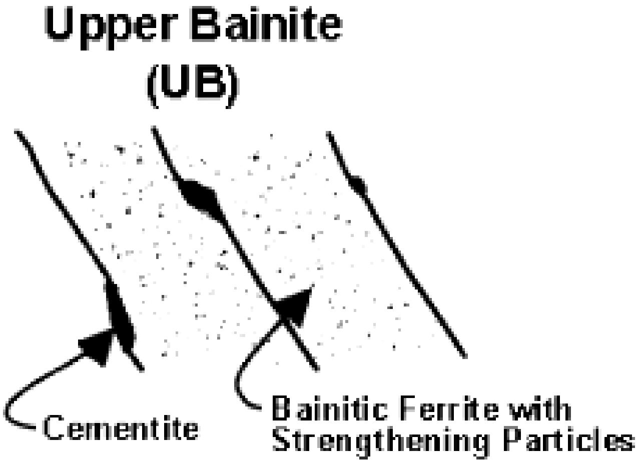

Figure 3.2 - Schematic illustration of UB morphology according to the classification by Zajac et al [21]

Upper bainite typically forms at lower transformation temperatures than GB and features lath-like ferrite arranged in packets, with cementite precipitating between laths along boundaries. The laths usually exhibit high internal dislocation densities and are aligned at 40–60° to the rolling direction. Microalloying elements such as Nb, Ti, and V may also contribute to precipitation strengthening by forming fine intra-lath carbides[21].

Degenerate upper bainite emerges when cementite precipitation is suppressed, either due to specific alloying effects or cooling paths. Its microstructure consists of lath-like ferrite with MA constituents or retained austenite located along the lath boundaries. While macroscopically similar to UB, DUB is distinguished by the absence of cementite and the presence of residual austenite or martensite islands, which can be visualized under high magnification SEM[21].

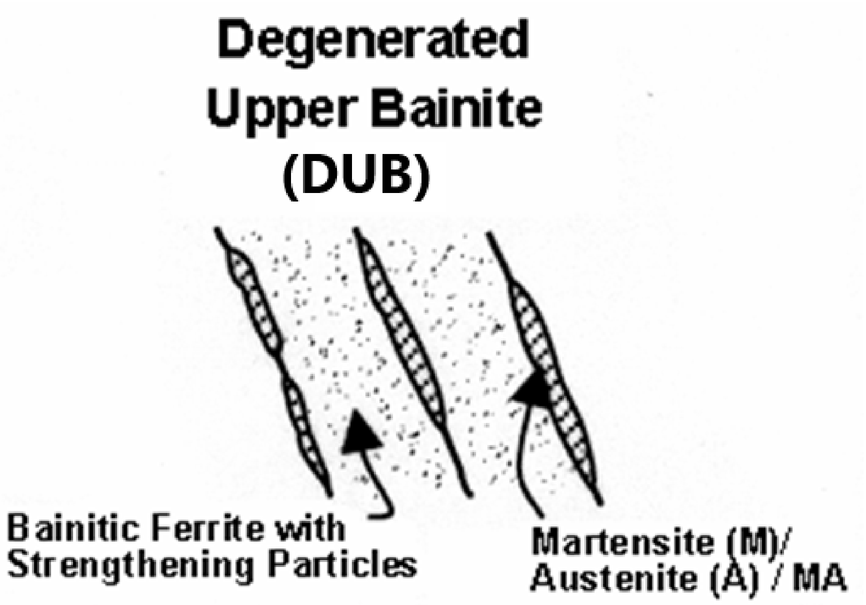

Figure 3.3 - Schematic illustration of DUB morphology according to the classification by Zajac et al [21]

Lower bainite also presents a lath morphology but differs from UB in the location of carbide precipitation. In LB, cementite precipitates intralath, typically oriented at ~60° to the growth direction of the lath. This morphology is particularly well-developed in steels with slightly higher hardenability, and the intra-lath carbides serve to reinforce mechanical strength through precipitation hardening mechanisms[21].

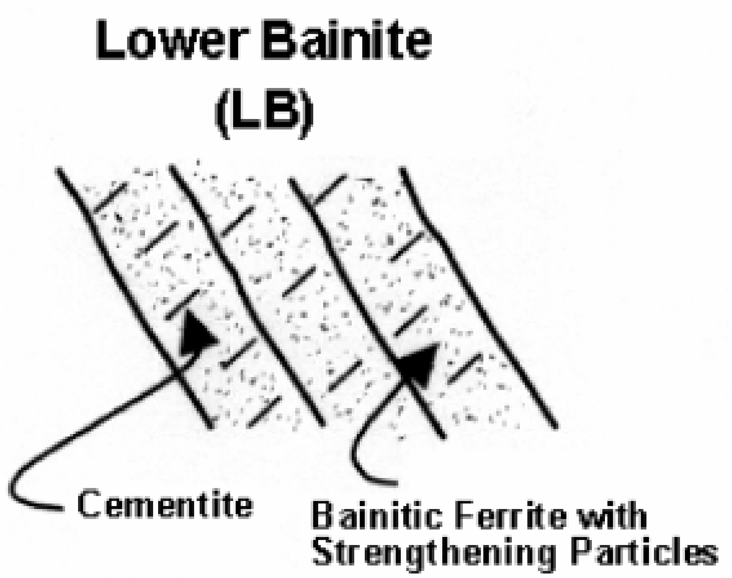

Figure 3.4 - Schematic illustration of DLB morphology according to the classification by Zajac et al [21]

Degenerate Lower Bainite is a novel microstructural class identified in complex alloy systems such as MoNiCuCrB steels. It resembles LB in its lath morphology but diverges in its carbide behavior: instead of cementite, intra-lath MA constituents are observed, indicating incomplete transformation. The suppression of cementite is attributed to altered carbon activity and kinetic factors arising from alloying. Under certain conditions, rapid transformation results in a high carbon supersaturation at the austenite-ferrite interface, favoring MA formation over cementite precipitation. As transformation rates slow, this gradient becomes less pronounced, and carbon diffusion is insufficient to nucleate cementite, solidifying the DLB morphology[21].

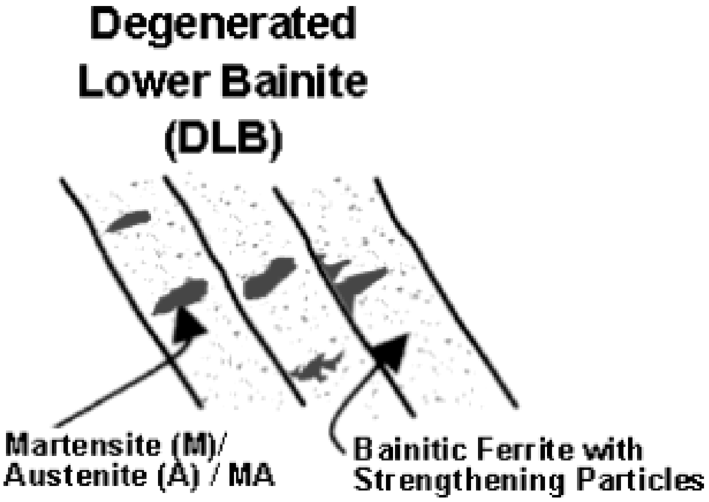

Figure 3.4 - Schematic illustration of LB morphology according to the classification by Zajac et al [20]

Acicular ferrite (AF), quasi-polygonal ferrite (QPF), and polygonal ferrite (PF) represent distinct ferritic microstructures that form under different cooling rates and transformation conditions in low-carbon steels[22]. Acicular ferrite is composed of intragranular ferrite plates that nucleate on nonmetallic inclusions within prior austenite grains, forming a fine and highly interlocked network of lenticular plates. This morphology, characterized by high dislocation density and numerous high-angle boundaries, refines the effective grain size and enhances resistance to cleavage, providing an excellent combination of strength and toughness[22]. Quasi-polygonal ferrite, in contrast, forms when austenite transforms rapidly through the two-phase ferrite–austenite field with minimal chemical partitioning. The resulting grains are relatively coarse and irregular, with serrated boundaries and internal dislocation substructures. This morphology is often associated with high strain-hardening capacity and favorable ductility in low-carbon HSLA steels. Finally, polygonal ferrite develops at higher transformation temperatures under slow cooling. It is composed of equiaxed grains with smooth, continuous boundaries and very low dislocation density, representing a fully recrystallized structure. PF typically nucleates along prior austenite grain boundaries and grows by diffusion-controlled mechanisms, resulting in a soft, ductile microstructure that contrasts with the more dislocated and irregular morphologies of AF and QPF[22].

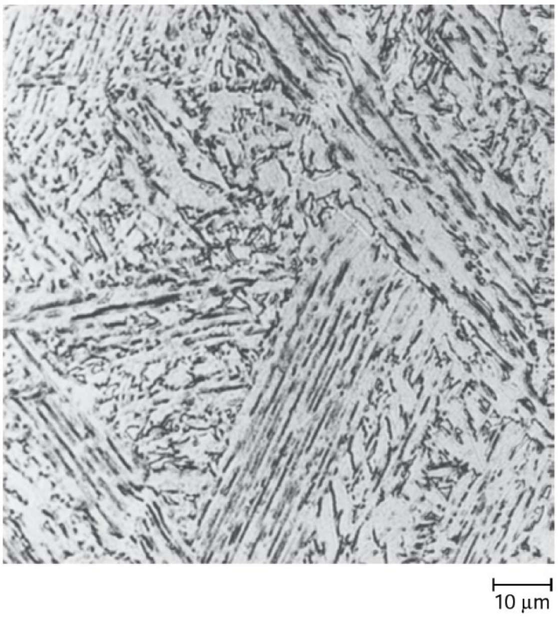

Figure 3.6 - Acicular ferrite formed by isothermal transformation of a copper containing HSLA-80 steel transformed for 5000 s at 500 °C[22]

Acicular ferrite consists of intragranular ferrite plates that nucleate on nonmetallic inclusions dispersed throughout prior austenite grains. Nucleation occurs on inclusion surfaces that present crystallographic or chemical features favourable to the ferrite–austenite interface. A single active inclusion often initiates several plates in quick succession, which gives the microstructure a highly interlocked appearance. The plates are lenticular rather than needle shaped. In three dimensions they resemble thin lenses that grow with a pronounced shape deformation. Typical plate thickness is near one micrometre and the length is on the order of several micrometres, although both dimensions increase with higher transformation temperature and with slower cooling. The aspect ratio observed in two dimensional sections underestimates the true three dimensional shape[22].

Plates form in many directions within the same prior austenite grain. Each plate adopts an orientation relationship with austenite that places a close packed plane of ferrite nearly parallel to a close packed plane of austenite, with close packed directions nearly parallel as well. Because many plates nucleate on a variety of inclusions and grow with different habit planes, the misorientation between neighbouring plates is large. This creates a three dimensional network of high angle boundaries that interrupts cleavage paths and deflects cracks[22].

Growth is displacive and accompanied by an invariant plane strain type shape change. The surrounding austenite accommodates this shape change by plastic deformation. The resulting dislocations are inherited by the ferrite as it advances, so the plates contain a high density of dislocation cells and tangles. This stored defect density contributes significantly to yield strength. During growth there is little or no long range partitioning of substitutional solutes. Carbon partitions rapidly at the advancing interface and may form very fine carbides during or after transformation, but the ferrite matrix remains essentially low in carbon[22].

The intragranular nature of acicular ferrite distinguishes it from bainitic sheaves and from grain boundary ferrite. There is no packet structure that spans multiple prior austenite grains. Instead, each grain contains a chaotic basket weave of plates with frequent intersections. This interlocking arrangement refines the effective grain size defined by high angle boundaries and increases resistance to cleavage[22].

Inclusions control both the number of nucleation events and the initial plate orientations. Complex oxide–sulfide–nitride clusters and glassy inclusions with manganese and silicon oxides are particularly potent. A single successful plate can stimulate further nucleation on or near the same inclusion, which explains why the number of plates is not simply proportional to the number of particles. The most effective inclusions are those that are small, numerous, and well dispersed, and that present crystallographic or chemical conditions that reduce the ferrite–austenite interfacial energy[22].

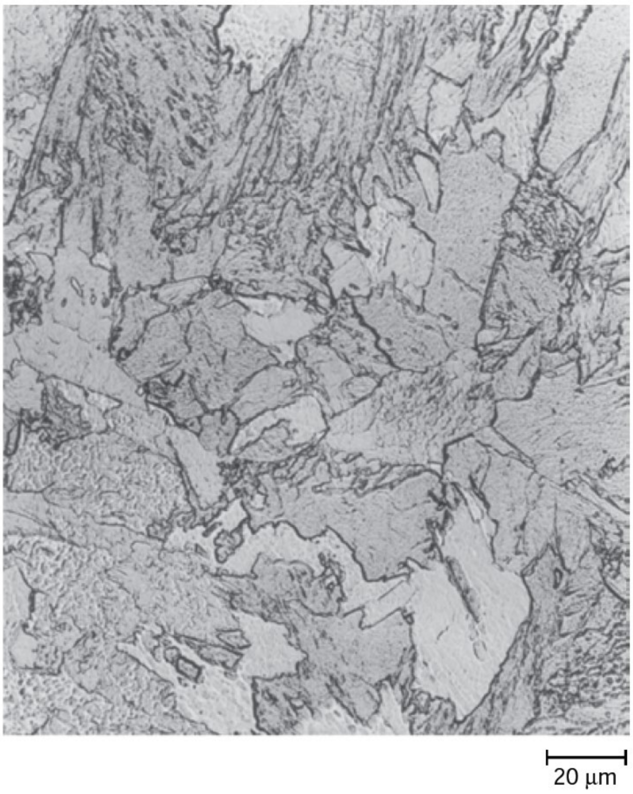

Figure 3.7 - Quasi-polygonal ferrite formed in ultra-low-carbon steel containing 0.003% C and 3.00% Mn cooled at 50°C/s [22].

Quasi polygonal ferrite forms in very low carbon steels and irons when austenite is cooled rapidly enough to pass through the two phase ferrite plus austenite field with little or no chemical partitioning. The product is therefore often described as massive ferrite. The ferrite crystals are relatively coarse, but their boundaries are not smooth. Instead they show irregular, jagged outlines and frequently reveal an internal substructure in etched sections. Individual ferrite grains commonly span prior austenite grain boundaries, which distinguishes this constituent from grain boundary allotriomorphic ferrite[22].

Ideally the parent austenite and the product ferrite have the same composition, which means that the transformation can proceed through very short range diffusion at the moving interface.

In practice, some partitioning of interstitial or substitutional solutes may still occur locally at the interface and this is thought to promote the irregular growth morphology and the serrated grain boundaries that are typical of quasi polygonal ferrite[22].

Transmission electron microscopy shows a high density of dislocations within these ferrite grains together with dislocation subboundaries. In some cases small regions of martensite austenite constituent can also be present. This internal substructure is associated with a relatively low ratio of yield strength to ultimate tensile strength and with high strain hardening rates, features that help explain why continuously cooled low carbon steels containing quasi polygonal ferrite can display attractive combinations of strength and ductility[22].

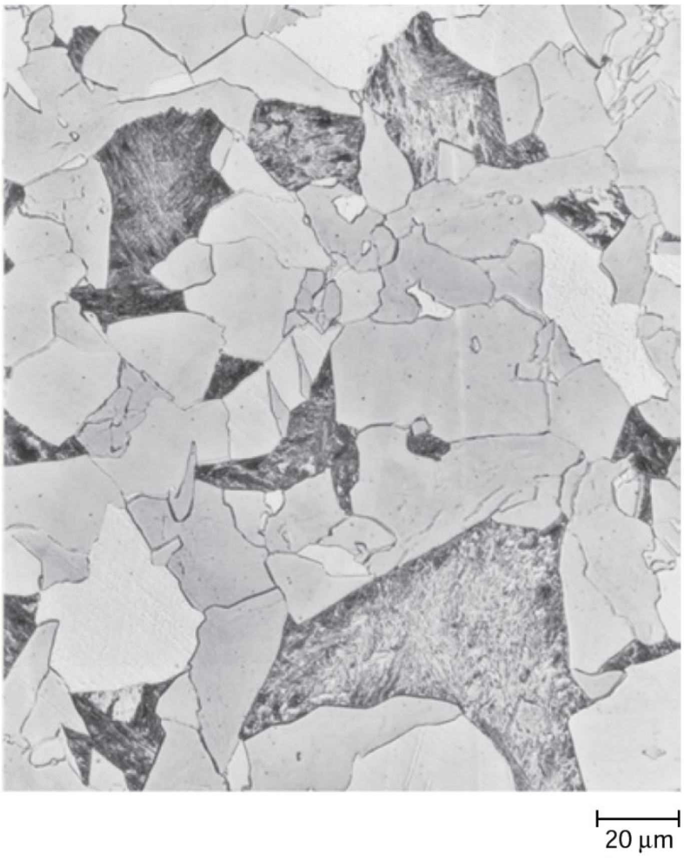

Figure 3.8 - Polygonal ferrite (light structure) formed in HSLA-80 steel isothermally transformed at 675 °C for 500 s[22].

Polygonal ferrite forms at the highest transformation temperatures under the slowest cooling conditions in low carbon steels. Nucleation begins as grain boundary allotriomorphs and the product grows into equiaxed grains. In common notations this constituent is referred to as polygonal ferrite or primary ferrite and is often labeled alpha p. The International Institute of Welding distinguishes primary ferrite that nucleates on boundaries from that which appears within grain interiors, noted as PF at grain boundaries and PF in grain interiors[22].

In light microscopy polygonal ferrite is easy to recognise because the grains are equiaxed and the boundaries appear smooth and continuous at the scale of observation. Transmission electron microscopy reveals very low dislocation density and an absence of internal substructure. After isothermal holds followed by quenching, any remaining austenite may transform to martensite, which appears as dark regions, while the ferrite grain boundaries remain smooth even when impingement produces boundary curvature. Nucleation is favoured at austenite grain corners and along prior austenite grain boundaries. Before impingement the network of grain boundary allotriomorphs outlines the parent austenite structure. Growth is controlled by rapid transfer of substitutional atoms across partially coherent boundaries and by the long-range diffusion of carbon that is rejected from the advancing ferrite. Some partitioning of substitutional alloying elements can occur at ferrite interfaces, and this segregation may reduce the growth rate of grain boundary allotriomorphs[22].

3.3 Centerline Segregation

In low-carbon low-alloy steel plates produced from continuously cast slabs, central segregation leads to chemical and microstructural heterogeneity that is typically confined to a narrow region of the plate[15][23], phenomenon represented on fig 3.1. While this heterogeneity does not significantly impact bulk mechanical properties, it introduces localized discontinuities. These discontinuities reduce mechanical performance in the Z-direction, increase the susceptibility to weld zone cracking, and, more critically for sour service applications, enhance the material's sensitivity to hydrogen-induced cracking [22;23].

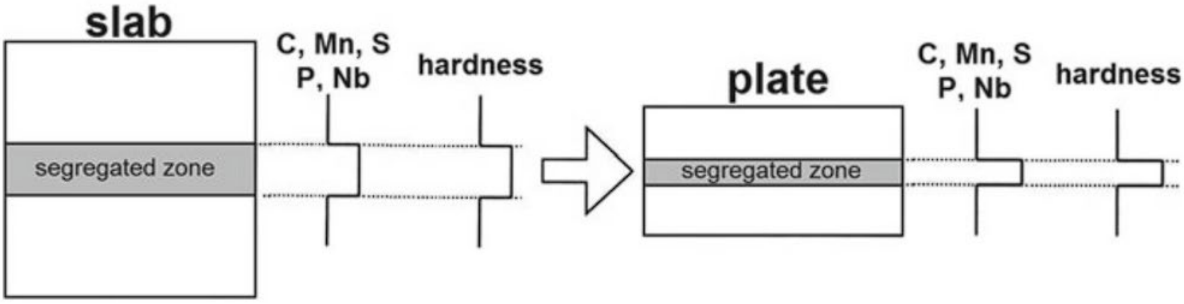

Figure 3.9 - Schematic representation of the mechanism by which centerline segregation in continuously cast slabs is inherited by the rolled steel plate. [15]

Resistance to HIC is influenced not only by chemical composition, impurity content, and non-metallic inclusions, but also by the characteristics of the microstructure formed during the final stages of plate production. Both the selection of alloying elements and the applied thermomechanical treatment have a decisive impact on the final microstructure of the base metal and on the degree of segregation and heterogeneity present in the axial zone [26-28]. To enhance HIC resistance, it is essential to reduce the negative effects of central segregation by controlling the axial zone's microstructure. This requires optimization of chemical composition and thermomechanical processing parameters during the production of rolled steel products.

Manganese is the alloying element with the highest tendency to stabilize austenite, meaning that higher levels of this element in steel will delay the bainitic reaction. In steels with a banded structure, the Mn content varies in a sinusoidal distribution along its longitudinal section. The decomposition of austenite begins in Mn-depleted regions, forming equiaxed ferrite (PF) that grows toward the Mn-rich regions. Upon reaching the bainitic transformation start temperature, the untransformed austenite regions shear, forming ferrite. Depending on the carbon content and the applied cooling rates, cementite nucleation and growth occur, leading to bainite and MA constituent formation, as shown in Figure 3.2 [29].

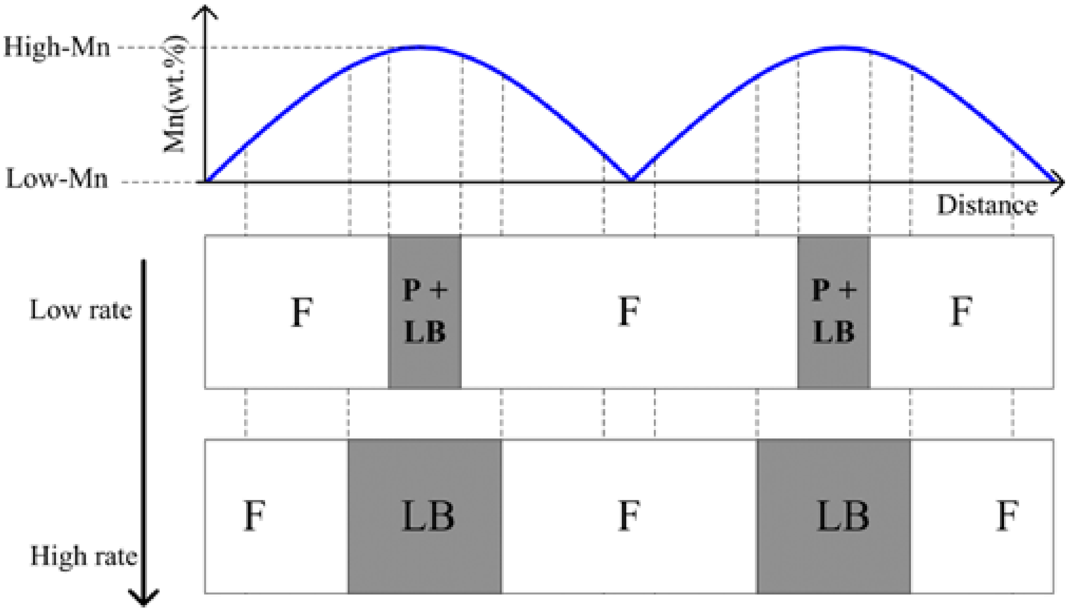

Figure 3.10 - Constituents formed during in HSLA steel during increasing cooling rates [29].

3.5 Hydrogen Embrittlement

Hydrogen embrittlement is a phenomenon in which the mechanical properties of a material are degraded due to the presence of atomic hydrogen in solid solution within its matrix phase [31;32], These changes in mechanical behavior can lead to catastrophic failure during service.

Atomic hydrogen may be introduced into the material during production, resulting in internally assisted hydrogen cracking. This form of contamination can occur during various processing stages, such as ladle operations in steelmaking, continuous casting, welding, electrochemical surface cleaning, electrodeposition, or heat treatment. Alternatively, hydrogen can enter the material from the service environment, leading to environmentally assisted hydrogen cracking. In this case, hydrogen sources may include corrosive media, cathodic protection systems, or exposure to high-pressure gaseous hydrogen [33].

3.5.1 Hydrogen-Enhanced Decohesion (HEDE)

Hydrogen-Enhanced Decohesion (HEDE) is one of the earliest proposed mechanisms to explain hydrogen embrittlement (HE) and has been widely incorporated into numerical models. Initially proposed by Pfeil in 1926 [35], the mechanism was based on the observation of brittle fracture surfaces in hydrogen-charged single-crystal and polycrystalline iron. According to HEDE, the segregation of hydrogen atoms at interfaces weakens metallic interatomic bonds, reducing the cohesive strength and leading to rupture under lower applied stress. For this to occur, a critical concentration of hydrogen must accumulate within the fracture process zone (FPZ) near the crack tip, where tensile stresses exceed the cohesive strength of the material, represented on figure 3.8.

A critical feature of HEDE is the presence of mobile hydrogen atoms, which can diffuse through the crystal lattice and along with microstructural defects. This mobility allows hydrogen to concentrate in regions subjected to high stress, particularly near crack tips, promoting localized bond weakening due to interactions between mobile hydrogen and deformation fields. HEDE is typically associated with three microstructural features: dislocation shielding regions, areas under high hydrostatic stress, and trapping sites such as grain boundaries and particle–matrix interfaces. Dislocation shielding refers to localized regions around dislocations in which hydrogen mobility is reduced or restricted. Figure 3.8 presents a schematic representation of HEDE, highlighting the weakening of interatomic bonds in three hydrogen states: (i) lattice hydrogen, (ii) adsorbed hydrogen, and (iii) hydrogen located at particle–matrix interfaces.

Experimental evidence of intergranular fracture, supported by quantum mechanics and molecular dynamics simulations [37], further corroborates the HEDE model.

3.5.2 Adsorption-Induced Dislocation Emission (AIDE)

The Adsorption-Induced Dislocation Emission (AIDE) mechanism, proposed by Lynch et al. [38], attributes hydrogen-assisted cracking to the adsorption of hydrogen atoms on the crack surface, which reduces the energy barrier for dislocation nucleation and surface step propagation. This occurs through the breaking and reforming of interatomic bonds across multiple atomic distances, thereby promoting dislocation emission, as shown on figure 3.8. A schematic representation of this mechanism is shown in Figure x. In addition to dislocation emission, the AIDE model also accounts for microvoid formation and growth as contributing factors to crack propagation.

Despite these secondary processes, dislocation emission remains the primary mechanism of crack growth in AIDE. This process is central to the plastic deformation and fracture behavior of metallic materials, as it governs dislocation nucleation, movement, and interaction within the stress field, particularly near crack tips.

In contrast to the HELP mechanism-which attributes crack advancement to enhanced dislocation mobility due to internal hydrogen-the AIDE mechanism emphasizes the role of hydrogen adsorbed externally on the crack surface in facilitating dislocation emission. This distinction highlights the significance of surface phenomena in AIDE. Atomistic simulations and surface science studies provide strong evidence in support of this mechanism [36-38].

3.5.3 Hydrogen-Enhanced Localized Plasticity (HELP)

The Hydrogen Enhanced Localized Plasticity (HELP) mechanism, initially proposed by Beachem in 1971 [39] and later developed by Birnbaum and colleagues [40], describes how hydrogen facilitates localized plastic deformation processes, such as dislocation nucleation and motion, in regions with sufficient H concentration. Although the material undergoes localized plasticity at the microscale, the overall fracture behavior remains macroscopically brittle.

As illustrated in figure. 3.8, the HELP mechanism involves the formation of a highly localized plastic zone near the crack tip, where elevated hydrogen concentrations promote the initiation and movement of dislocations. Interactions between hydrogen and dislocations have been extensively studied in the context of the HELP mechanism, offering critical insights into hydrogen-assisted fracture. Analogous to the formation of Cottrell atmospheres, hydrogen atoms bind to dislocation cores, forming a hydrogen atmosphere that is drawn into the surrounding elastic stress field [41].

Under certain conditions, this hydrogen atmosphere enhances dislocation mobility, facilitating their motion. This phenomenon has been experimentally observed and documented in various studies [40;41]. Specifically, in edge dislocations, hydrogen alters the dislocation stress field, creating a shielding effect that lowers the interaction energy between dislocations and thus promotes increased mobility

3.5.4 Hydrogen-Enhanced Strain-Induced Vacancies (HESIV)

The Hydrogen-Enhanced Strain-Induced Vacancy (HESIV) mechanism proposes a synergistic interaction between hydrogen and the generation of vacancies induced by plastic deformation in metals and alloys. The presence of hydrogen promotes dislocation motion and reduces the energy required for vacancy formation, which increases both the density and clustering of vacancies within the material [44-46]. These vacancies can coalesce to form microvoids that link and grow into larger voids, ultimately reducing resistance to crack propagation and contributing to premature failure of the material [45].

A schematic representation of this mechanism is shown in Figure 3.4. Experimental support for the HESIV mechanism has been obtained through thermal desorption spectrometry (TDS), which revealed elevated concentrations of strain-induced vacancies in iron and low-alloy ferritic steels [45;46]. Additional confirmation comes from positron lifetime measurements, which indicated an increase in the mean positron lifetime in iron under tensile straining conditions-a behavior that becomes even more pronounced when hydrogen pre-charging is applied [47].

3.5.5 Interactions Between Mechanisms

Although individual mechanisms such as Hydrogen-Enhanced Decohesion (HEDE), Hydrogen-Enhanced Localized Plasticity (HELP), Adsorption-Induced Dislocation Emission (AIDE), and Hydrogen-Enhanced Strain-Induced Vacancy formation (HESIV) have demonstrated relevance under specific conditions, there is growing consensus that multiple hydrogen embrittlement (HE) mechanisms may act simultaneously to explain the complex nature of hydrogen-assisted damage . For instance, HELP is typically dominant when fracture initiates at slip band intersections, whereas HEDE is more closely associated with decohesion at microstructural interfaces.

A combined interpretation of HE phenomena has been proposed through models such as the HEDE + HELP framework, which considers both intergranular fracture and microstructural evolution as evidence of the co-existence of mechanisms [48;49]. Brittle fracture surfaces exhibiting intergranular features alongside microstructure-sensitive decohesion have often been attributed to this dual-mechanism interaction.

Djukic et al. [49] reviewed the synergistic roles of these mechanisms, emphasizing that the interplay between HELP and HEDE may better explain hydrogen embrittlement under various microstructural and environmental conditions. Additionally, mechanisms such as HESIV may become significant depending on factors like material class, heat treatment, and stress state [51].

More recently, Neeraj et al. [52] introduced the nanovoid coalescence (NVC) mechanism to address hydrogen embrittlement in ferritic steels while accounting for the role of microstructure. The NVC model integrates the effects of HELP, HEDE, and HESIV into a sequential framework for hydrogen-induced fracture. As shown in figure 3.4, plastic deformation initiates in regions with high hydrogen concentration, where HELP facilitates dislocation motion. This is followed by the accumulation of vacancies, stabilized by hydrogen, which promotes the nucleation and coalescence of nanovoids, ultimately leading to crack propagation and failure.

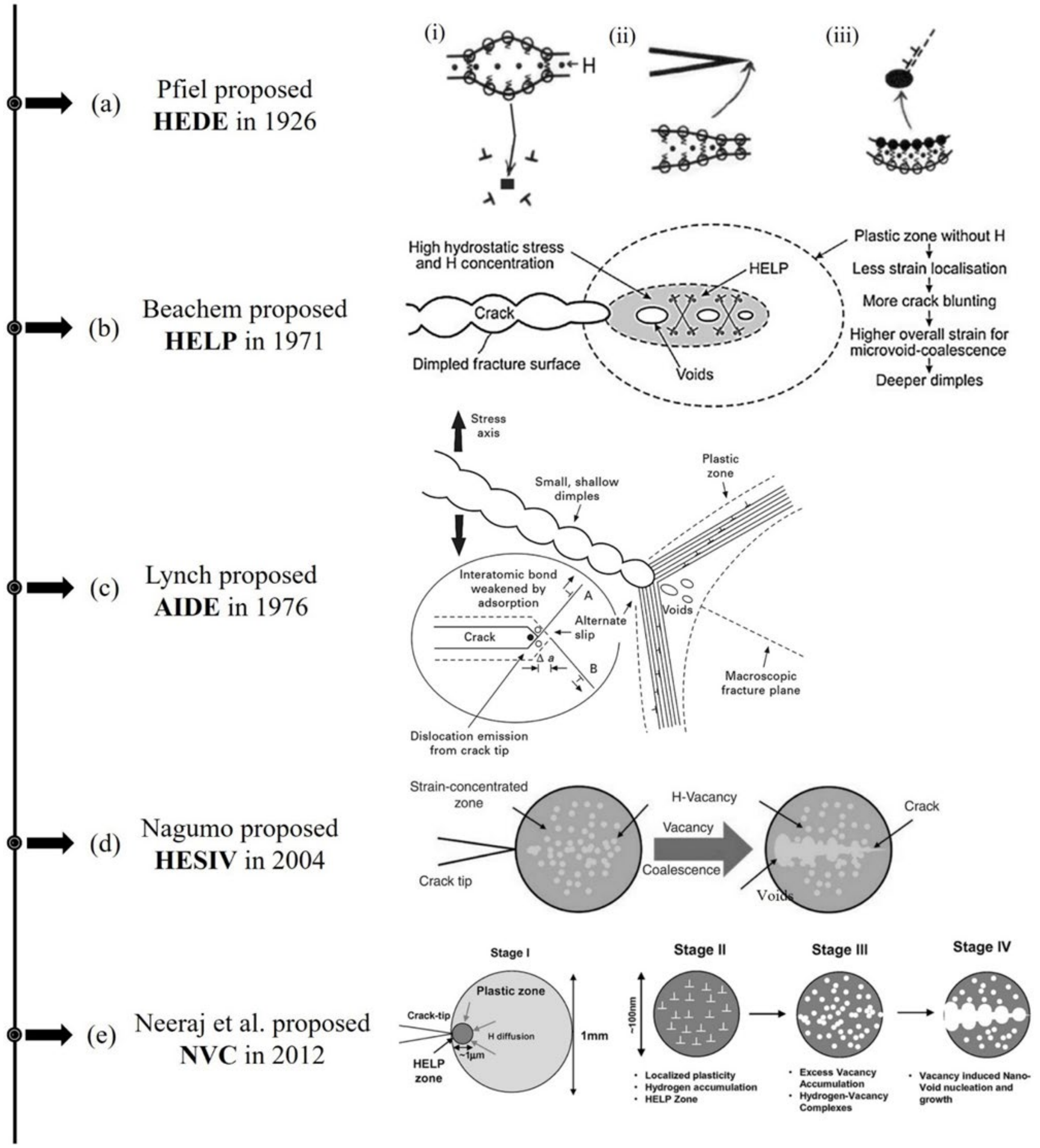

Figure 3.11 - HE mechanisms [53].

3.6 Hydrogen Diffusion

The equilibrium concentration of hydrogen in solid solution in α-iron at room temperature is extremely low-approximately one part per 10^8 by weight [54]. However, steel can retain significantly higher hydrogen concentrations due to the presence of microstructural traps. These traps, which act as preferential sites for hydrogen retention, include dislocations, grain boundaries, and interfaces between inclusions and second-phase particles [55].

When hydrogen is dissolved in a body-centered cubic (BCC) matrix, it preferentially occupies octahedral interstitial sites [56]. The asymmetry of these sites induces local elastic distortions, promoting interactions with various types of dislocations, including edge, screw, and mixed configurations [57]. Hydrogen trapping at these defects lowers the system's overall energy, thereby facilitating continued hydrogen ingress into the material.

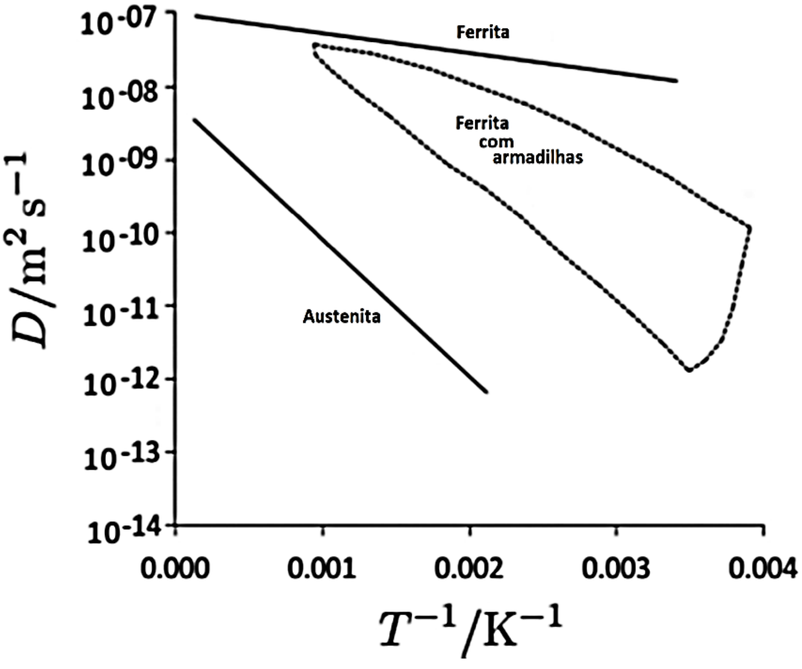

Figure 3.12 – H diffusion coefficient values in Fe [34].

Although the presence of traps in the metal increases hydrogen solubility in the solid state, it reduces hydrogen diffusivity. This effect is shown in Figure 3.4, which demonstrates a wide range of diffusion coefficients for hydrogen in ferrite across different samples. The activation energy for hydrogen diffusion in ferrite ranges from 6.9 kJ·mol^{-1} [56] to 8.0 kJ·mol^{-1} [54]. In the presence of traps, hydrogen diffusion in ferrite requires overcoming the binding energy between solute and trap, leading to different diffusion coefficients depending on the type of trap.

The earliest model of hydrogen diffusion in metals assumes that hydrogen at lattice sites and at microstructural traps remains in local thermodynamic equilibrium. This equilibrium, first quantified by Oriani (Eq. 3.7), expresses the partitioning of hydrogen solely in terms of the trap-binding (activation) energy and the fractional occupancies of lattice and trapping sites. Oriani's relation underpins the governing diffusion expression presented in Eq. 3.6 [3].

$$\frac{\partial c}{\partial_t} = \frac{\partial c_L}{\partial t} + \frac{\partial c_t}{\partial t} = D_L \nabla^2 c_L \qquad [3.6]$$

$$\frac{\theta_T}{1 - \theta_T} = \theta_L \, exp\left(-\frac{E_b}{RT}\right) \qquad [3.7]$$

Incorporating hydrogen flux caused by chemical potential and mass balance results on the modified form of the second Fick's law, [3.8]. Further work from Sofronis and McMeeking on finite element simulation, resulted on the transport equation [3.9] and the transport equation 3.10 [4].

$$\frac{\partial c_T}{\partial_t} + \frac{\partial C_L}{\partial_t} - \nabla \cdot (D_L \nabla D_T) + \nabla \cdot \left(\frac{D_L C_L \nabla_H}{RT} \sigma_h\right) = 0 \qquad [3.8]$$

$$D_{eff} = \frac{D_L}{\left(1 + \frac{\partial C_T}{\partial C_L}\right)} \qquad [3.9]$$

$$\frac{\partial C_L}{\partial t} - \nabla \cdot \left(D_{eff} \nabla C_L\right) + \nabla \cdot \left(\frac{D_{eff} C_L V_H}{R\,T} \nabla \sigma_h\right) = 0 \qquad [3.10]$$

From the previous model, Krom and Bakker included the plastic strain rate, resulting in the general form 3.11 and the flux equation 3.12, obeying Oriani's equilibrium. For diffusion dependent scenarios, such as SSRT and HIC, the plastic strain rate is too little, so the model from Sofronis and McMeeking is used on the modelling [3]. The model from Oriani is useful on the simulation of steady state scenarios, in which chemical potential gradients and mass balance can be ignored [2].

$$\frac{\partial C_T}{\partial t} = \frac{\partial C_T}{\partial C_L} \frac{\partial C_L}{\partial t} + \frac{\partial C_T}{\partial N_T} \frac{d\,N_T}{d\,\varepsilon_p} \frac{\partial \varepsilon_p}{\partial t} \qquad [3.11]$$

$$\frac{\partial C_T}{\partial t} = \frac{C_T(1-\theta_T)}{C_L} \frac{\partial C_L}{\partial t} + \theta_T \, \frac{dN_T}{d\varepsilon_p} \, \frac{\partial \varepsilon_p}{\partial t} \qquad [3.12]$$

3.7 Hydrogen Trapping sites

The strength of hydrogen trapping is commonly described in terms of the binding energy (E_b) or the activation energy required for de-trapping (E_a). Additionally, the occupation of trapping sites may be influenced by the energy barrier for hydrogen to enter the particle (E_t) [55]. In the lattice, the intrinsic diffusion energy of hydrogen is denoted as E_D, which is slightly altered in the vicinity of traps, becoming E_s. The de-trapping activation energy (E_a) corresponds to the sum of the binding energy (E_b) and the energy needed for hydrogen to diffuse in the region near the trap, as shown on figure 3.9 [59].

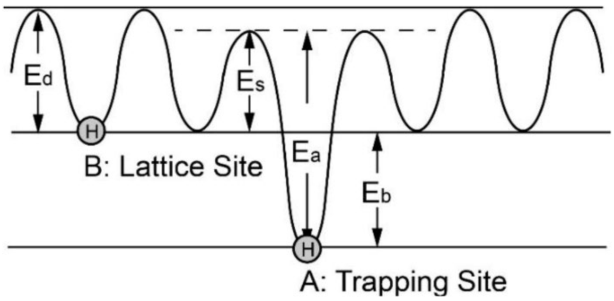

Figure 3.9 - Classical lattice diffusion of hydrogen [59].

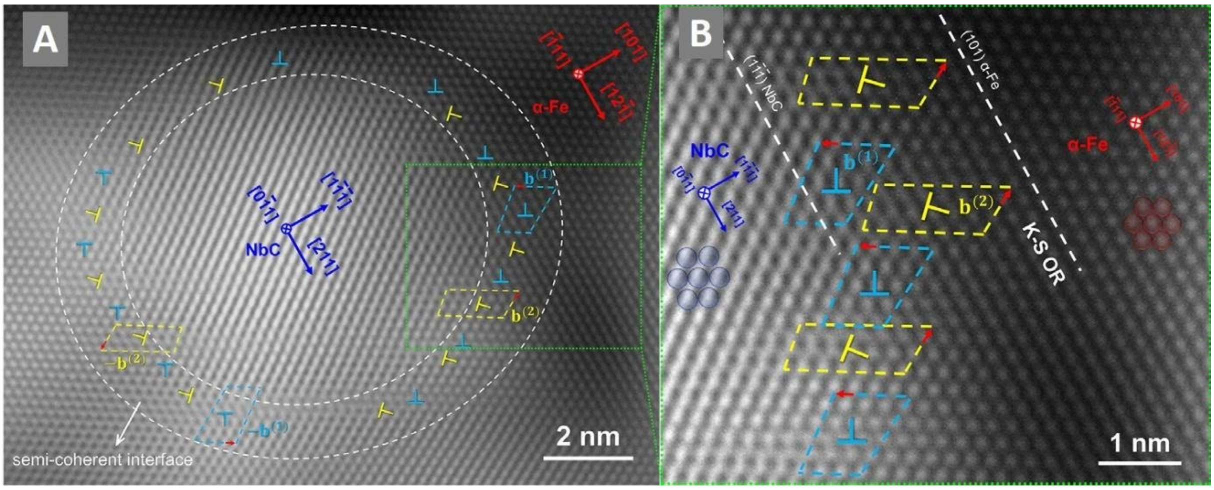

Figure 3.10— NbC particle observed with TEM. B) Close up on the particle-matrix interface [60].

The binding energy between atomic hydrogen and microstructural features varies significantly depending on the nature of the particle–matrix interface. Hydrogen traps can generally be classified as coherent, semi-coherent, or incoherent, based on the degree of crystallographic alignment with the surrounding matrix.

Coherent precipitates possess a crystallographically aligned interface with the matrix, resulting in minimal lattice strain. These interfaces serve as weak hydrogen traps, with binding energies typically ranging from 1.7 to 4.0 kJ·mol^{-1} [58]. Hydrogen in these sites remains highly mobile and is readily released under moderate thermal or mechanical loading.

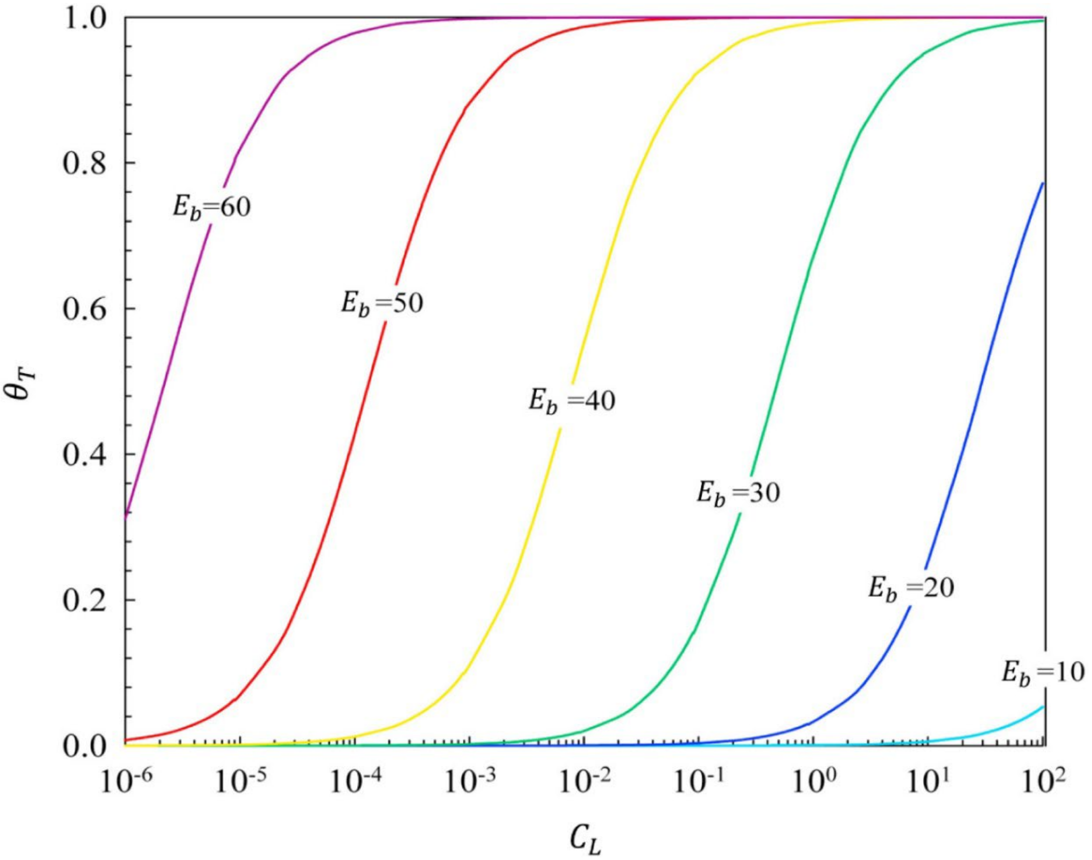

Figure 3.11 - Plotted equation 3.7 for different values of trap binding energy, showing the relation between the trapped H occupancy θ_T and lattice H concentration C_L, [55].

Semi-coherent precipitates exhibit partial crystallographic coherence, with misfit strain accommodated by dislocations at the interface as shown on figure 3.10[60]. These dislocations act as moderate-strength hydrogen traps, characterized by binding energies in the range of 30 to 70 kJ·mol^{-1} [57]. Trapping at these interfaces is reversible, which may contribute positively to hydrogen embrittlement resistance by temporarily immobilizing hydrogen and delaying its transport. Misfit dislocations are considered the dominant trapping features in these systems.

Incoherent precipitates, by contrast, lack a crystallographic relationship with the matrix, resulting in highly strained interfaces containing a high density of defects and voids. These features serve as strong, often irreversible hydrogen traps, with binding energies exceeding 90 $kJ \cdot mol^{-1}$ [57]. Although hydrogen in these sites is effectively immobilized and less likely to participate in embrittlement, under extreme service conditions these regions may act as preferential sites for crack nucleation due to localized stress concentrations.

The role of precipitates in mitigating hydrogen embrittlement depends on their capacity to trap hydrogen effectively without significantly compromising the material's ductility. Incoherent precipitates, while capable of strongly retaining hydrogen, may induce stress concentration at their highly strained interfaces, potentially promoting localized failure [55][57][65]. In contrast, semi-coherent precipitates - such as NbC, TiC and VC - provide a more favorable balance. These particles exhibit moderate hydrogen trapping capability while maintaining acceptable mechanical performance [57]. Acting as reversible hydrogen traps, they temporarily immobilize hydrogen, thereby delaying or suppressing the onset of embrittlement, as shown on figure 3.11.

3.8 Hydrogen Embrittlement in Large-Diameter Pipes

Large-diameter pipes are susceptible to hydrogen embrittlement when transporting petroleum contaminated with a partial pressure of H_2S greater than 0.3 kPa and under acidic pH conditions, a situation known as sour service [62], represented in region 3 of Figure 3.12.

In sour service conditions, hydrogen sulfide reacts with the steel through complex corrosion reactions, releasing hydrogen that interacts with the inner surface of the pipes and diffuses into the matrix as atomic hydrogen. This diffusion leads to concentrations high enough to trigger the nucleation and growth of cracks, even under stresses below the tensile strength limit.

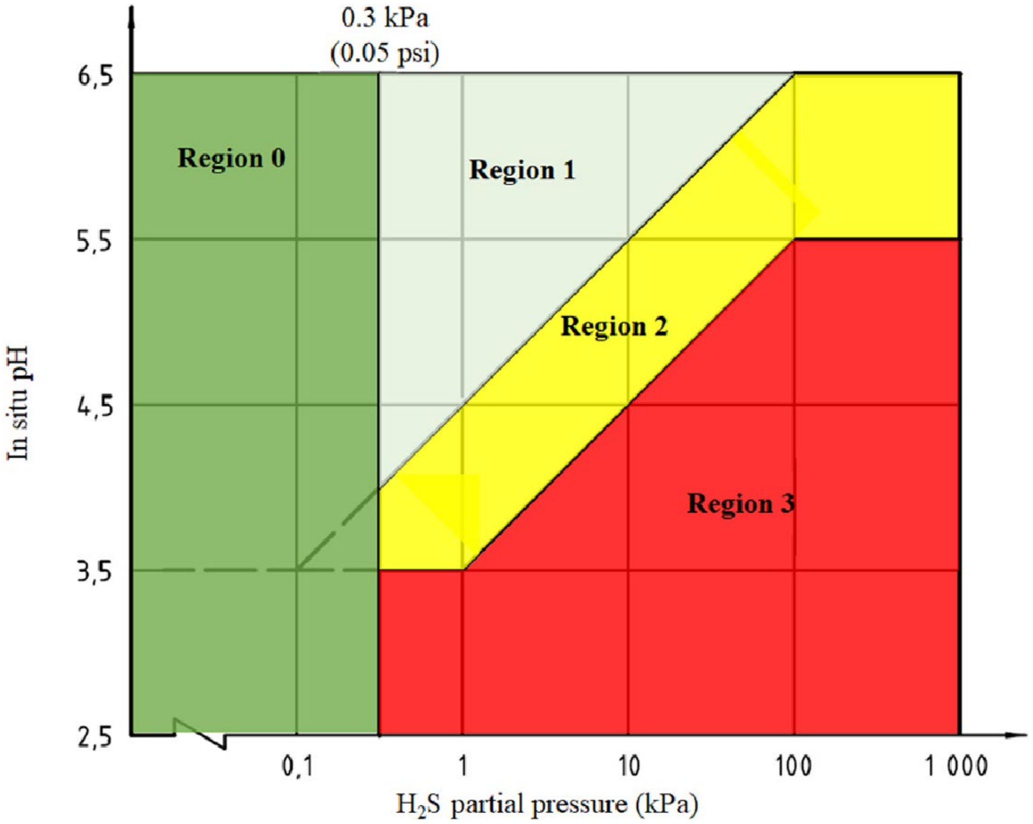

Figure 3.12 - Classification of service zones for low-carbon steels according to environmental severity, as established by the ISO 15156 standard [61].

3.9 Hydrogen-induced cracking

Hydrogen-induced cracking (HIC) is a form of hydrogen assisted damage that arises from the interaction between diffusible hydrogen in solid solution, non-metallic inclusions, and the metallic matrix. In this phenomenon, significant amounts of hydrogen accumulate at inclusions, where hydrogen gas bubbles nucleate and grow along with these inclusions and banded regions. This process ultimately leads to the formation of planar cracks parallel to the metal surface [62–73], as illustrated in Figures 3.13, 3.14, and 3.15. The three-dimensional morphology of hydrogen-induced cracks, recorded by Mostafijur Rahman et al. (Figure 3.15), clearly highlights their planar character.

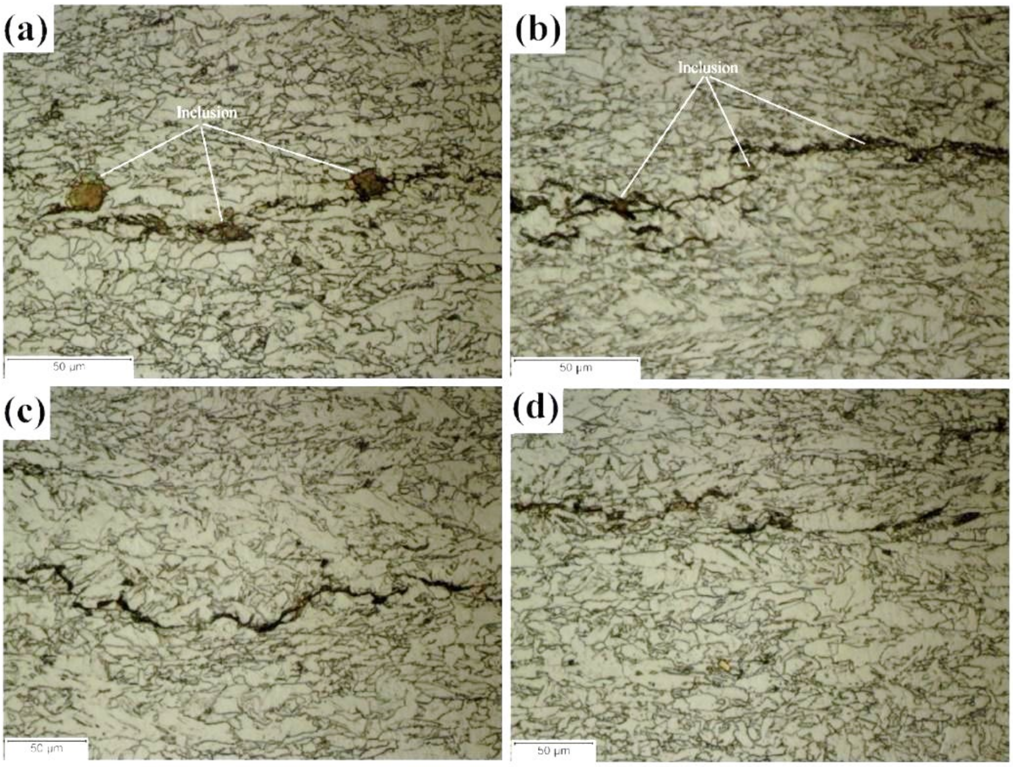

Figure 3.13 – Crack between cuboid inclusions [63].

Crack initiation in HIC is closely linked to the presence of non-metallic inclusions, particularly manganese sulfide , which act as preferential hydrogen trapping sites and serve as nuclei for crack formation. These inclusions exhibit weak interfacial bonding with the surrounding ferritic matrix, allowing atomic hydrogen, diffusing through the steel lattice, to accumulate and become irreversibly trapped at the inclusion–matrix interface. Under these conditions, hydrogen atoms recombine to form molecular hydrogen, generating localized internal pressure that leads to interfacial decohesion and crack initiation, process shown on Figure 3,14.

Once initiated, crack propagation is governed by the interplay between local microstructural features and hydrogen–material interactions. It typically manifests as either quasi-cleavage or intergranular fracture. Quasi-cleavage occurs when hydrogen lowers the cohesive strength along specific crystallographic planes, producing brittle fracture surfaces even in otherwise ductile materials. Intergranular fracture, in contrast, results from hydrogen-enhanced decohesion at grain boundaries, often intensified by the segregation of impurities.

Crack propagation in HIC frequently follows the rolling plane of the steel product. This preferred orientation is attributed to the alignment of microstructural bands, such as elongated MnS inclusions and segregation zones, which provide a mechanically favorable path for crack growth. The resulting anisotropy in crack behavior reflects the influence of thermomechanical processing and is further intensified by the uneven distribution of hydrogen traps along the rolling direction.

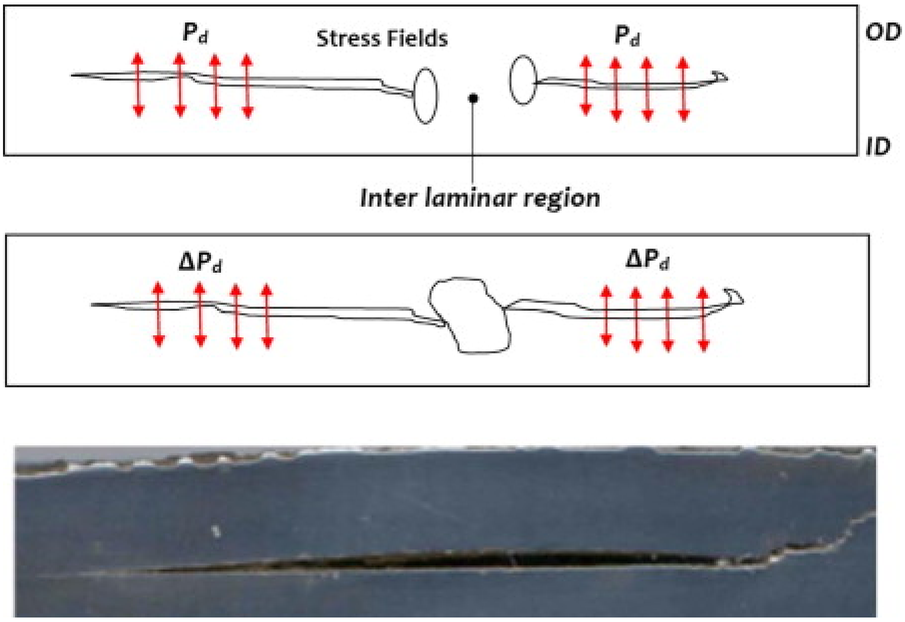

Figure 3.14 – Stepwise crack formation mechanism [64].

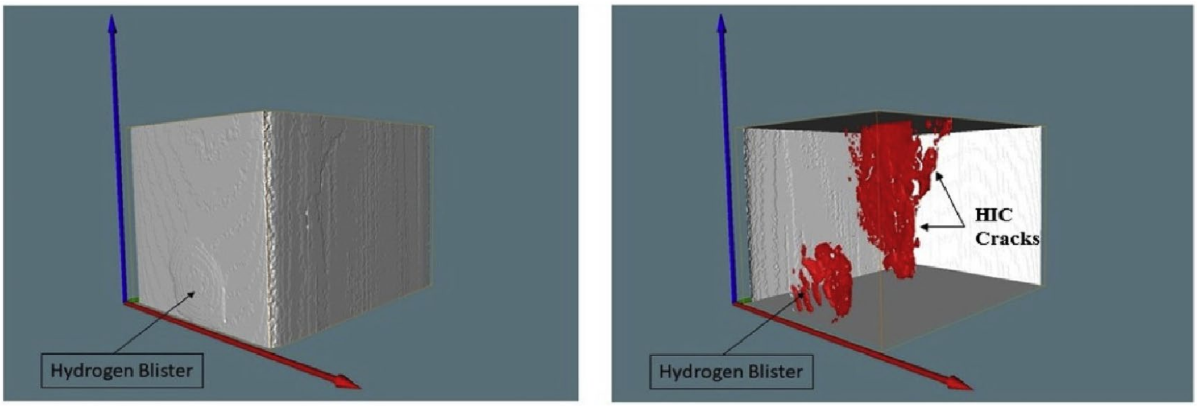

Figure 3.15 - (a) Tomography image showing surface deformation caused by a subsurface H_2 blister. (b) Tomography image showing a subsurface H_2 blister and an internal hydrogen-induced crack [66].

In X80 pipeline steel, the addition of copper improves resistance to hydrogen induced cracking (HIC) by shifting the microstructure from equiaxed to acicular ferrite and by dispersing fine particles rich in copper [67]. The presence of acicular ferrite is widely linked to superior performance. Conversely, Beidokhti [68] reported that higher fractions of bainite and martensite plus retained austenite (M/A) constituents reduce HIC resistance; when these constituents exceed roughly 30 %, susceptibility rises sharply. The authors proposed that softer phases can accommodate deformation caused by the internal pressure of incipient hydrogen bubbles, which helps to explain why initiation sites must be larger in ferritic matrices (≈ 150 µm) than in harder microstructures (≈ 20 µm).

Titanium also contributes to HIC mitigation because titanium based precipitates trap hydrogen. However, excessive titanium promotes the formation of bainite and M/A constituents in weld metal, which can outweigh the benefits provided by the precipitates[68]. Oversized titanium containing precipitates may even act as crack nucleation sites [69;70]. According to Beidokhti [69], titanium contents up to about 0.08 wt.% are beneficial, provided that the manganese content remains below 2 wt.%.

3.10 Slow Strain Rate Tensile Test

Slow-strain-rate tensile (SSRT) testing is a quasi-static tensile methodology in which specimens are elongated at very low, fixed strain rates, typically between 10^{-6} s^{-1} and 10^{-4} s^{-1} [73-74]. These rates are several orders of magnitude below those used in conventional tensile tests, so the material remains under load for a long time, giving diffusible hydrogen the opportunity to interact continuously with the evolving plastic zone. Hydrogen charging may be applied prior to the test via electrochemical treatment [72] via gaseous treatment [73]. The test yields a complete engineering stress-strain curve from which yield strength (YS), ultimate tensile strength (UTS), uniform elongation, total elongation and reduction of area (RA) can be extracted. Ductility metrics are usually quantified equation 3.13 and 3.14, where L_0 and A_0 are the initial gauge length and cross-section, and L and A_f are their post-fracture values. Because diffusible hydrogen and other species can redistribute during the slow loading, SSRT is widely adopted as a sensitive first-line method for ranking alloy susceptibility to hydrogen embrittlement and related time-dependent degradation processes.

$$\varepsilon_t = \frac{L - L_0}{L_0} \quad [3.13]$$

$$RA = \frac{(A_0 - A_f)}{A_0} \times 100\ \% \quad [3.14]$$

In practice, SSRT is carried out on a servo-hydraulic or electromechanical frame fitted with a high-resolution extensometer, and multiple repeats at an identical strain rate are recommended to achieve statistical confidence. Comparative assessment relies on ductility-loss indices, for example the ratio of charged to uncharged elongation or RA; a decrease in these indices indicates embrittlement, whereas shifts in YS or UTS can reveal hydrogen-induced hardening or softening. The monotonically increasing load allows the test to capture both initiation and growth of hydrogen-assisted cracks in a single experiment, something constant-load or high-rate methods often miss. However, the long test duration demands strict control of temperature, surface finish and environment to avoid artefacts such as corrosion products that may mask true hydrogen effects; polished specimens, inert grips and post-test fractography are therefore recommended in standard protocols. When these precautions are observed, SSRT provides a robust and broadly standardized framework for isolating the interplay among microstructure, hydrogen chemistry and mechanical integrity in high-strength steels and similar alloys.

Singh et al. [73] tested X65 samples. In their work, the samples were electrochemically charged with H at 20 mA/cm^2 for a period of 4 h in 1M H_2SO_4 with 1.4g/L Thiourea. SSRT was caried with a strain rate of 5x10-5s-1 in both charged and uncharged conditions. A decrease in elongation was noted, changing from 25% to 21%. The microstructure was composed of ferritic pearlite with the presence of MA constituent.

A study done by Rahman et al [66] on X70 pipeline steel electrochemically charged with H at 20 mA/cm^2 for periods of 1h, 8h and in 0.2M H_2SO_4 with 3g/L ammonium thiocyanate. SSRT were conducted in duplicate in an undisclosed strain rate with the results shown on figure 3.16, there was not a concensus on the reason of the ductility loss of the samples charged for 8h being larger compared with the samples charged for 8h and 15h. The microstructure contained globular, rectangular and spinoidal inclusions and grain size ranged from 0.2µm to 30µm.

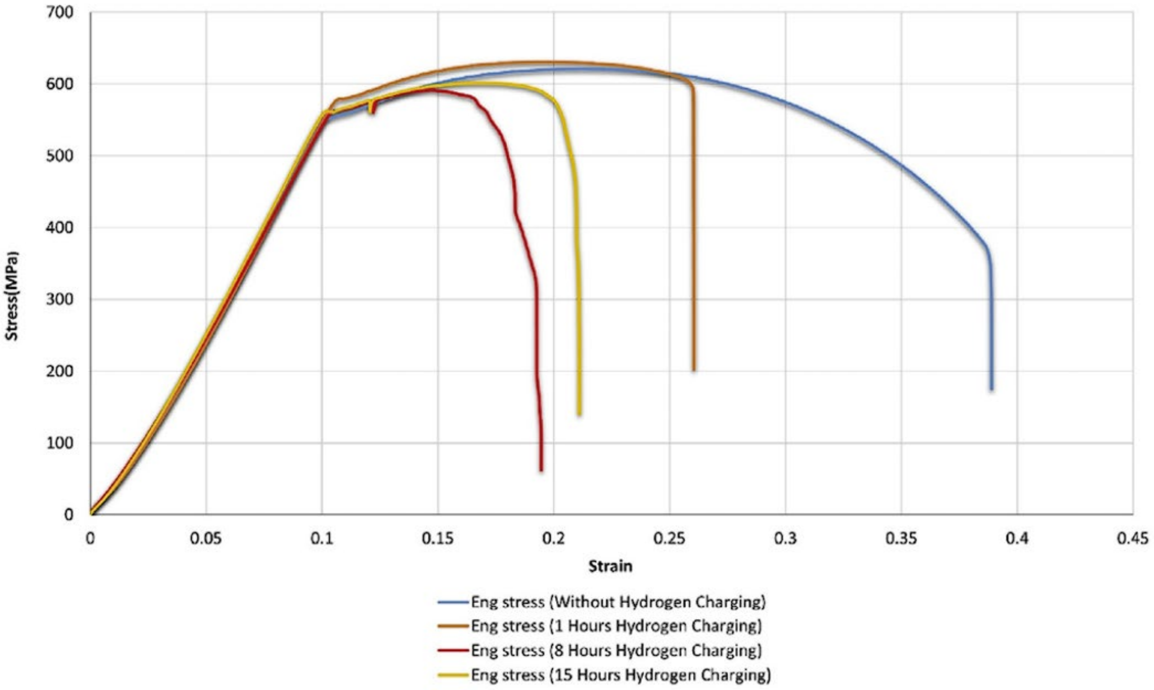

Figure 3.16 - Engineering Stress-Strain diagram of X70 Steel immediately after the hydrogen charging.[66]

Zhang et al.[72] conducted a series of experiments on X65 to investigate the effects of charging time, electrolyte, H recombination poison. For the electrolyte type investigation, solutions of 0.5 M H_2SO_4 + 5 g/L thiourea, 3.5 wt% NaCl + 5 g/L thiourea and 0.1 M NaOH + 5 g/L thiourea were prepared. SSRT was conducted with a strain rate of 8×10^{-5} s^{-1} and for each charging electrolyte, samples were charged for 0h, 0.5h, 2h, 8h and 24h. Results of the average the triplicate test are presented on figure 3.17.

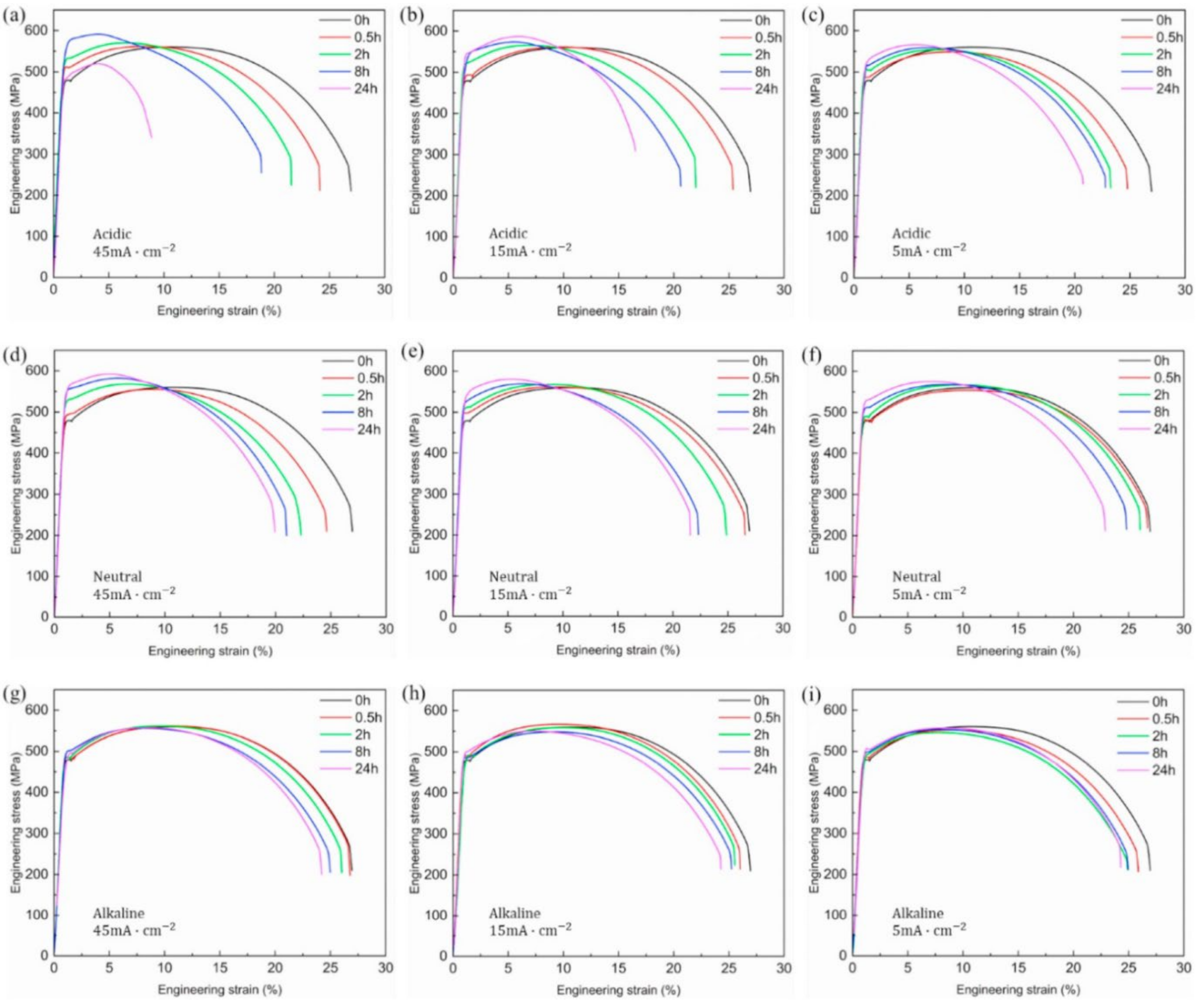

Figure 3.17 - Engineering stress-strain curves of X65 tensile specimens H-charged in different conditions: (a–c) acidic, (d–f) neutral, and (g–i) alkaline electrolytes with different current densities of (a,d,g) 5, (b,e,h) 15, and (c,f,i) 45 mA·cm^{-2} for different time periods [72].

Figure 3.17 shows that the greatest loss in ductility occurs in specimens that were charged with hydrogen in the acidic electrolyte at the highest current density (45 mA cm^{-2}) for the longest duration (24 h). This result contradicts the findings of Rahman et al. [66]. Only the specimens that experienced this pronounced ductility reduction also displayed a drop in ultimate tensile strength. Scanning electron microscopy fractography confirmed that the observed strength loss was associated with internal hydrogen blistering.

Zhang et al. [72] investigated the influence of recombination poison on the susceptibility to HE. Samples were charged in acidic conditions with a current density of 45 mA cm^{-2} for 24h with and without the addition of 5g/l thiourea. Results were compared to uncharged samples and are shown on figure 3.18. The effect of thiourea as is clear, as the samples H charged with poison had a more significant loss of ductility compared with the samples H charged without it.

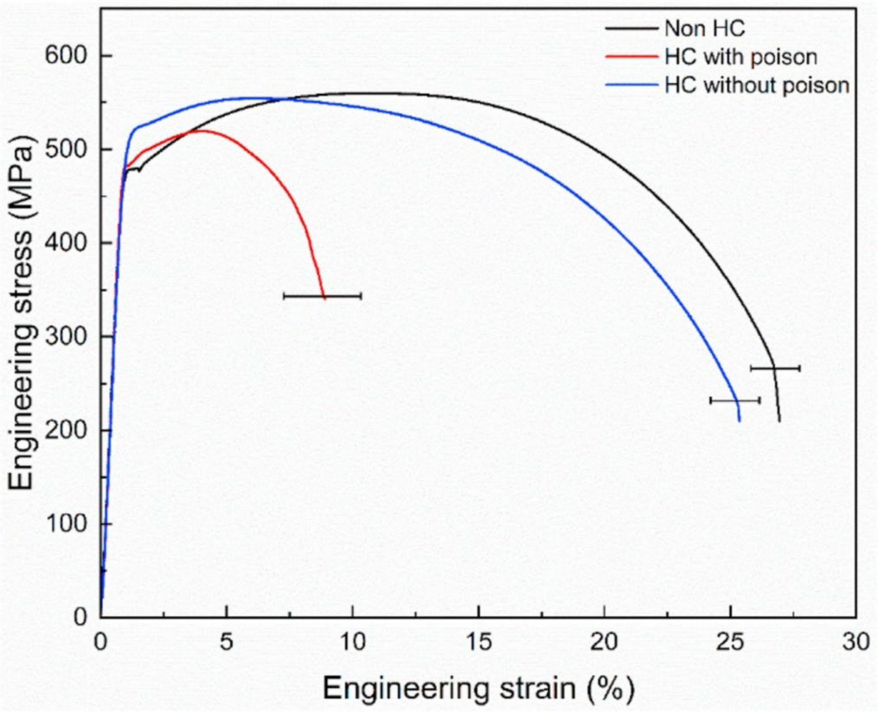

Figure 3.18 - Stress-strain curves of X65 tensile specimens hydrogen-charged for 24 h in an acidic electrolyte with a current density of 45 mA/cm2, both with and without addition of thiourea to the charging electrolyte[72].

Depover et al. [75] investigated the interaction between microstructure and hydrogen by examining a wide range of ferrous materials. The study included commercial transformation induced plasticity steels, dual phase steels, high strength low alloy steels and Armco grade steel, together with commercially pure iron.

To assess the level of hydrogen induced mechanical degradation, SSRT tests were conducted. Tensile samples were H charged with 1 g/L thiourea 0.5 M H_2SO_4 solution at a current density of 0.8 mA/cm2 for 1 or 2 h, and the tensile test were carried with a strain rate of $1.11x10^{-3}s^{-1}$ or $0.0111x10^{-3}s^{-1}$. The TRIP steel had a 60% loss on ductility, while the HSLA steel only had 8%.

The commercial steels were analyzed by TDS and hot extraction to further evaluate the interaction between H and microstructural constituents. TDS spectra is presented on figure 3.19. HSLA had the highest TDS peak, while it had the least amount of diffusible H, which is due to the presence of Ti and Nb nanoprecipitates that lower H diffusivity and increase HE resistance.

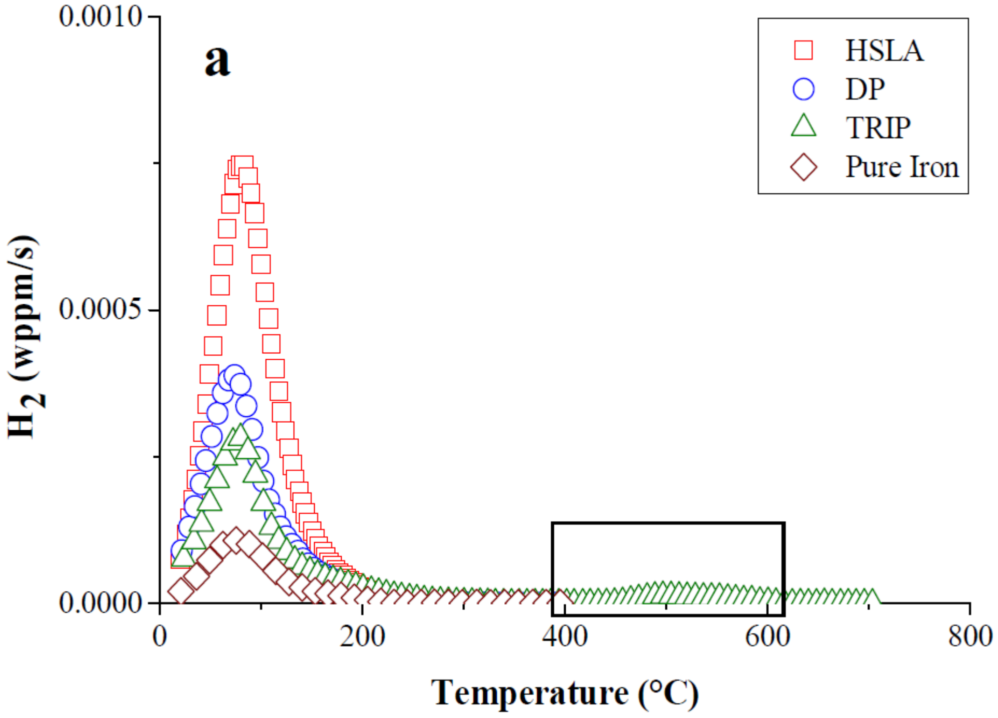

Figure 3.19 – TDS spectra of HSLA, DP, TRIP and pure iron[75].

3.11 Hydrogen Permeation Test

Hydrogen permeation test are performed in accordance with ISO 17081 [6] and ASTM G148 [7] standards, employing the electrochemical technique developed by Devanathan and Stachurski [76]. This method allows for the evaluation of hydrogen absorption, transport, and permeation in metallic materials and is applicable to a wide range of alloys. The test setup involves placing a metallic membrane between two electrochemical cells: the charging cell and the oxidation (or detection) cell, illustrated on figure 3.20. In the charging cell, atomic hydrogen is generated and adsorbed onto one surface of the metal. The hydrogen atoms then diffuse through the membrane and reach the opposite side, where they are oxidized in the detection cell. The oxidation of hydrogen at the exit surface produces an electric current proportional to the hydrogen flux through the material. By measuring this current, it is possible to determine the permeation flux and calculate the effective diffusivity of hydrogen in the metal.

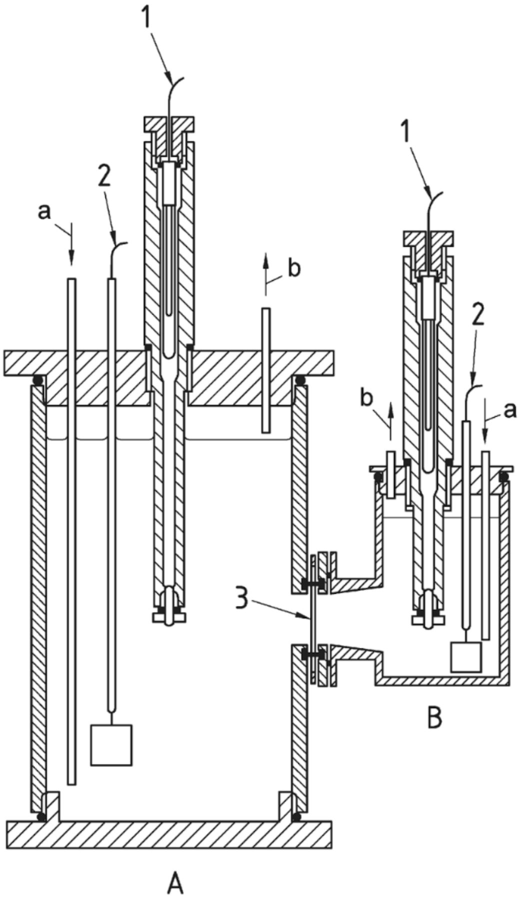

Figure 3.20 – Hydrogen permeation cell with double junction electrodes [6].

Zheng et al.[77] compared a finite element model with permeation experiments of a X80 steel. This study investigated the influence of the steel membrane thickness on the D_{eff}, the binding energy of the trapping sites, using TDS, and the hydrogen distribution on the membrane during the permeation test, using finite element models.

The apparent diffusion coefficient values were measured and are presented on figure 3.21. TDS curves were made with heating rates of 100°C/h, 150°C/h, 200°C/h, and 250°C/h, and the trap binding energies were 47.1 kJ/mol and 13.5 kJ/mol.

Trap occupancy across the permeation membrane, after the steady state current was reached, was simulated for different binding energies, results presented on figure 3.22 show that the traps with higher binding energies stay saturated, while those with lower binding energies release the bound H.

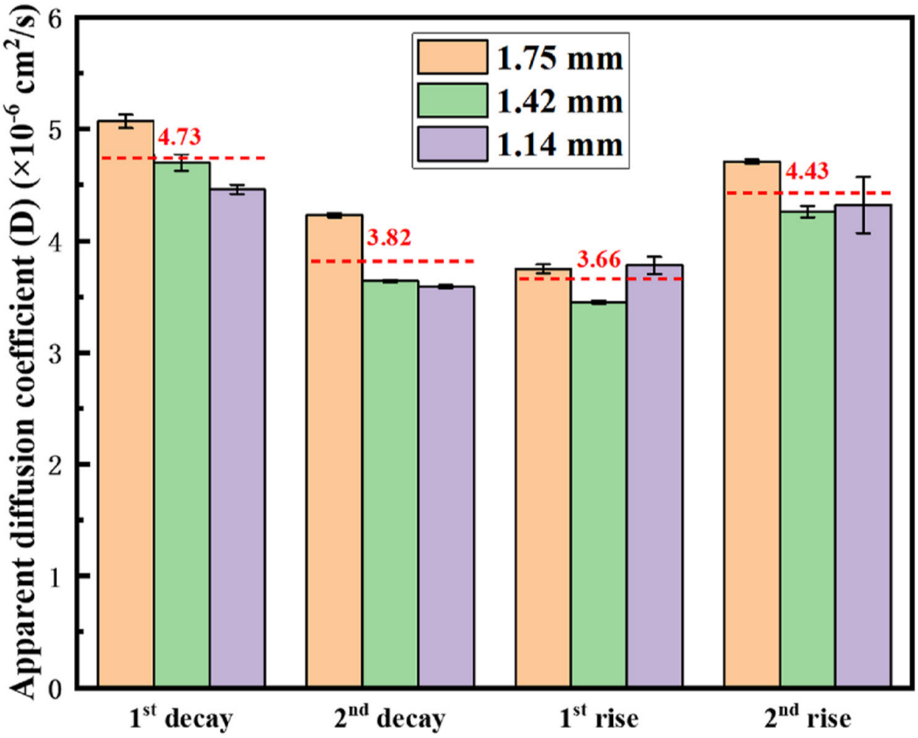

Figure 3.21 - Apparent diffusion coefficients in specimens of different thicknesses at different transients of the stepwise hydrogen charging process. The D_{app} values obtained in the three thicknesses were averaged to 4.73 × 10^{-6} cm^2 s^{-1}, 3.82 × 10^{-6} cm^2 [77]

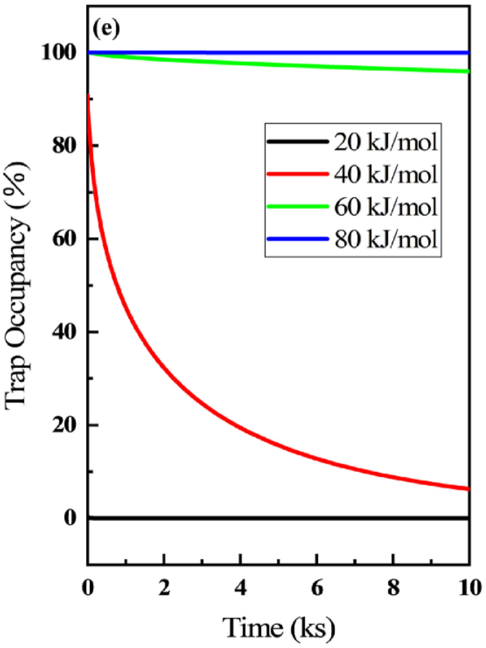

Figure 3.22 - Occupancy rate of trapping sites with different binding energies traps after reaching a steady state under the same conditions. [77]

4. METHODOLOGY

This study examined the hydrogen embrittlement (HE) resistance of two grades of API pipeline steels: X65 and X70. All steels were processed via Thermomechanical Controlled Processing (TMCP). For the X65 grade, three different processing conditions were evaluated. One of the alloys, designated X65-1, contained a lower manganese content and a higher niobium content than conventional microalloyed steels typically used in similar applications. As a result, it was processed under High Temperature Processing (HTP) conditions. The other two alloys, X65-2 and X65-3, exhibited typical chemical compositions for this grade but were manufactured in different steel plants.

The overall experimental workflow adopted in this study is illustrated in Figure 4.1. Initially, Hydrogen-Induced Cracking (HIC) tests were conducted in accordance with the NACE TM0284 standard. Subsequently, the microstructures across the plate thickness were examined using Optical Microscopy (OM) and Scanning Electron Microscopy (SEM), particularly at three specific locations: 2 mm below the surface (top), at one-fourth of the thickness (¼-T), and at mid-thickness (½-T). Hydrogen permeation tests were also performed at the same positions to assess the apparent diffusion coefficient (D_{eff}) and subsurface hydrogen concentration (C_0) through the thickness. Finally, Slow Strain Rate Tensile (SSRT) tests were carried out on hydrogen-charged and uncharged specimens extracted exclusively from the ¼-T region. The fracture surfaces of these samples were subsequently analyzed via fractography.

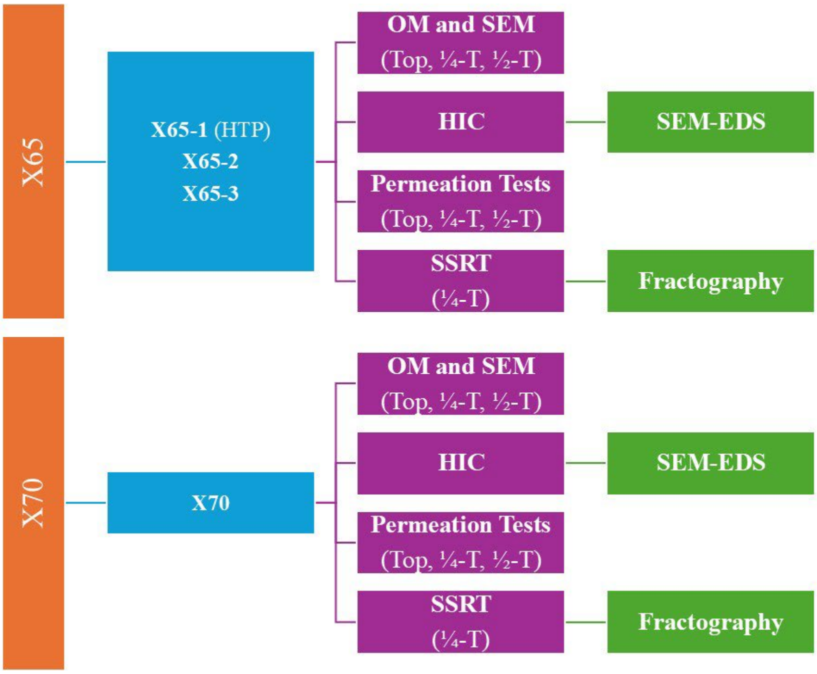

Figure 4.1 – Experimental workflow for assessing hydrogen embrittlement in API 5L X65 and X70.

4.1. Materials

One pipeline steel of grade API 5L X70 and three steels of grade API 5L X65 were thoroughly investigated. Table 4.1 presents the alloy designations along with their respective chemical compositions. All materials were processed using Thermomechanical Controlled Processing (TMCP). The initial slabs had a thickness of approximately 250 mm and were reheated to about 1240 °C for the X65-1 steel, and to approximately 1080 °C for the X65-2, X65-3, and X70 steels. Following reheating, controlled rolling was performed to reduce the thickness to 32 mm, with a finishing temperature of 850 °C. Subsequently, accelerated cooling was applied at a rate of 20 °C/s to promote the formation of a microstructure containing ferrite and bainite.

The X65-1 steel was manufactured using the HTP method, which involves reducing the manganese (Mn) content while compensating the carbon equivalent (CE) through the addition of niobium (Nb) (Table 4.1). This compositional adjustment raises both the complete solubilization temperature of Nb in carbon and the non-recrystallization temperature, thereby requiring the roughing passes during thermomechanical controlled rolling to be conducted at higher temperatures. Further details of the plates processing have been omitted due to industrial confidentiality.

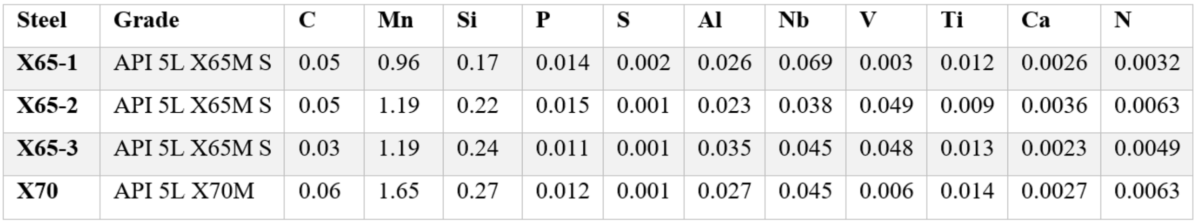

Steel	Grade	C	Mn	Si	P	S	Al	Nb	V	Ti	Ca	N
X65-1	API 5L X65M S	0.05	0.96	0.17	0.014	0.002	0.026	0.069	0.003	0.012	0.0026	0.0032
X65-2	API 5L X65M S	0.05	1.19	0.22	0.015	0.001	0.023	0.038	0.049	0.009	0.0036	0.0063
X65-3	API 5L X65M S	0.03	1.19	0.24	0.011	0.001	0.035	0.045	0.048	0.013	0.0023	0.0049
X70	API 5L X70M	0.06	1.65	0.27	0.012	0.001	0.027	0.045	0.006	0.014	0.0027	0.0063

Table 4.1 - Steel composition (wt.%).

4.2. Microstructural Characterization

Initially, the microstructures of the different steels and their through-thickness variations were characterized using optical microscopy and scanning electron microscopy. Sample preparation for metallographic analysis involved five sequential steps: extraction from the steel plate, grinding, polishing, and chemical etching. The selected thick plate specimens were embedded in acrylic resin with the cross-sectional face exposed for analysis. Grinding was carried out using a series of water-lubricated silicon carbide papers with progressively finer grit sizes (100, 240, 320, 400, 600, and 1000). Polishing was then performed using diamond suspensions with particle sizes of 9 µm, 3 µm, and 1 µm to achieve a mirror-like surface finish. Finally, the samples were etched with 5% Nital solution to reveal the microstructural features of the steels.

OM was employed to provide a general assessment of grain distribution and morphology. Images were captured at magnifications of 500× and 1000× at three distinct positions across the thickness of the samples: 2 mm from the surface (top), at one-quarter of the thickness, and at mid-thickness (center). The microstructures were further characterized by using a field-emission scanning electron microscope (FE-SEM, FEI Quanta 3D FEG) equipped with energy-dispersive X-ray spectroscopy (EDS) for elemental analysis at the Microscopy Center of UFMG, as well as a conventional scanning electron microscope (SEM, JEOL JSM-360LV) at the Department of Metallurgical and Materials Engineering at UFMG.

4.3. Hydrogen Permeation Test

For the tests, sections were extracted from the steel plates parallel to the normal direction (ND) at three distinct positions: approximately 2 mm below the surface, one-quarter thickness (¼-T), and mid-thickness (½-T). These sections were cut using wire electrical discharge machining (EDM), a method chosen to minimize thermal and mechanical damage to the material. Each section was then machined into rectangular membranes with approximate dimensions of 50 mm

× 20 mm × 2 mm. Two membranes were prepared from each selected position for each steel plate. To achieve the final target thickness and eliminate any surface damage introduced during machining, the membranes were mechanically ground on both sides using silicon carbide (SiC) abrasive paper up to 600 grit, reducing the thickness to approximately 1 mm.

The Devanathan–Stachurski hydrogen permeation setup consists of two electrochemical cells sharing the same sample as a working electrode. One cell generates hydrogen on one side of the membrane, while the other oxidizes the hydrogen that diffuses through it. The schematic design of the Devanathan–Stachurski cell is shown in the top image of Figure 4.2, and the actual experimental assembly is depicted in the bottom image of this figure.

The electrochemical cells were equipped with reference electrodes: silver/silver chloride (Ag/AgCl) for the charging (reduction) cell and mercury/mercury oxide (Hg/HgO) for the oxidation cell. Platinum-coated titanium auxiliary electrodes were employed and strategically positioned to minimize the potential drop across the system. A Luggin capillary was incorporated into the oxidation chamber to further reduce the potential gradient between the membrane surface and the reference electrode.

The charging compartment was filled with an aqueous solution of 0.1 M NaOH, appropriate for the electrochemical generation of atomic hydrogen on the entry surface of the membrane. On the opposite side, the oxidation chamber was filled with a standardized 0.1 M NaOH solution to enable the oxidation of hydrogen atoms that permeated through the membrane. To enhance hydrogen activity at the charging surface, 3 g/L of thiourea was added to the charging solution, acting as a hydrogen recombination poison.

Before the main experiment, the oxidation cell underwent a stabilization period, during which the background oxidation current was allowed to decrease below 1 μA. The system was operated using a BioLogic SP300 bipotentiostat, which controlled the applied potential and continuously monitored the oxidation current at the detection surface.

To improve oxidation efficiency during testing, the oxidation side of each membrane was electroplated with a thin layer of palladium, which serves to catalyze hydrogen oxidation and reduce the buildup of an oxide layer that typically forms and acts as a barrier. After palladium deposition, the samples were rinsed with distilled water and purified with ethanol.

During the test, hydrogen was generated cathodically on the charging side by applying a constant current of 5 mA using a bipotentiostat. Simultaneously, the oxidation side was anodically polarized at 300 mV versus the mercury/mercury oxide (Hg/HgO) using a bipotentiostat. Once the oxidation current reached a steady-state value (I_{ss}), the cathodic current was interrupted, marking the end of the buildup transient and the beginning of the transient decay. The atmosphere was purged with nitrogen gas and the solution level was maintained with a peristaltic pump.

The main parameters derived from the permeation curve were the time lag (t_L) and the steady-state oxidation current (I_{ss}). The time lag (t_L) corresponds to the time required for the permeation current to reach 63% of the steady-state value. The steady-state current (I_{ss}) represents the constant permeation current after the system reaches equilibrium.

From these parameters, the effective diffusivity (D_{eff}) and the apparent subsurface hydrogen concentration (C_0) were determined using the following equations:

$$D_{eff} = \frac{L^2}{6\,t_L} \qquad [4.1]$$

$$C_0 = \frac{I_{SS}.L}{F.A.D_{eff}} \qquad [4.2]$$

where L is the membrane thickness (cm), I_{ss} is the steady-state atomic hydrogen permeation current (µA), A is the exposed surface area in the oxidation cell (cm^2), F is Faraday's constant (9.6485×10^4 C/mol), and $t_L$is the time lag (s).

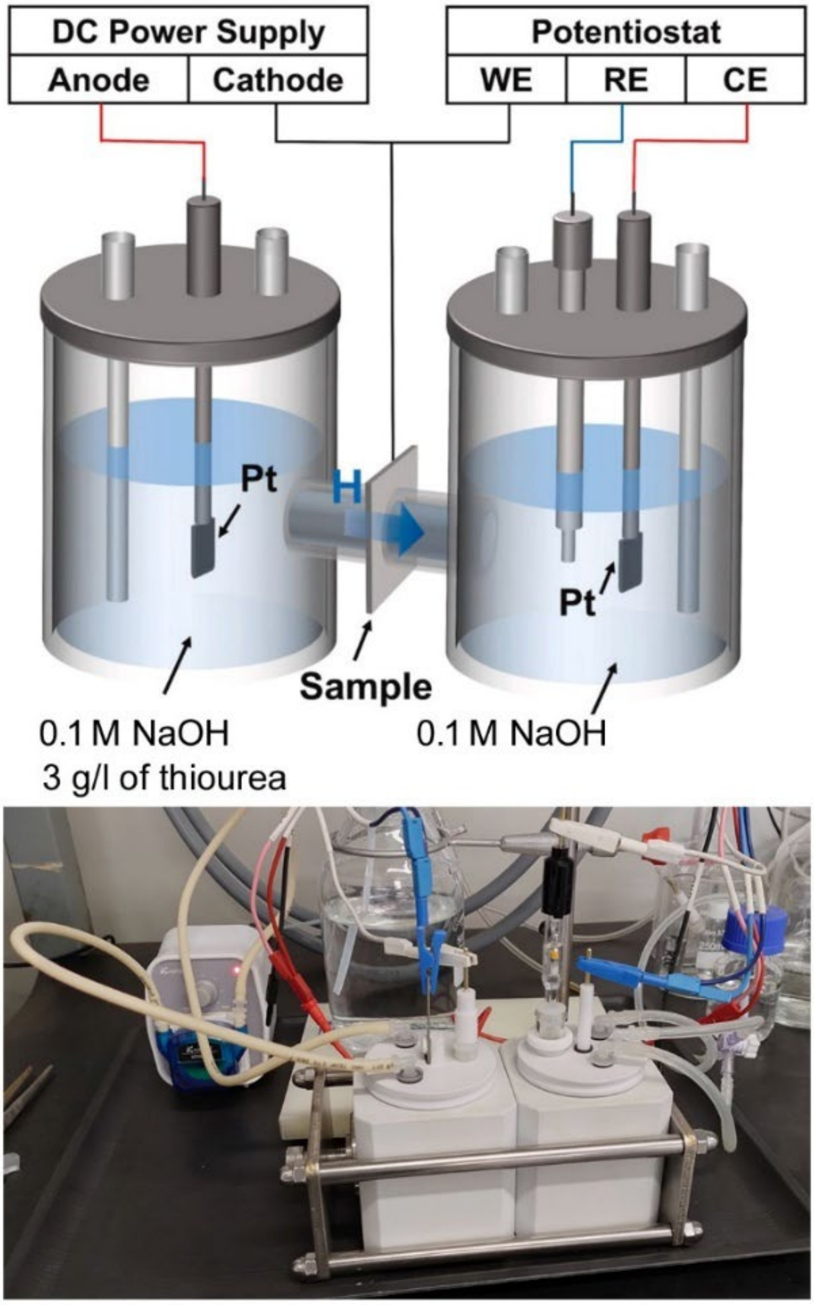

Figure 4.2 – Davanathan and Stachurski setup used for hydrogen permeation test.

4.4. Resistance to Hydrogen-Induced Cracking

Hydrogen-induced cracking (HIC) susceptibility was evaluated following NACE Standard TM0284–96 [10]. Standard HIC specimens (20 mm × 100 mm × plate thickness), with the length oriented along the rolling direction, were tested at 25 °C for 96 h. The tests were conducted at the Corrosion Laboratory of Vallourec, located in Belo Horizonte, Brazil.

The specimens were placed inside a hermetically sealed vessel equipped with gas inlet and outlet ports. The vessel was filled with a test solution (Solution A of the standard), composed of 0.5% acetic acid and 5% sodium chloride dissolved in distilled water, simulating seawater conditions. After sealing, the vessel was purged with nitrogen (N_2) to remove all air, followed by saturation with hydrogen sulfide (H_2S) at a flow rate of at least 100 mL/min for the entire duration of the test.

After testing, each specimen was sectioned into four segments of 25 mm length, and polished cross-sections were examined for the presence of cracks. It is important to note that the HIC test does not establish pass/fail criterion or replicate real service conditions; rather, it provides a comparative assessment of the cracking susceptibility among different steels.

4.5. Slow Strain Rate Tensile Testing

The effect of hydrogen charging on the mechanical properties of the materials was evaluated by slow strain rate tensile (SSRT) testing. Tests were performed at a nominal strain rate of approximately 10^{-4} s^{-1} on both hydrogen-charged specimens, prepared via electrochemical charging, and uncharged reference specimens. SSRT testing was initiated immediately after the completion of the hydrogen charging process to minimize hydrogen loss.

Tensile tests were conducted in accordance with ASTM A370-23 [8], using subsize specimens with dimensions specified by the standard. For these tests, the Instron model 5288 universal testing machine was employed. Each condition was tested in duplicate, using specimens extracted from three different through-thickness locations: near the top surface, at one-quarter thickness (¼-T), and at mid-thickness (½-T) of the steel plates. The three X65 steels evaluated (Steels 1, 2, and 3) are detailed in Table 4.1.

Hydrogen charging was carried out electrochemically by immersing the specimens in a solution containing 0.1 mol/L H_2SO_4 and 3 g/L thiourea. A cathodic current density of 10 mA/cm² was applied continuously for 17 hours to promote hydrogen absorption into the material [78]. The setup used for the electrochemical hydrogen charging of a subsize specimen, as employed in the SSRT experiments, is shown in Figure 4.3.

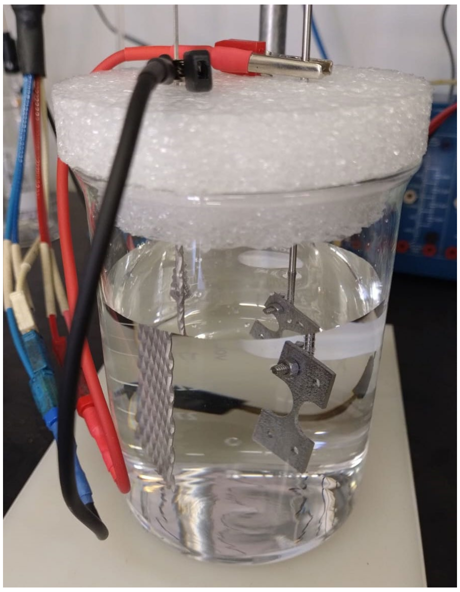

Figure 4.3 - Electrochemical hydrogen charging setup for a subsize specimen used in the SSRT experiments.

5. RESULTS AND DISCUSSION

5.1. Through-Thickness Assessment of the Microstructure in As-Received Steels

Based on the steel compositions presented in Table 4.1 and the TMCP pass schedule followed by accelerated cooling at a rate of 20 °C/s, the *expected microstructure* [13][78] for all steels was predominantly composed of acicular ferrite and bainite near the surface (referred to as the top region); a combination of equiaxed and acicular ferrite around one-quarter of the plate thickness; and a mixture of equiaxed ferrite and bainite at mid-thickness [13][22][82]. This analysis assumes the absence of segregation and the exclusion of particles originating from the steelmaking process. Anisotropy was also expected in all cases due to the elongation of austenite grains during the final rolling passes and the subsequent nucleation of ferrite along austenite grain boundaries.

To verify these expectations, initial microstructural characterization of the X65 and X70 steels was conducted using OM, complemented by scanning electron microscopy SEM in secondary electron mode. Figures 5.1 to 5.8 illustrate the microstructures for each steel variant: X65-1 (HTP), X65-2, X65-3, and X70. OM and SEM images were obtained at multiple magnifications and from three through-thickness locations - approximately 2 mm below the surface (top), at one-quarter thickness (1/4-T), and mid-thickness (1/2-T) - allowing both general and detailed visualization of the microstructural features.

The observed microstructures revealed a complex mixture of phases and constituents across all samples, which did not entirely align with the initial expectations. However, phase differentiation based solely on OM and SEM images proved to be challenging. In the absence of advanced techniques such as electron backscatter diffraction (EBSD) and transmission electron microscopy (TEM), the interpretation of the microstructures in this study relied on comparative analysis with existing literature on high-strength low-alloy (HSLA) steels. The microstructural features identified were therefore inferred through correlation with those previously described in similar systems.

In X65-1, the microstructure at the top surface predominantly consists of a quasi-polygonal ferrite (QPF) matrix (light regions in Figure 5.1), interspersed with small areas of other constituents (dark regions in Figure 5.1). At the one-quarter thickness and, more prominently, at the mid-thickness position, acicular ferrite (AF) is also observed alongside QPF and isolated bainitic areas (Figures 5.1 and 5.2). Among the three analyzed regions of the X65-1 plate, the finest grain size was measured at the one-quarter thickness position. Additionally, large and elongated inclusions are detected at mid-thickness (Figure 5.1-f). In OM and SEM images (Figures 5.1 and 5.2), AF appears as a complex, interwoven network of fine ferrite laths, often accompanied by fine precipitates aligned along the lath boundaries

In X65-2, the microstructure at the subsurface predominantly consists of polygonal ferrite (PF) and quasi-polygonal ferrite (QPF), as clearly shown in Figure 5.4. In this region, equiaxed or slightly elongated particles, measuring a few micrometers in size, are dispersed throughout the ferritic matrix, as indicated by the white arrow in Figure 5.4-b. These particles appear slightly raised and exhibit higher brightness in SEM images, which is attributed to their greater resistance to acid etching during metallographic preparation. At the one-quarter thickness position, some bright particles appear finer and are located along grain boundaries, with typical lengths of approximately 10 μm, as highlighted by white arrows in Figure 5.4-d. Based on their morphology, distribution, and etching response, these features are interpreted as carbides.

At the mid-thickness position, a small amount of upper bainite (UB) can be distinguished in the OM image (Figure 5.3-f) and in the SEM image (Figure 5.4-e and 5.4-f). Additionally, yellow, cuboid-shaped non-metallic particles are observed in this region in the optical microscopy image (Figure 5.3-f). Based on EDS measurements of similar particles identified in the same region of the X70 steel, these precipitates are presumed to be complex carbonitrides, such as (Ti,Nb)(C,N), as will be further discussed in the following sections. Unlike other regions of the plate, elongated second-phase particles are no longer observed at mid-thickness; instead, only very fine carbide precipitates are present.

The localized presence of UB at mid-thickness, although limited, together with the distribution of hard non-metallic inclusions, can have a significant impact on mechanical performance and susceptibility to hydrogen-induced cracking. Additionally, the presence of complex carbonitride precipitates may serve as potent initiation sites for HIC. Consequently, even a small fraction of UB, when combined with a higher density of inclusions at mid-thickness, can locally compromise the steel’s resistance to hydrogen-induced damage, despite the predominantly ferritic nature of the overall microstructure. The implications of this microstructural configuration are further examined in the following sections through HIC and hydrogen permeation testing.

In X65-3 (Figures 5.5 and 5.6), the microstructure is predominantly composed of polygonal ferrite and quasi-polygonal ferrite throughout the entire thickness. Unlike X65-2, even at mid-thickness, the microstructure remains a homogeneous mixture of PF and QPF, with no evidence of upper bainite formation. Moreover, no non-metallic inclusions or elongated carbides were detected in X65-3, indicating a cleaner and more uniform microstructure across the plate.

In the X70 steel, the microstructure observed approximately 2 mm below the surface and at the one-quarter thickness position is primarily composed of polygonal ferrite (PF), quasi-polygonal ferrite (QPF), and acicular ferrite (AF), as shown in Figure 5.8. At mid-thickness, a markedly pronounced centerline segregation is observed (Figure 5.7), where the microstructure is characterized by the presence of granular bainite (GB), also illustrated in Figure 5.8.

The influence of this microstructure is further supported by the microhardness analysis shown in Figure 5.9, which reveals a pronounced hardness gradient along a banded region at the center of the X70 steel. Vickers microhardness values within this region vary substantially, ranging from 288 to 164 HV, with a maximum difference of 96 HV. These variations reflect the heterogeneity of the microstructure and may be associated with local differences in phase composition and mechanical performance.

A comparative summary of the main microstructural features observed across the thickness of the studied steels is presented in Table 5.1. The table highlights the key differences in surface and mid-thickness microstructures among the X65-1, X65-2, X65-3, and X70 steels, providing a basis for correlating microstructural characteristics with HIC susceptibility.

Table 5.1 - Comparative Summary of Through-Thickness Microstructures in X65 and X70 Steels.

Steel	**Surface Microstructure**	**Mid-Thickness Microstructure**
X65-1	QPF matrix with small regions of other constituents	AF with QPF and isolated bainitic regions; large, elongated inclusions
X65-2	PF + QPF; fine carbides aligned along grain boundaries	Localized UB and non-metallic carbonitrides
X65-3	Homogeneous mixture of PF and QPF	Homogeneous mixture of PF and QPF
X70	PF + QPF + AF	Pronounced centerline segregation; GB matrix with dispersed M/A constituents

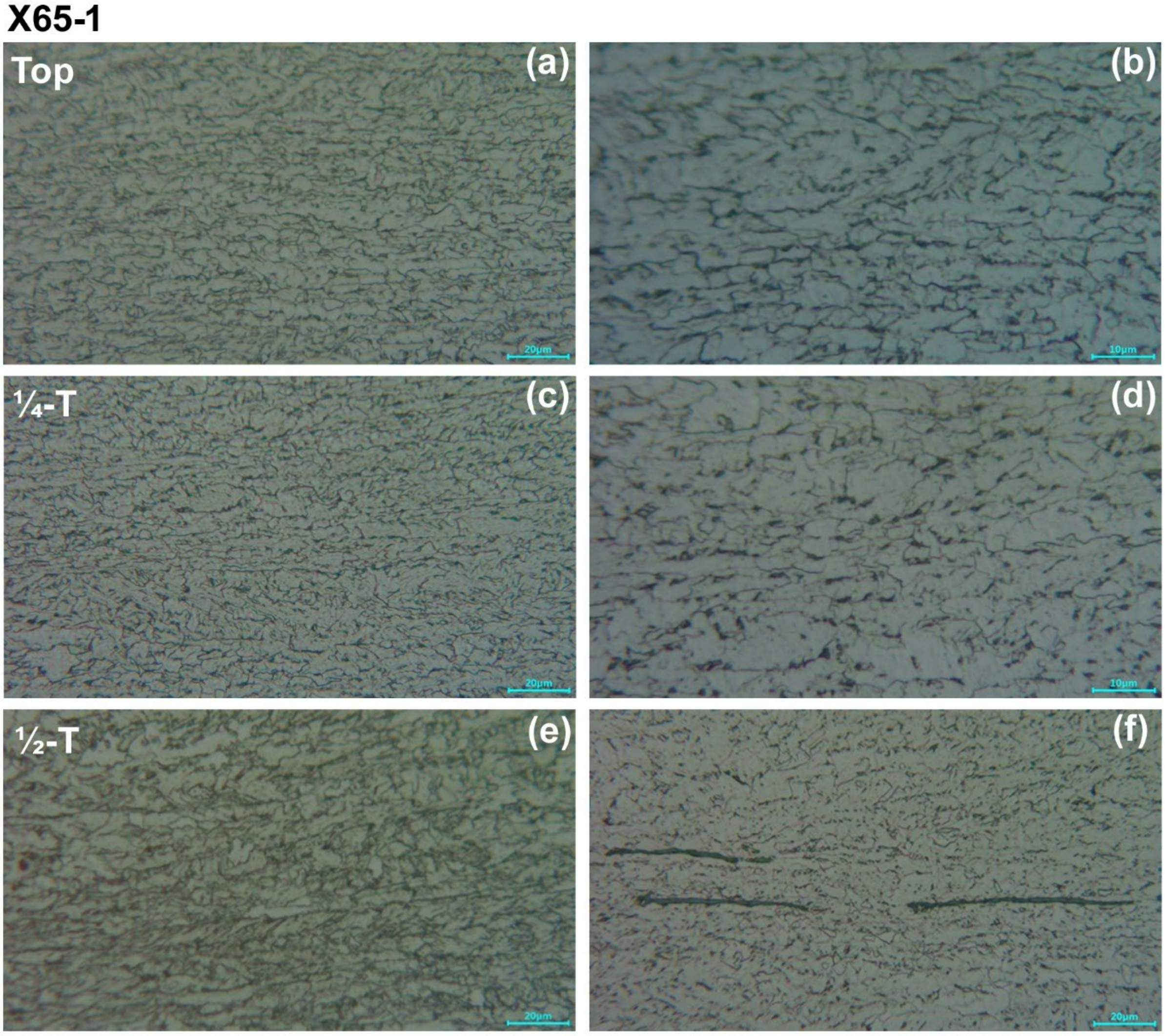

Figure 5.1 – OM images of the X65-1 steel obtained for the top, ¼ thickness, and ½ thickness at two different magnifications. In the images, the rolling direction of the steel plates is oriented horizontally.

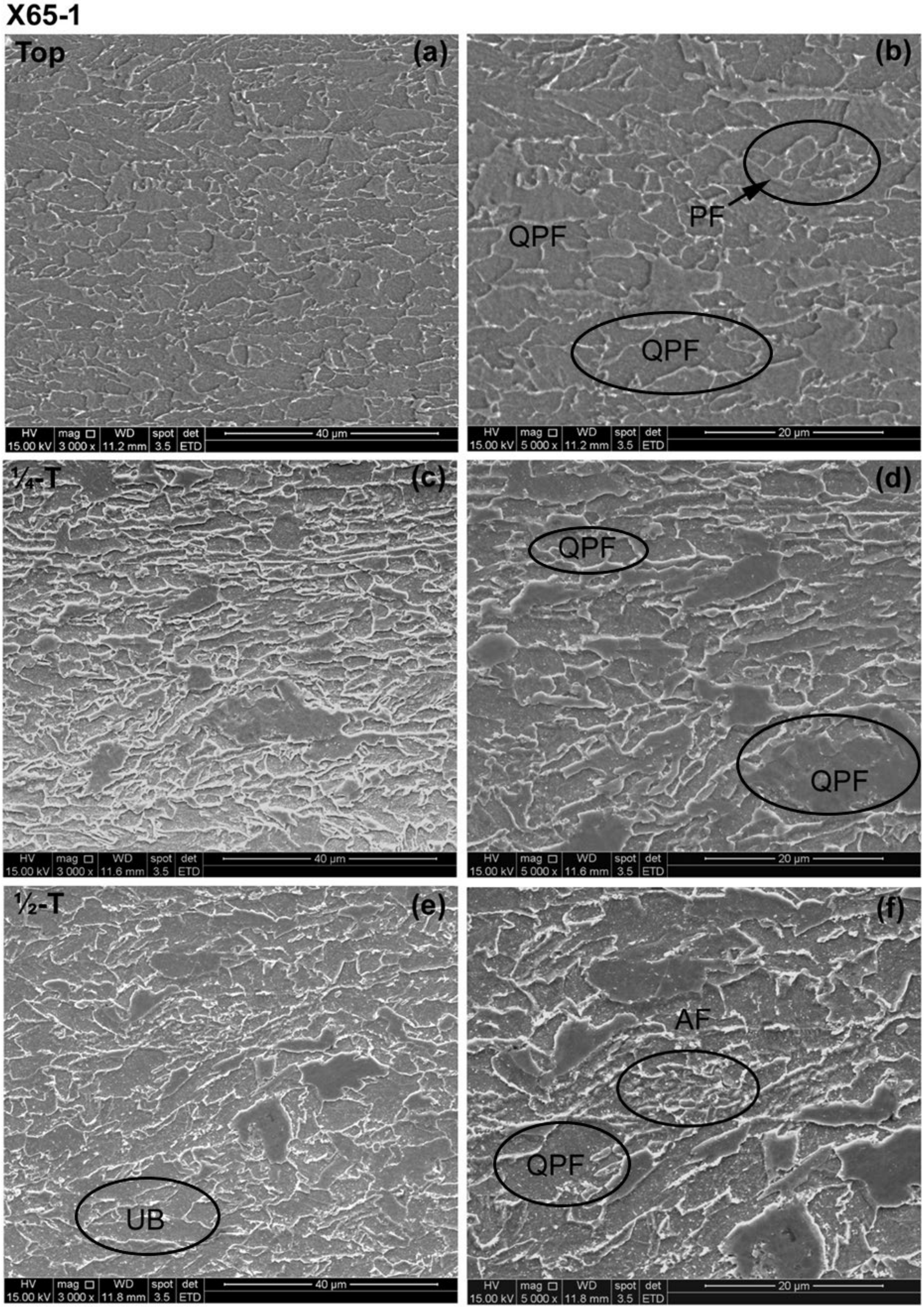

Figure 5.2 – SEM images of the X65-1 steel at the top, ¼ thickness, and ½ thickness, captured at two different magnifications using secondary electron mode.

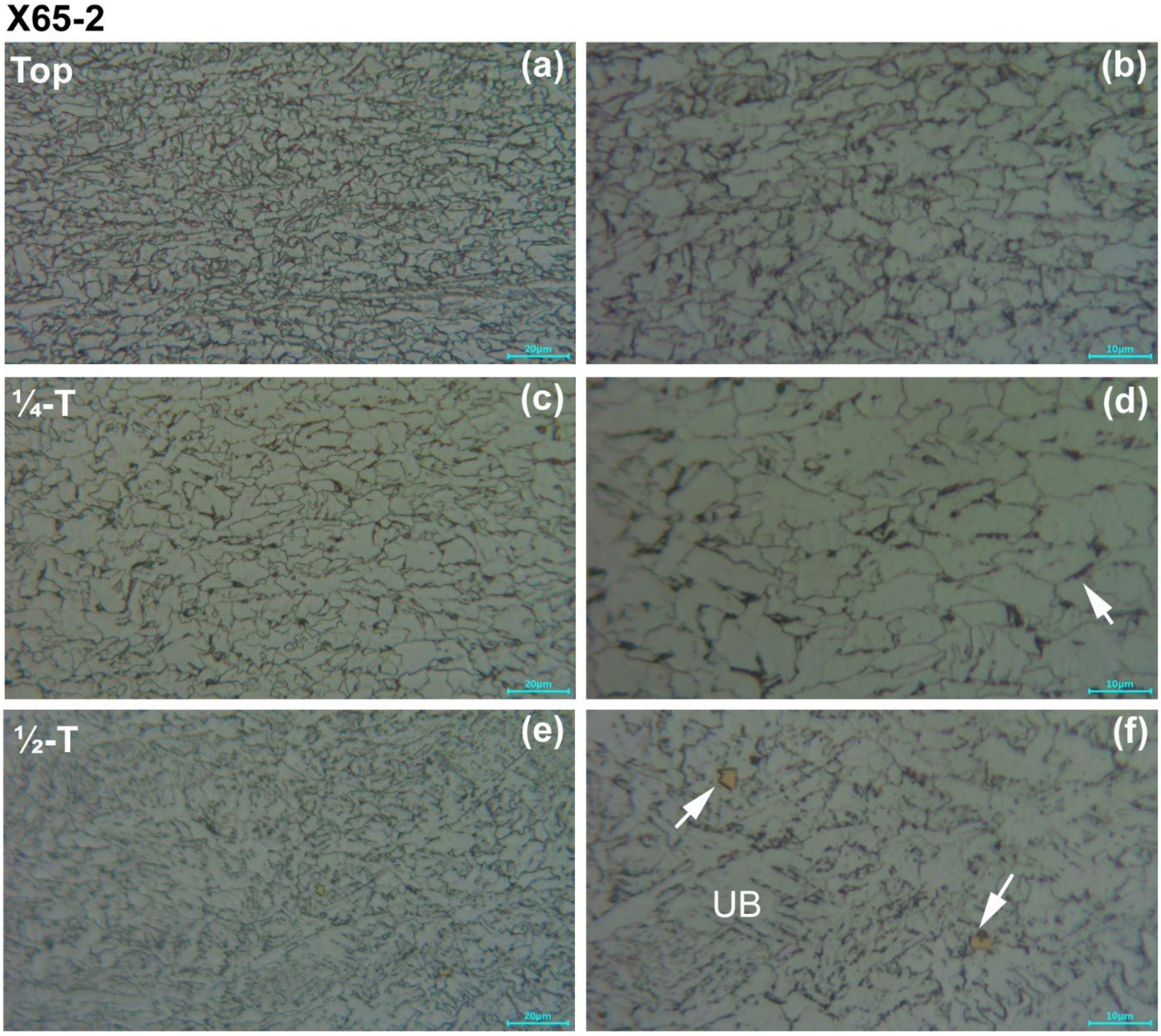

Figure 5.3 - OM images of the X65-2 steel obtained for the top, ¼ thickness, and ½ thickness at two different magnifications. In the images, the rolling direction of the steel plates is oriented horizontally.

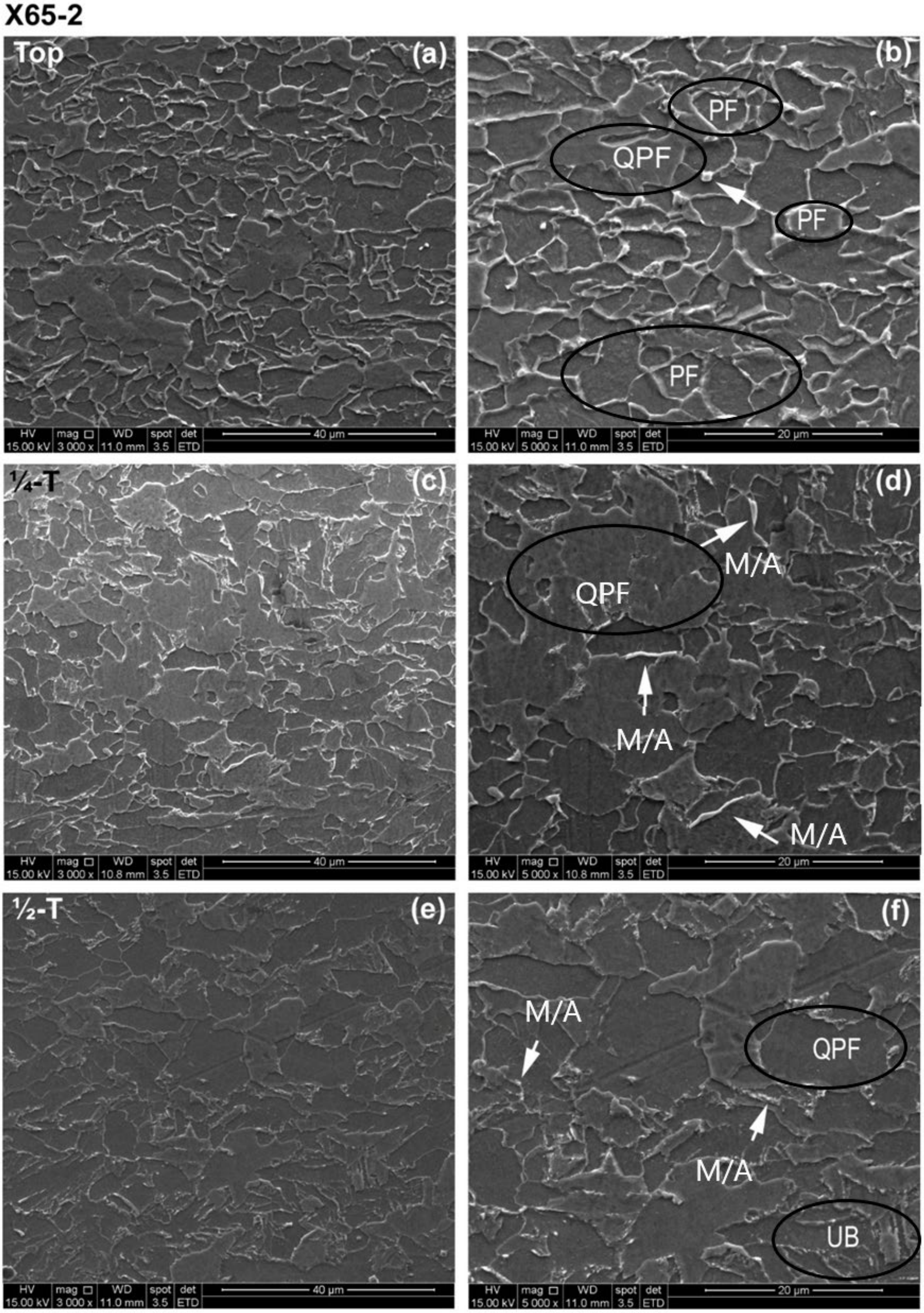

Figure 5.4 – SEM images of the X65-2 steel at the top, ¼ thickness, and ½ thickness, captured at two different magnifications using secondary electron mode.

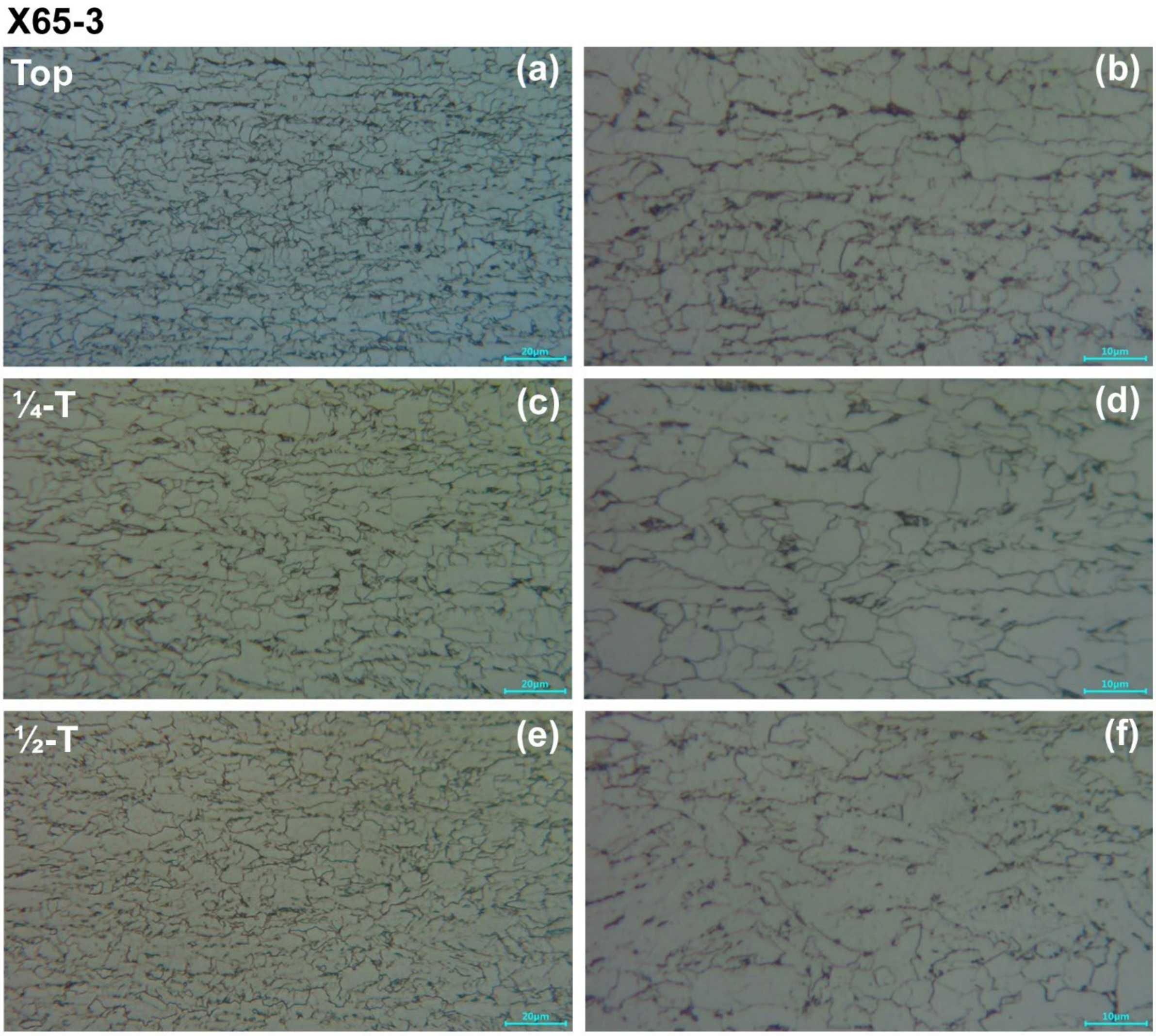

Figure 5.5 - OM images of the X65-3 steel obtained for the top, ¼ thickness, and ½ thickness at two different magnifications. In the images, the rolling direction of the steel plates is oriented horizontally.

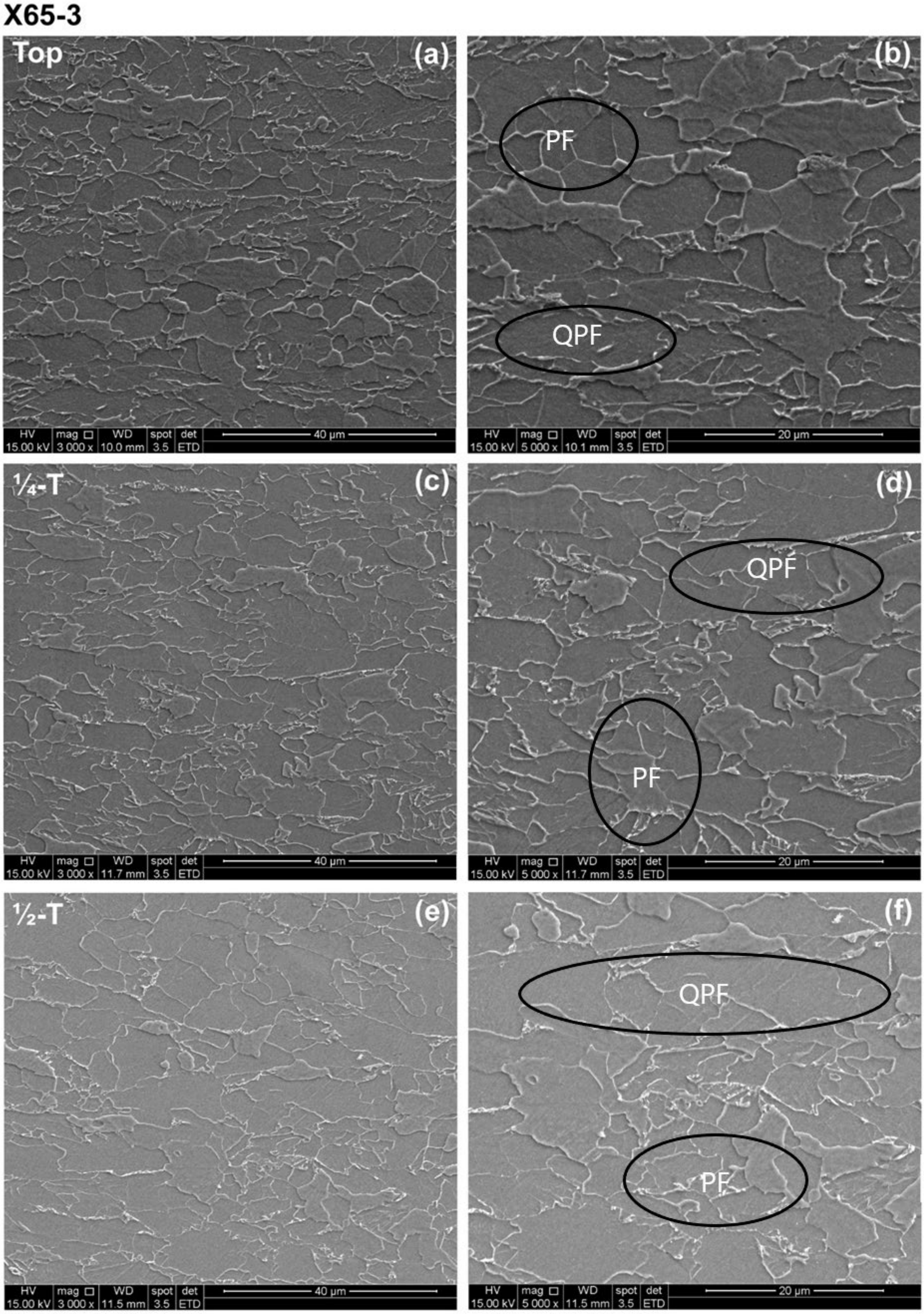

Figure 5.6 - SEM images of the X65-3 steel at the top, ¼ thickness, and ½ thickness, captured at two different magnifications using secondary electron mode.

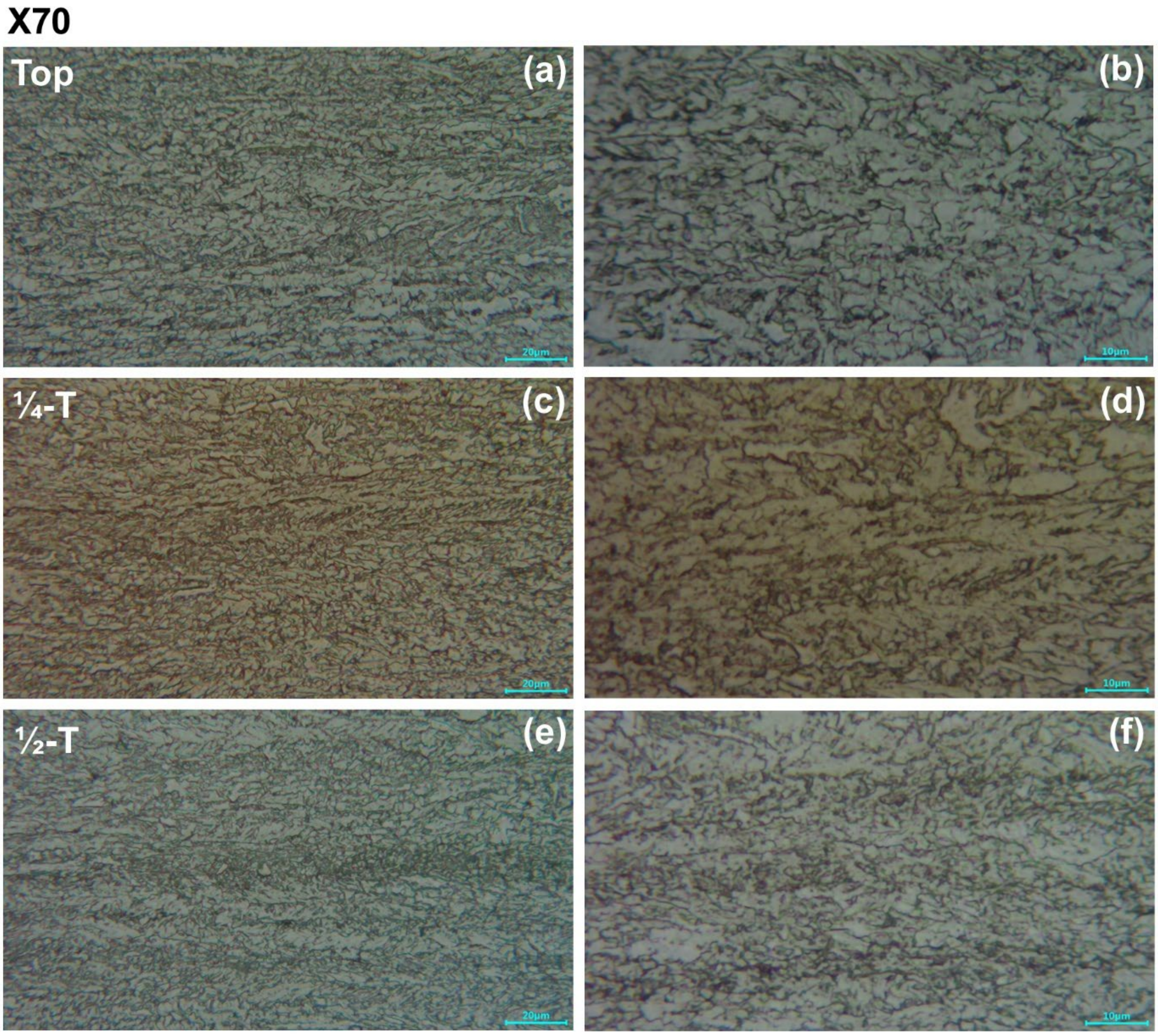

Figure 5.7 - OM images of the X70 steel obtained for the top, ¼ thickness, and ½ thickness at two different magnifications. In the images, the rolling direction of the steel plates is oriented horizontally.

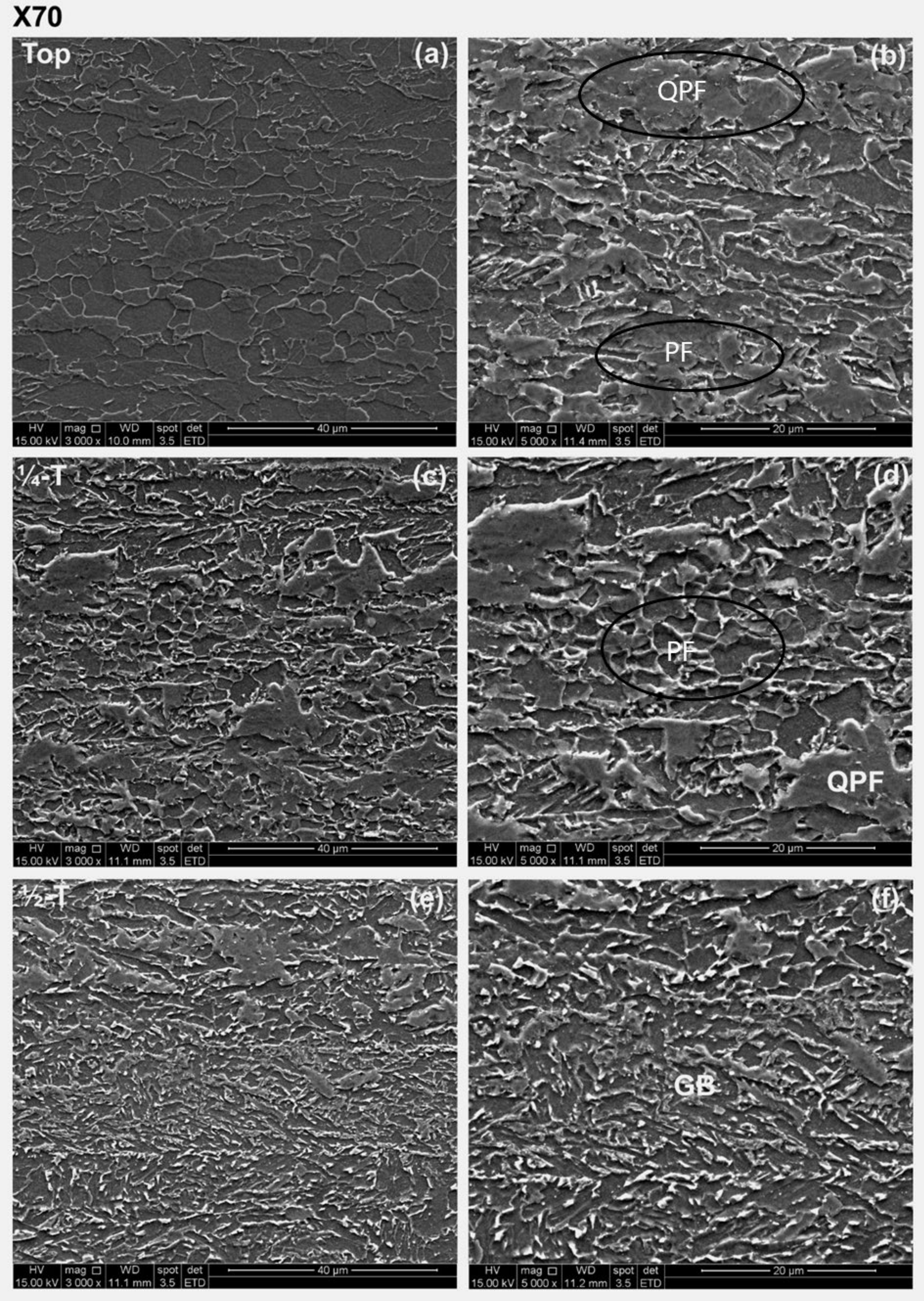

Figure 5.8 - SEM images of the X70 steel at the top, ¼ thickness, and ½ thickness, captured at two different magnifications using secondary electron mode.

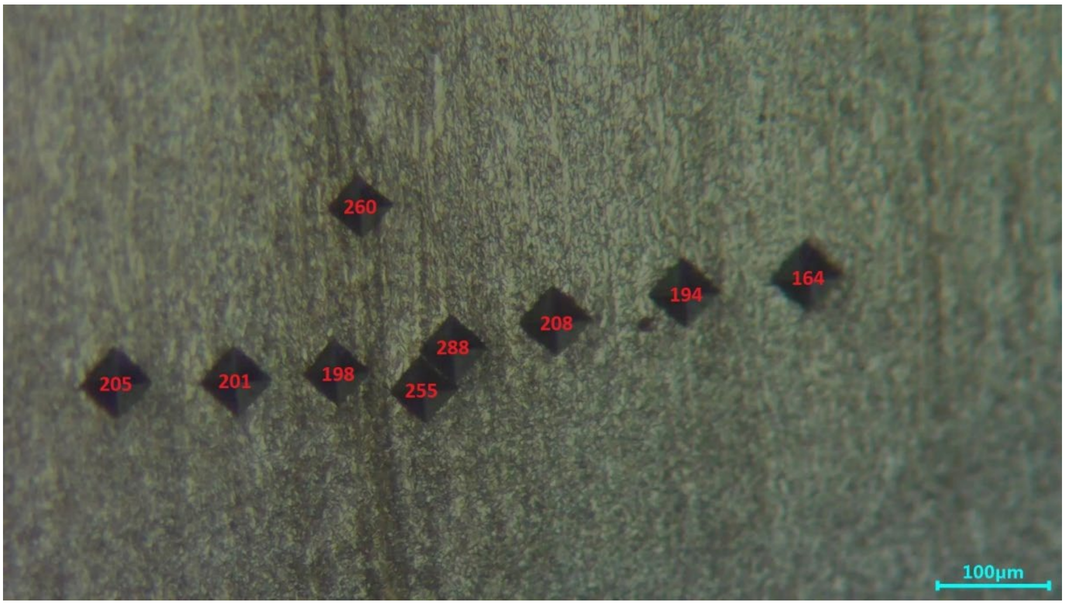

Figure 5.9 - Microhardness measurements along a banded region at the center of the X70 steel.

5.2. Through-Thickness Hydrogen Permeation Analysis

The hydrogen permeation test provides critical insights into the diffusion behavior of hydrogen through steel membranes. From the resulting permeation curves and by applying Eqs. (4.1) and (4.2), two key parameters were obtained: the effective diffusion coefficient (D_{eff}) and the apparent hydrogen solubility (C_0). The D_{eff} reflects the effective diffusivity of hydrogen, incorporating both the diffusing hydrogen and the fraction trapped at reversible microstructural sites. The C_0 represents the total hydrogen concentration, encompassing hydrogen in solid solution as well as that associated with reversible and irreversible traps.

Figures 5.10 and 5.11 display the measured values of D_{eff} and C_0, respectively, evaluated at three through-thickness locations - top surface, one-quarter thickness, and mid-thickness - for the four steels analyzed: X70, X65-1, X65-2, and X65-3.

In the X70 steel, the effective hydrogen diffusion coefficient (D_{eff}) progressively decreases from the surface to the mid-thickness, with values ranging from approximately 5.2×10^{-6} $cm^2\cdot s^{-1}$ at the surface to about 2.0×10^{-6} $cm^2\cdot s^{-1}$ at mid-thickness. Conversely, the subsurface hydrogen concentration (C_0) increases markedly at mid-thickness, reaching values close to 1.0×10^{-6} $mol\cdot cm^{-3}$, while remaining significantly lower at the top and quarter-thickness positions ($\sim4.0\times10^{-7}$ $mol\cdot cm^{-3}$). This inverse relationship between D_{eff} and C_0 is likely linked to the pronounced centerline segregation, as well as the significant presence of M/A constituents and second-phase particles at mid-thickness.

Segregated regions, enriched in solute elements and containing harder phases such as M/A, act as potent hydrogen traps, thereby reducing hydrogen diffusivity and promoting localized hydrogen accumulation. It is well established that M/A constituents serve as strong hydrogen-trapping sites, a behavior attributed to the high dislocation density typically present in martensite, which significantly promotes hydrogen-trapping capability [86; 88].

In X65-1, the highest D_{eff} is observed at the 1/4-thickness position ($\sim5.9\times10^{-6}$ cm$^2\cdot$s^{-1}), while lower values are measured at the top and mid-thickness. Correspondingly, the hydrogen concentration C_0 is highest at the surface ($\sim7.5\times10^{-7}$ mol$\cdot$cm^{-3}) and lower at the quarter and mid-thickness positions. The microstructure at ¼ thickness is characterized by a finer grain size and a higher fraction of acicular ferrite (AF), which promotes more efficient hydrogen transport due to its highly larger amount of grain boundaries acting as fast diffusion paths. In contrast, the top and mid-thickness regions, which are dominated by quasi-polygonal ferrite (QPF) with the presence of large, elongated inclusions, tend to trap hydrogen more effectively, leading to higher C_0 and reduced D_{eff}.

In X65-2, both D_{eff} and C_0 values remain relatively consistent throughout the plate thickness, showing only minor variations around 4.0×10^{-6} cm$^2\cdot$s^{-1} for D_{eff} and between 4.0 and 5.0×10^{-7} mol$\cdot$cm^{-3} for C_0. This behavior correlates with the microstructure, which is predominantly ferritic (PF + QPF) throughout the thickness, with only a small, localized presence of upper bainite (UB) and inclusions at mid-thickness. The homogeneous ferritic matrix, free from significant amounts of second-phase particles or severe segregation, results in more uniform hydrogen diffusion and trapping characteristics.

Similarly, X65-3 exhibits consistent D_{eff} and C_0 values across the thickness, with slightly higher hydrogen concentrations ($\sim6.0\times10^{-7}$ mol$\cdot$cm^{-3}) at the quarter and mid-thickness positions. The microstructure of X65-3 is highly homogeneous, composed entirely of PF and QPF, without evidence of upper bainite or non-metallic inclusions. The absence of strong hydrogen traps and the uniformity of the microstructure contribute to the observed homogeneous hydrogen transport behavior.

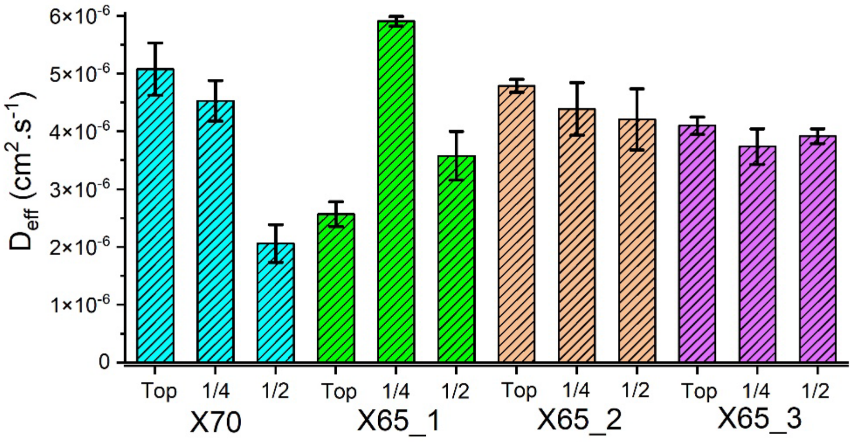

Figure 5.10 – Values of the effective hydrogen diffusion coefficient (D_{eff}) obtained for the three X65 steels and one X70 steel across the thickness of each, at three positions: top, ¼ thickness, and ½ thickness.

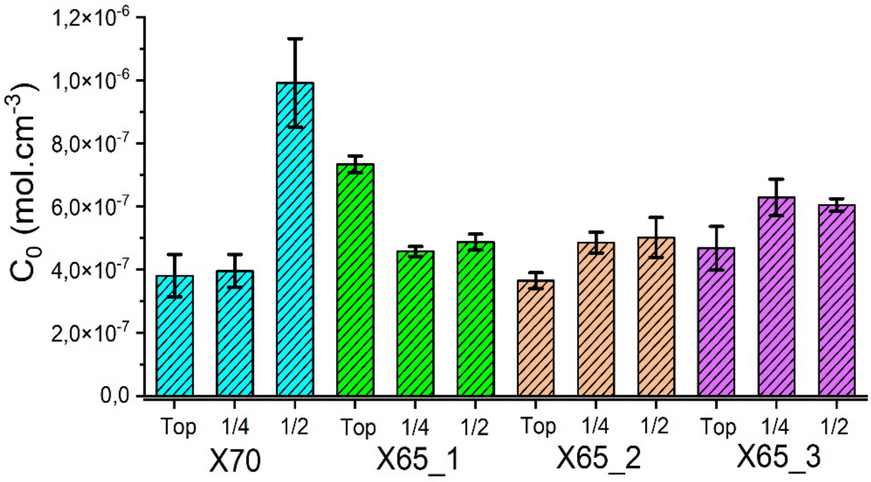

Figure 5.11 - Values of the apparent hydrogen solubility (C0) obtained for the three X65 steels and one X70 steel across the thickness of each, at three positions: top, ¼ thickness, and ½ thickness.

5.3. Evaluation of HIC Tests: Ultrasonic and Microstructural Analysis

Hydrogen-induced cracking (HIC) tests were conducted on specimens of the four steels, performed in triplicate, following the NACE TM0284 standard [11] using Solution A, and immediately evaluated by ultrasonic scanning (US). Figure 5.12 presents top-view ultrasonic scan images of the X65 and X70 steels. The US scan covers the full thickness of the plates, ranging from 0 to 32 mm, with green indicating full thickness (32 mm), yellow representing approximately half thickness (16 mm), and red corresponding to the opposite surface (0 mm).

The results reveal that the X65 steels - X65-1, X65-2, and X65-3 (Figures 5.11-a, b, and c) - were practically unaffected by the test conditions. All specimens exhibited predominantly green regions across the scanned surfaces, indicating full-thickness integrity and no evidence of significant blistering or central cracking. Only minor, isolated indications were observed in X65-2, corresponding to small, localized discontinuities.

In contrast, the X70 steel (Figure 5.12-d) exhibited extensive damage in all three specimens. The US scans revealed widespread yellow areas indicative of mid-thickness damage, along with several red regions associated with near-surface cracking, suggesting severe central cracking and multiple surface blisters.

To further elucidate the damage mechanisms in the X70 steel, a detailed microstructural characterization was performed. Optical microscopy images (Figure 5.13) revealed cracks localized at mid-thickness (Figures 5.13-a and 5.13-b) and subsurface blistering (Figure 5.13-c). Scanning electron microscopy images confirmed the stepwise propagation of hydrogen-induced cracks, a phenomenon commonly referred to as stepwise cracking (SWC) (Figure 5.14-a). Furthermore, the interaction between the crack path and the surrounding microstructure is evident (Figure 5.14-b), including evidence of decohesion at the interfaces between non-metallic precipitates and the metallic matrix (Figure 5.14-c).

SEM-EDS chemical mapping of the cracking region is shown in Figures 5.15 and 5.16. The Fe elemental map shows a uniform distribution throughout the matrix. The C map reveals enrichment along the crack and adjacent areas, which is attributed both to metallographic preparation artifacts and to the presence of martensite-austenite (M/A) constituents. The Mn map highlights significant enrichment along the crack path and in segregated bands, suggesting that crack propagation is strongly associated with Mn-rich regions. This elemental segregation promotes localized hardening (as revealed in Figure 5.9) and embrittlement, thereby increasing the susceptibility of these areas to crack initiation and growth.

The Si and Cr maps exhibit relatively uniform distributions across the matrix. In contrast, the Ti and Nb maps reveal isolated, highly enriched particles - likely corresponding to complex carbonitride precipitates, such as (Ti,Nb)(C,N) - marked by white arrows in Figure 5.15. These precipitates are undissolved, extremely hard, brittle, and non-coherent with the metallic matrix; as such, they act as potent stress concentrators and potential crack initiation sites [88]. A comparative analysis between Figures 5.15 and 5.16 indicates that the Nb- and Ti-rich particles display a more polygonal morphology in Figure 5.15, whereas in Figure 5.16 they appear more elongated.

The experimental observations obtained in this study - notably the preferential crack propagation along Mn-segregated bands and regions containing M/A constituents in the X70 steel - are in strong agreement with findings reported in the literature [83;84].

Centerline segregation concentrates Mn (and C, P, Mo) in the axial band, raising hardenability and forming harder pearlite/bainite/MA-rich regions that act as preferred paths for HIC initiation and linkage[14].

In Shabalov et al., [15] the maximum hardness at mid-thickness crosses the HIC-sensitive threshold (≈HV260) when Mn is 1.50% (~300 HV at ½-t versus <240 HV at ¼-t), while lowering Mn to 1.20% brings both conditions below the critical hardness and reduces through-thickness contrast—thereby improving HIC resistance. Because Mn segregation rises sharply once total Mn exceeds ~1.0%, reducing Mn mitigates the centerline hardness spike and increases microstructural homogeneity.

Consistent with this, many authors recommend Mn ≤1.20% to curb central segregation and enhance HIC resistance (especially with older CCM slabs); when strength limits constrain further Mn/C reductions, a balanced design using Cr, Ni, Cu and higher Nb can meet mechanical targets without sacrificing HIC performance[16].

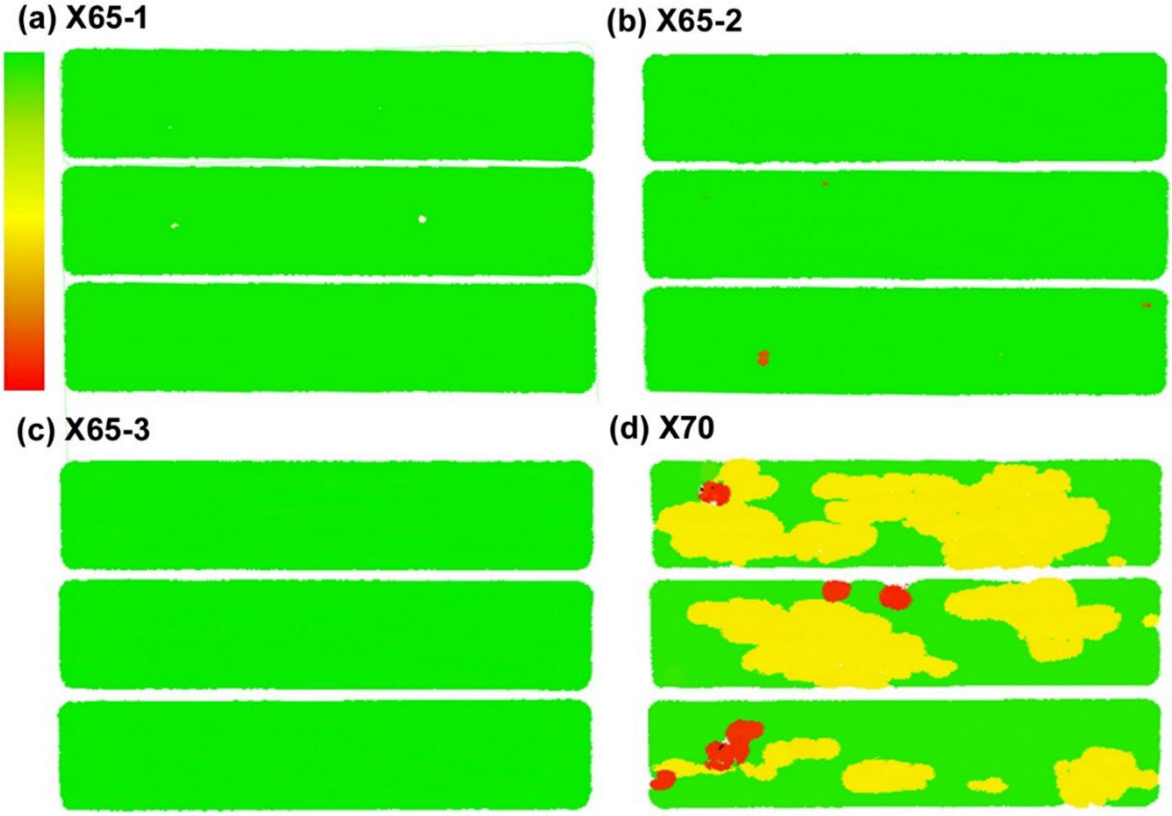

Figure 5.12 - Top-view ultrasonic scan images of the X65 and X70 steels after the HIC tests, which were performed in triplicate.

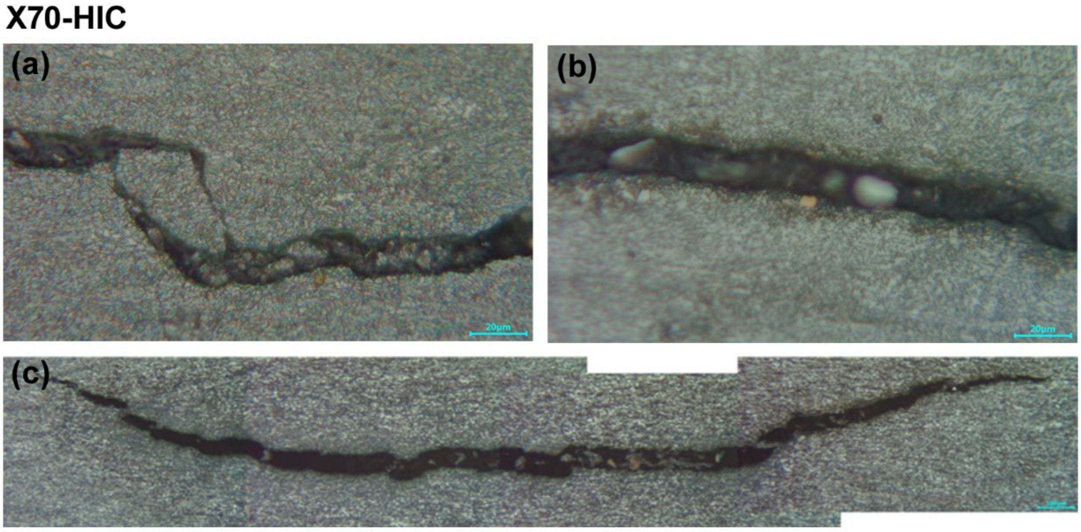

Figure 5.13 - Optical microscopy images of the X70 steel after the HIC test. The images, obtained at ½ thickness, show extensive cracks (a, b) and a subsurface blister (c).

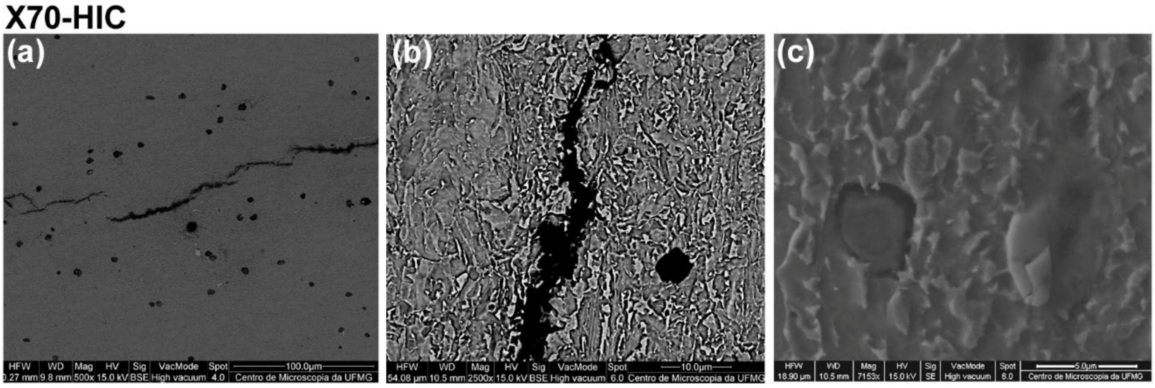

Figure 5.14 - SEM images of the X70 steel after the HIC test at mid-thickness region.

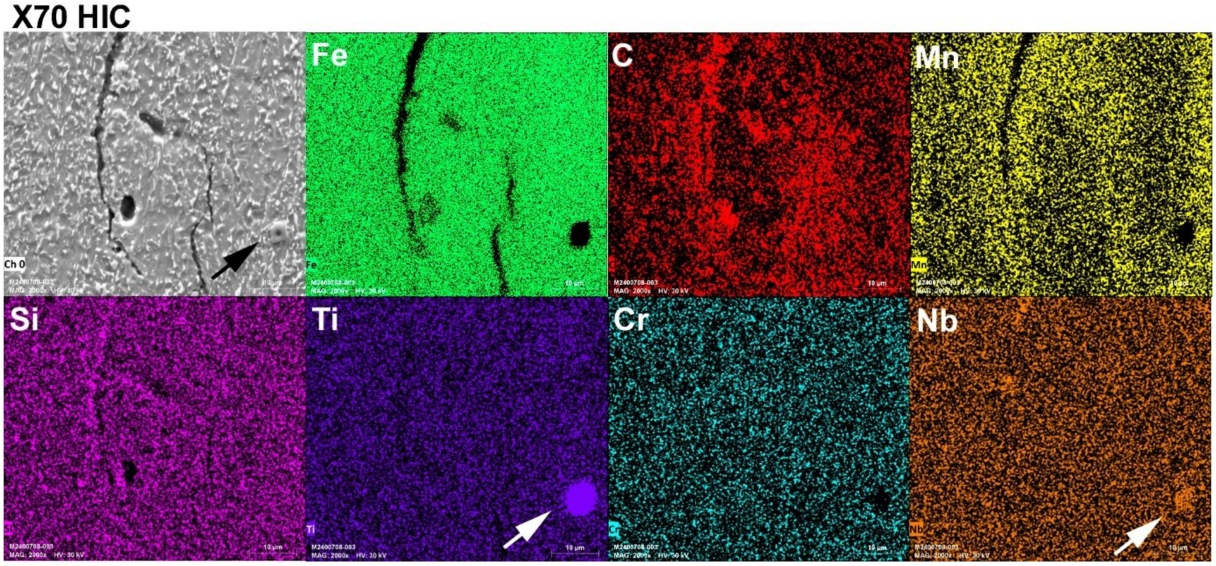

Figure 5.15 – SEM-EDS of the X70 steel after the HIC test at mid-thickness region.

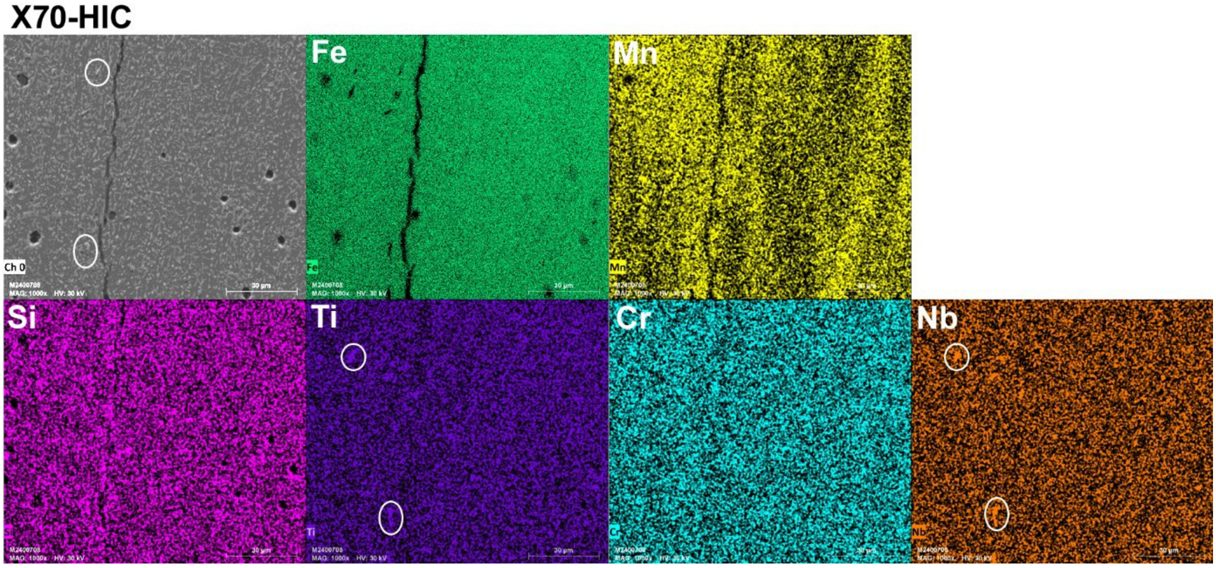

Figure 5.16 – SEM-EDS of the X70 steel after the HIC test at mid-thickness region.

5.4. SSRT Testing and Fractographic Examination

Figures 5.17 to 5.20 show the SSRT curves obtained at room temperature for both uncharged and hydrogen-charged X65-1 (HTP), X65-2, X65-3, and X70 steels with duplicate tests performed for each condition. All tests were performed on specimens extracted at ¼ of the plate thickness and oriented at 0° to the rolling direction. For each steel, part (a) of the figure presents the stress-strain curve for the uncharged specimen, while part (b) presents the curve for the hydrogen-charged specimen: Figures 5.17 shows the results for X65-1, Figure 5.18 for X65-2, Figure 5.19 for X65-3, and Figure 5.20 for X70.

Figures 5.21 to 5.23 presents the compiled average mechanical property values for the three X65 steels and the X70 steel. This figure compares the yield strength (YS), ultimate tensile strength (UTS), and total strain (ε_T) for the different steel variants at one-quarter thickness (¼-T), evaluated both with and without hydrogen charging. Blue bars correspond to uncharged specimens, while red bars represent hydrogen-charged specimens.

Figure 5.21 reveals a slight increase in yield strength for all steels following hydrogen charging. This effect is especially pronounced in the X65-2-H specimen, which exhibits a noticeably higher yield strength compared to its uncharged counterpart. This behavior may be attributed to hydrogen-induced localized hardening, resulting from the interaction between hydrogen atoms and dislocations, which restricts dislocation motion during the early stages of plastic deformation.

Figure 5.22 shows that the ultimate tensile strength (UTS) is largely unaffected by hydrogen charging in most cases. Subtle variations are observed, including a slight decrease in UTS for the X65-1-H and X65-3-H specimens and a minor increase for X65-2-H. The UTS values for the X70 steel remain essentially unchanged between the charged and uncharged conditions.

In contrast, Figure 5.23 highlights a more significant impact of hydrogen on ductility. The X70-H specimen displays a marked reduction in total strain, indicating a high susceptibility to hydrogen-induced embrittlement. The X65 steels, on the other hand, exhibit only minor changes in ductility upon hydrogen charging.

The differences in mechanical properties observed in the X65-3 steel, compared to the other X65 variants, can be directly attributed to its microstructural characteristics. The predominance of polygonal and quasi-polygonal ferrite contributes to its lower yield and ultimate tensile strengths, while enhancing ductility.

To further assess the hydrogen embrittlement susceptibility of the X65 steels, the fracture surfaces of specimens tested by SSRT were examined. Figures 5.24 and 5.25 show the fracture surfaces of X65-1 under uncharged and hydrogen-charged conditions, respectively. Figures 5.26 and 5.27 correspond to X65-2 in the same conditions, while Figures 5.28 and 5.29 present the results for X65-3. High-magnification images revealed a predominantly dimpled fracture morphology across the entire cross-section of both uncharged and hydrogen-charged specimens, regardless of the steel variant.

Figure 5.30 presents SEM images of the fracture surface of an uncharged X70 specimen, revealing a ductile morphology characterized by the presence of dimples. In contrast, Figure 5.31 shows the fracture surface of a hydrogen-charged X70 specimen, where a clear boundary between ductile and brittle fracture regions is observed. In Figure 5.32 the boundary between ductile and fragile regions is explicated.

SSA is the time-dependent strengthening that occurs when a plastically prestrained ferritic steel is held at modest temperature. During the hold, fast interstitials diffuse toward the hydrostatic field of edge dislocations and form Cottrell atmospheres, lowering the elastic energy and locking the dislocations. On reloading, an extra stress is required to free/bypass the locked dislocations, which produces a discontinuous yield. [leslie]

Hydrogen is a highly mobile interstitial in α-Fe; during charging it segregates to dislocation cores and nearby tensile zones, forming H-Cottrell atmospheres that lock dislocations. In a subsequent tensile test, the stress first rises to an upper yield point required to unlock or break these atmospheres from the pinned dislocation population. Once unlocking begins locally, a Lüders band nucleates and propagates at roughly constant stress while the H atmospheres along its path are progressively disrupted or redistributed, producing a plateau. The flow stress remains near this level until a sufficient fraction of atmospheres is consumed, after which the band has traversed the gauge length and uniform work hardening resumes.[leslie]

All hydrogen-charged specimens exhibited a Lüders plateau (Figs. 5.17–5.20), and the yield strength of the three X65 variants increased relative to the uncharged condition (Fig. 4.21), indicating the occurrence of SSA

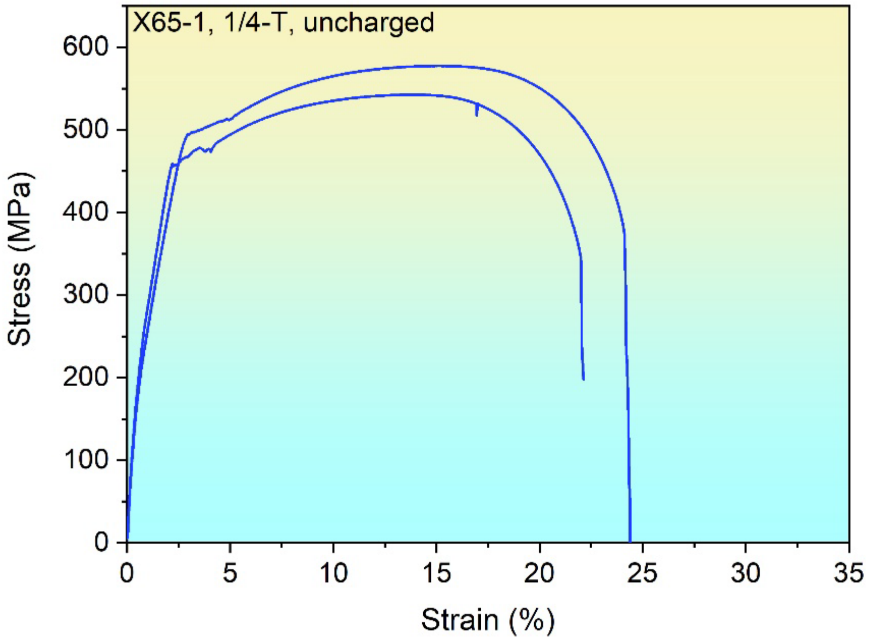

(a)

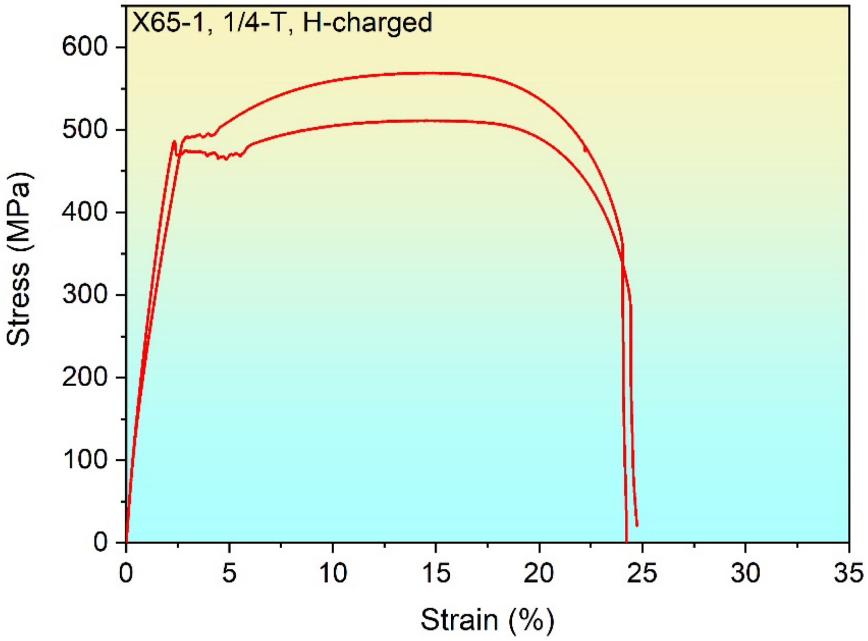

(b)

Figure 5.17 - Stress–strain curves obtained during the SSRT tests for the X65-1 steel specimens: (a) hydrogen-uncharged and (b) hydrogen-charged specimens. All tests were conducted on the region of the specimens corresponding to ¼ of the thickness.

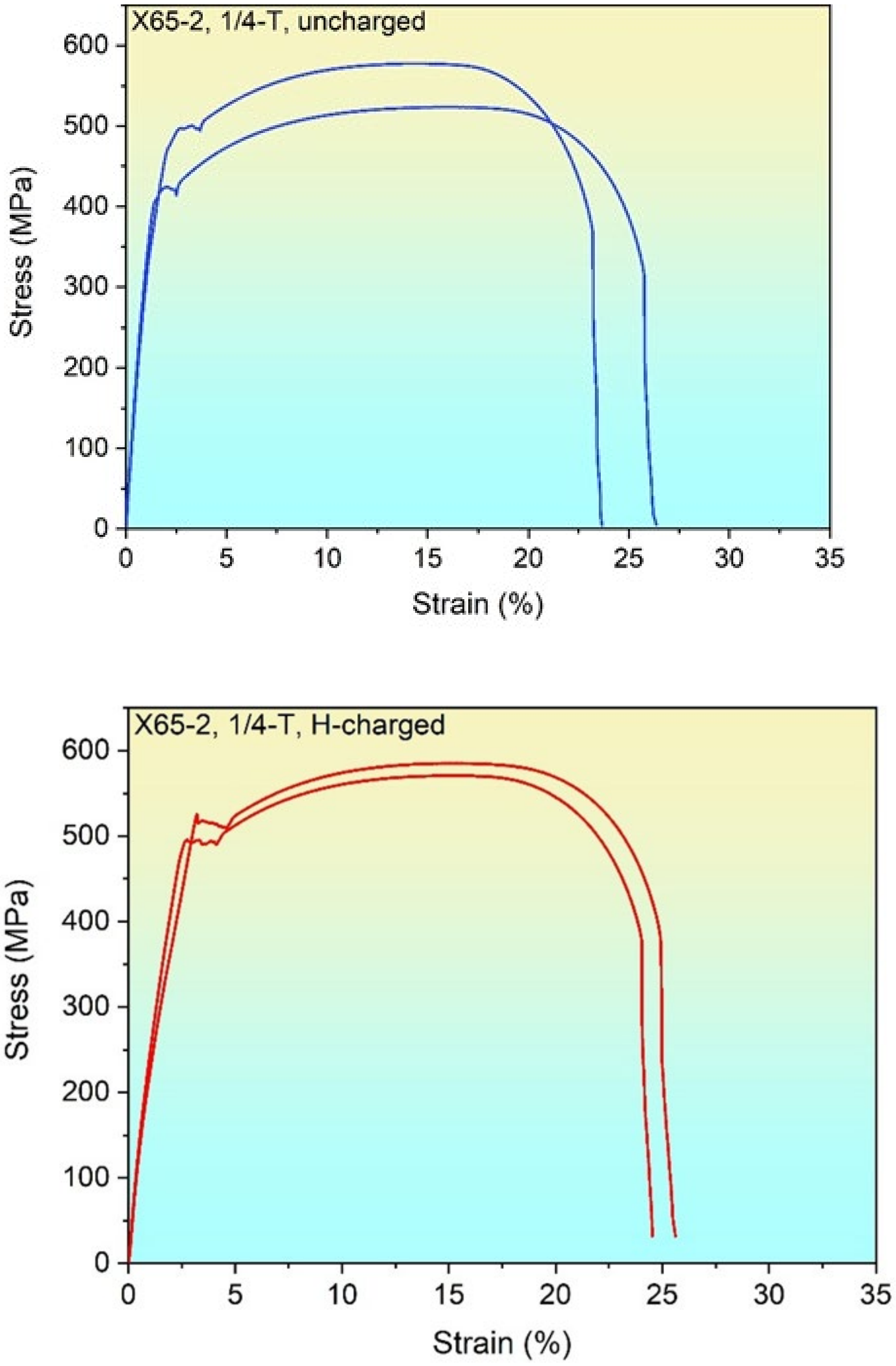

(a)

(b)

Figure 5.18 – Stress–strain curves obtained during the SSRT tests for the X65-2 steel specimens: (a) hydrogen-uncharged and (b) hydrogen-charged specimens. All tests were conducted on the region of the specimens corresponding to ¼ of the thickness.

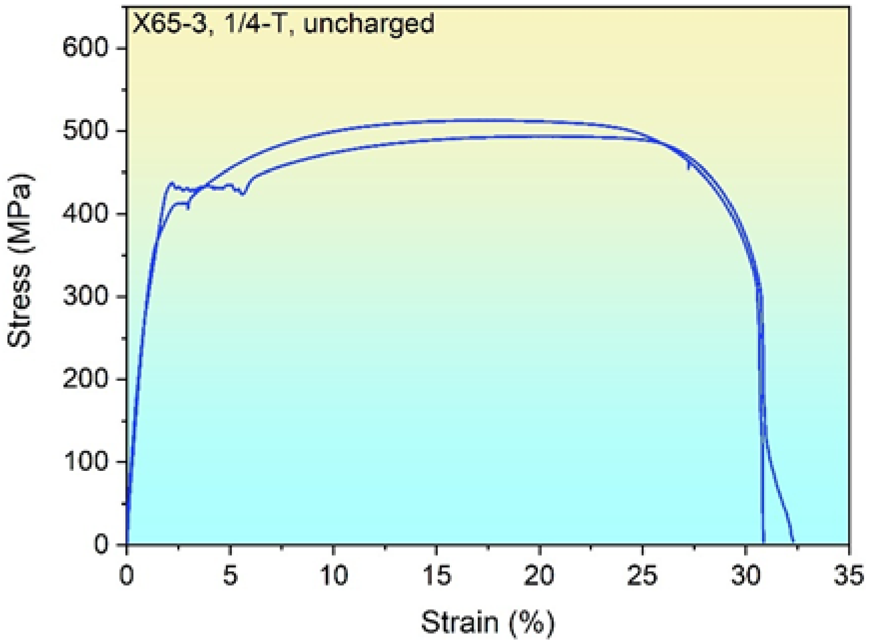

(a)

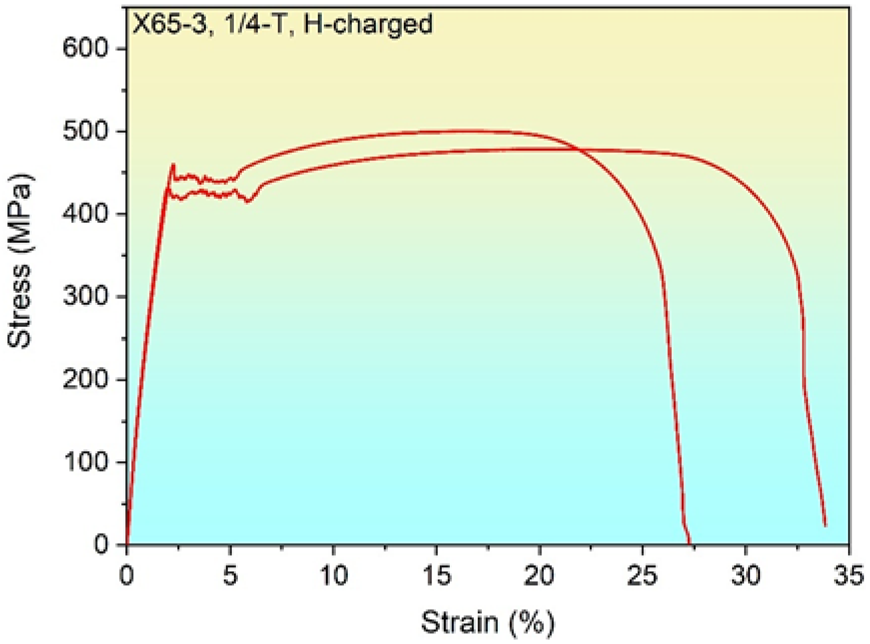

(b)

Figure 5.19 - Stress–strain curves obtained during the SSRT tests for the X65-3 steel specimens: (a) hydrogen-uncharged and (b) hydrogen-charged specimens. All tests were conducted on the region of the specimens corresponding to ¼ of the thickness.

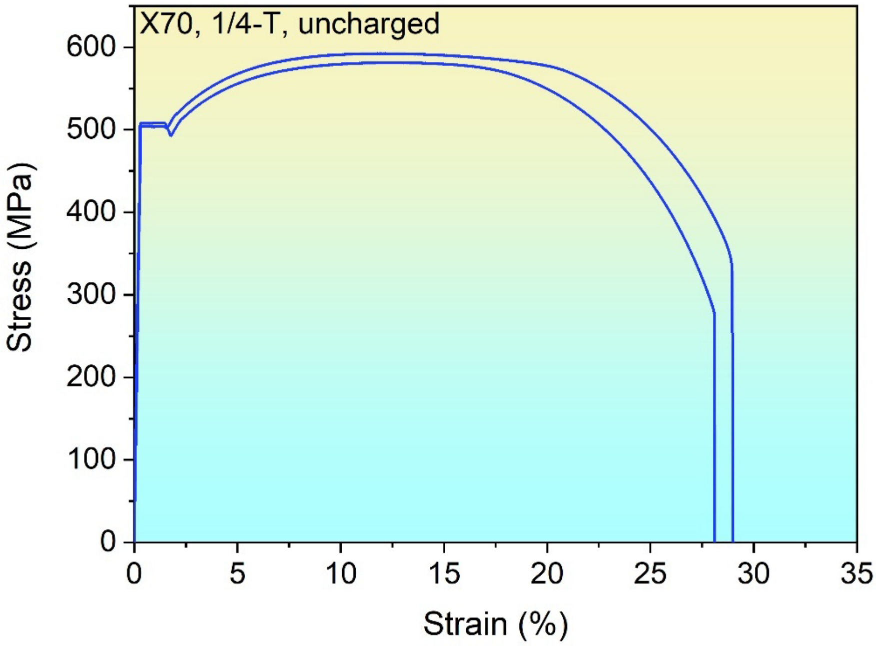

(a)

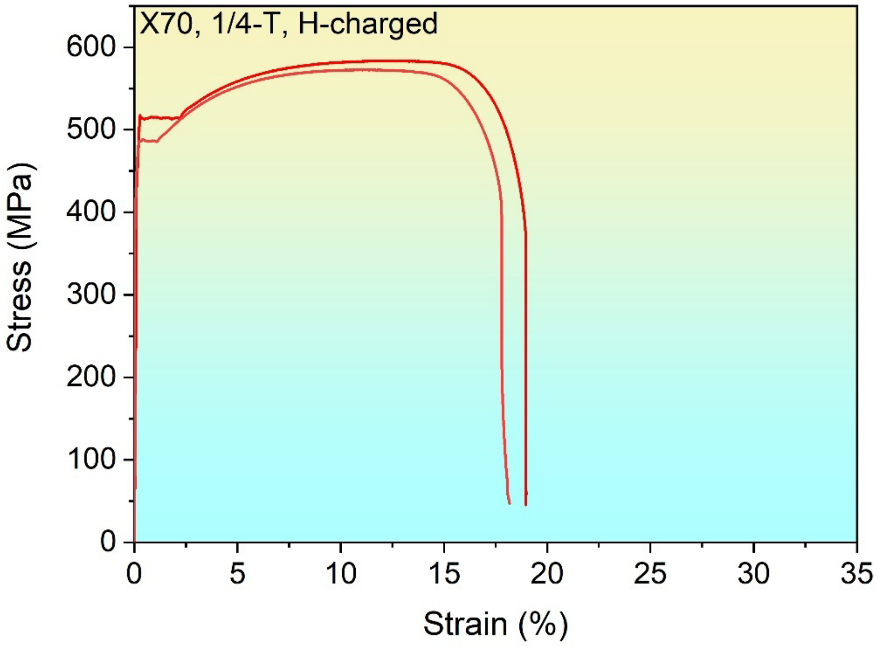

(b)

Figure 5.20 - Stress–strain curves obtained during the SSRT tests for the X65-3 steel specimens: (a) hydrogen-uncharged and (b) hydrogen-charged specimens. All tests were conducted on the region of the specimens corresponding to ¼ of the thickness.

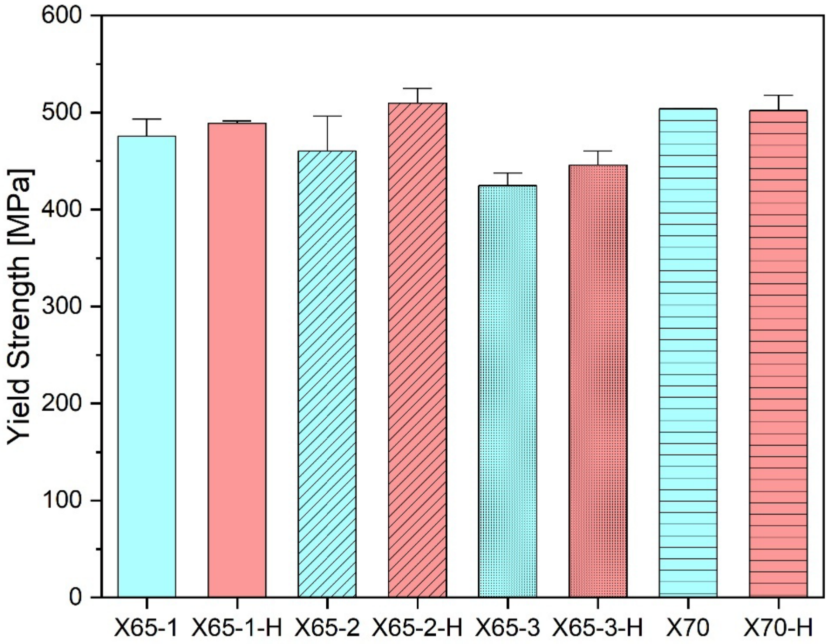

Figure 5.21 - Average yield strength values for the three X65 steels and the X70 steel at one-quarter thickness, comparing uncharged and hydrogen-charged (H) specimens. Blue bars indicate uncharged specimens, while red bars represent hydrogen-charged one.

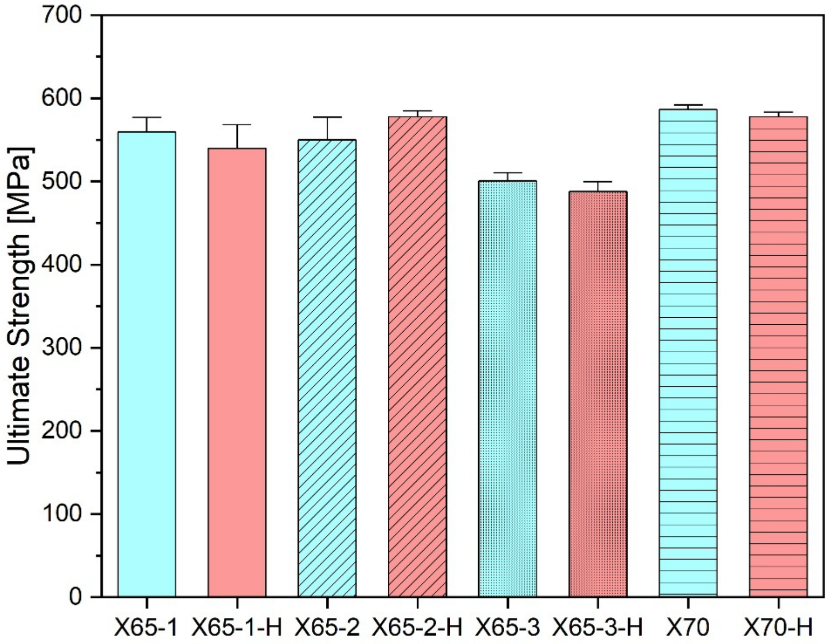

Figure 5.22 - Average ultimate tensile strength at ¼ thickness for X65 and X70 steels, comparing uncharged (blue) and hydrogen-charged (red) specimens.

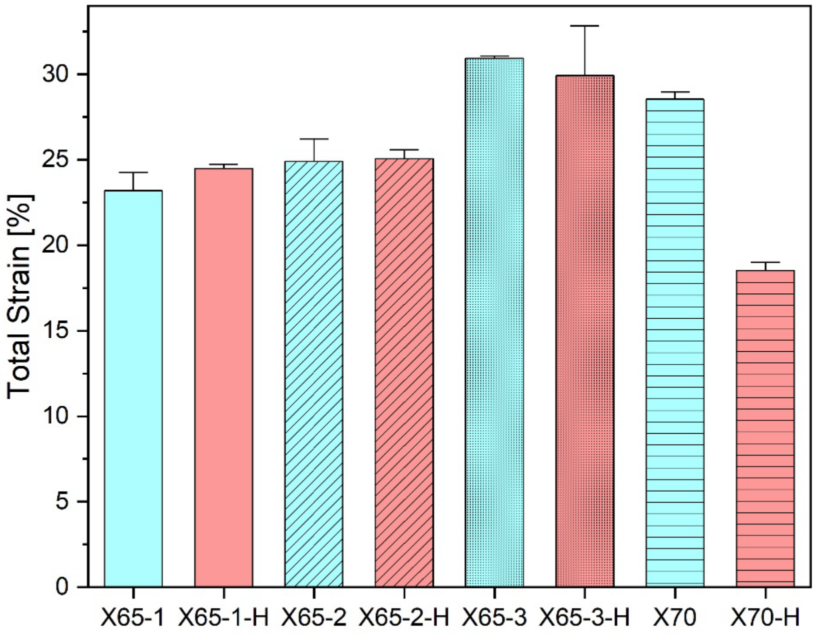

Figure 5.23 - Average total strain at ¼ thickness for X65 and X70 steels, comparing uncharged (blue) and hydrogen-charged (red) specimens.

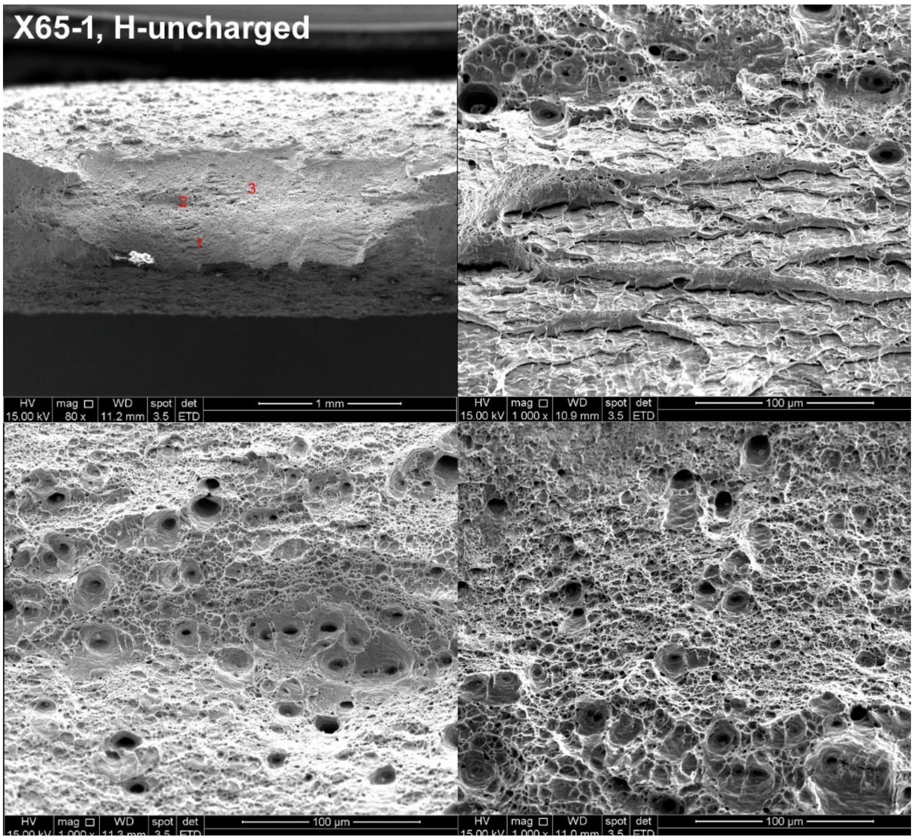

Figure 5.24 - Fracture surface of the X65-1 steel SSRT specimen in the hydrogen-uncharged condition. The test conducted on the region of the specimen corresponding to ¼ of the thickness.

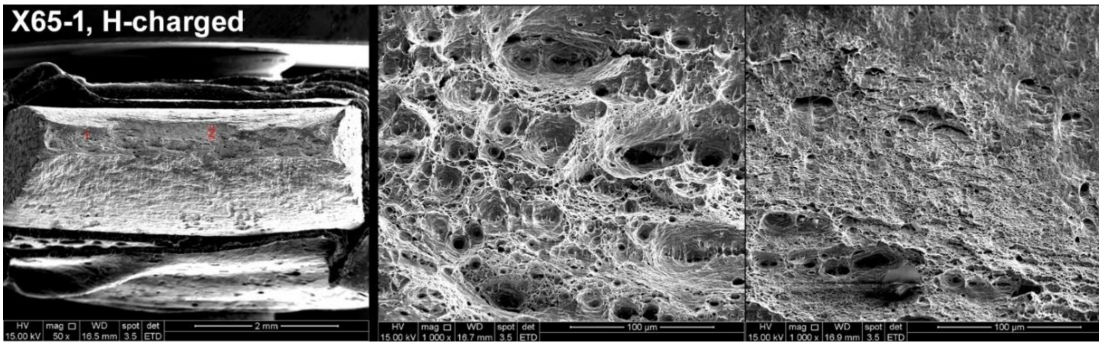

Figure 5.25 - Fracture surface of the X65-1 steel SSRT specimen in the hydrogen-charged condition. The test conducted on the region of the specimen corresponding to ¼ of the thickness.

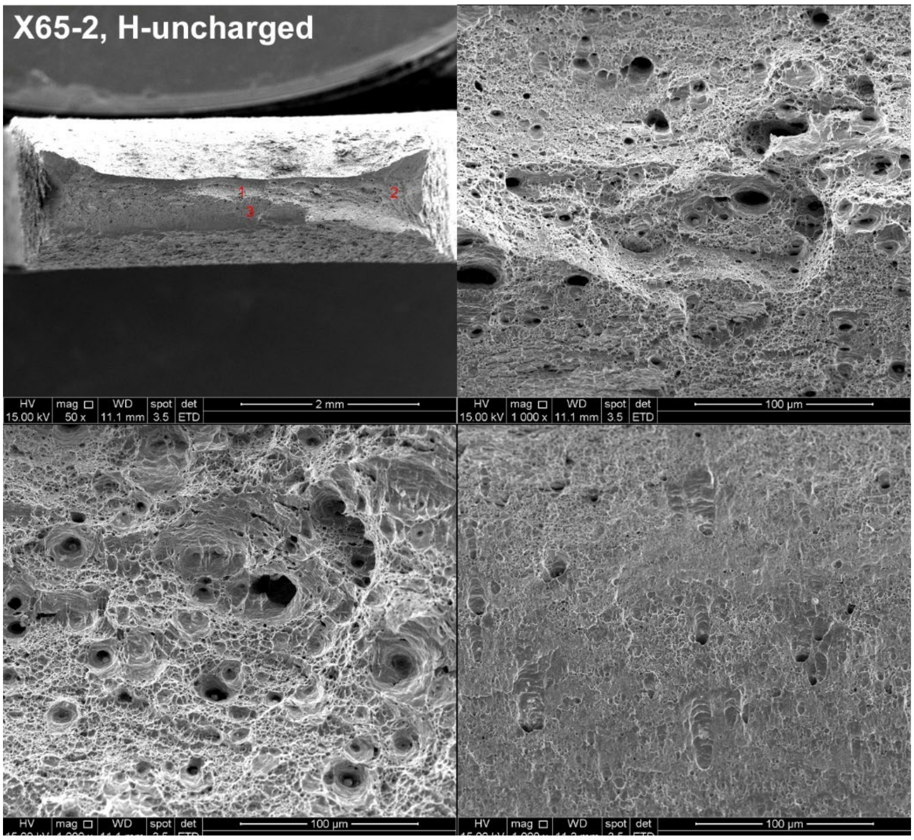

Figure 5.26 - Fracture surface of the X65-2 steel SSRT specimen in the hydrogen-uncharged condition. The test conducted on the region of the specimen corresponding to ¼ of the thickness.

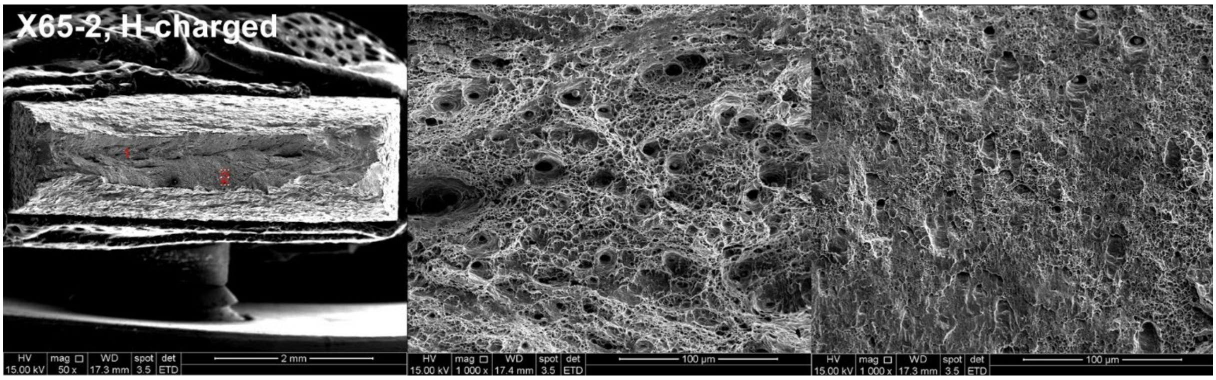

Figure 5.27 - Fracture surface of the X65-2 steel SSRT specimen in the hydrogen-charged condition. The test conducted on the region of the specimen corresponding to ¼ of the thickness.

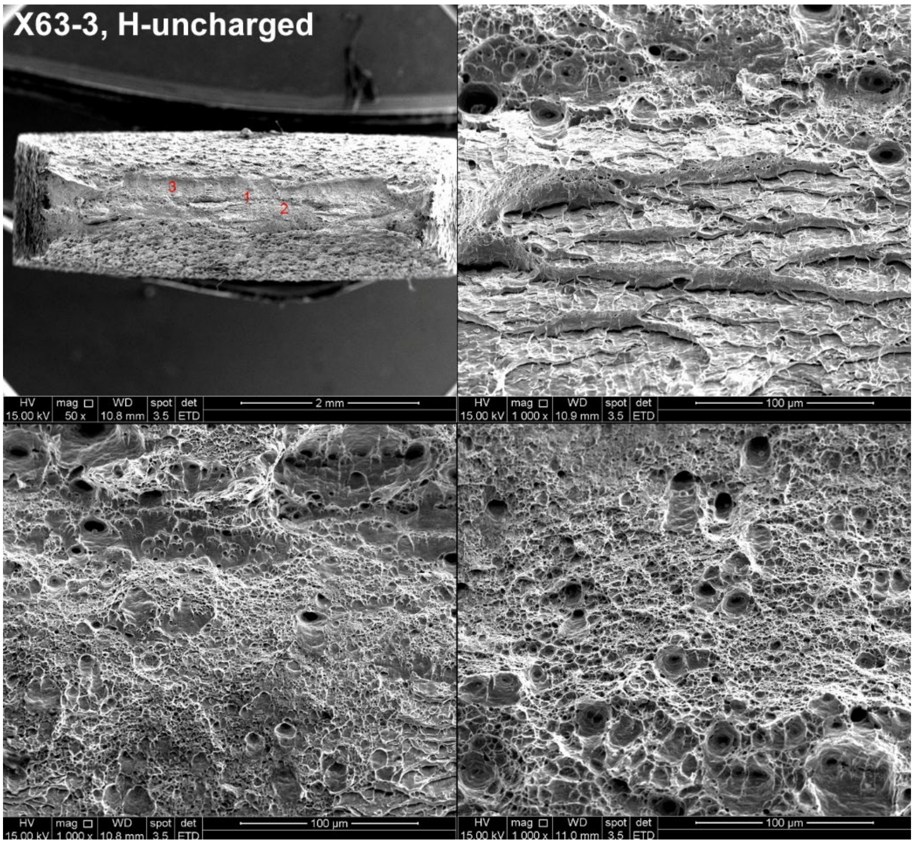

Figure 5.28 - Fracture surface of the X65-3 steel SSRT specimen in the hydrogen-uncharged condition. The test conducted on the region of the specimen corresponding to ¼ of the thickness.

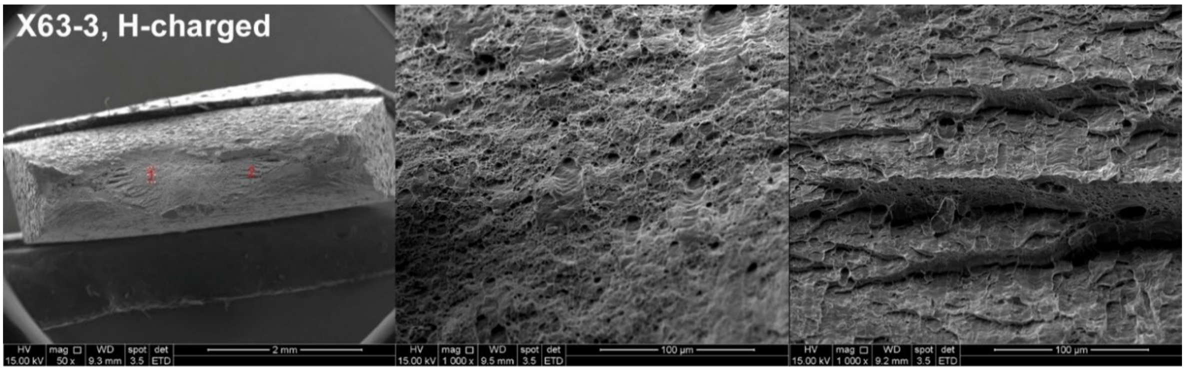

Figure 5.29 - Fracture surface of the X65-3 steel SSRT specimen in the hydrogen-charged condition. The test conducted on the region of the specimen corresponding to ¼ of the thickness.

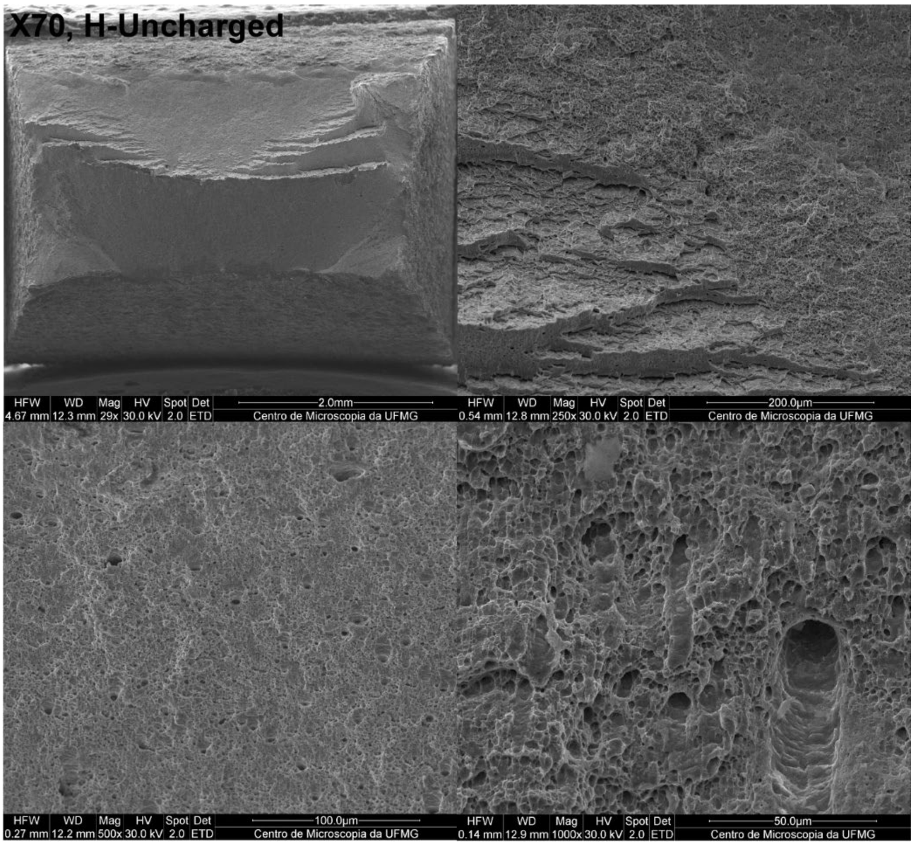

Figure 5.30 – Fracture surface of the X70 steel SSRT specimen in the hydrogen-uncharged condition. The test conducted on the region of the specimen corresponding to ¼ of the thickness.

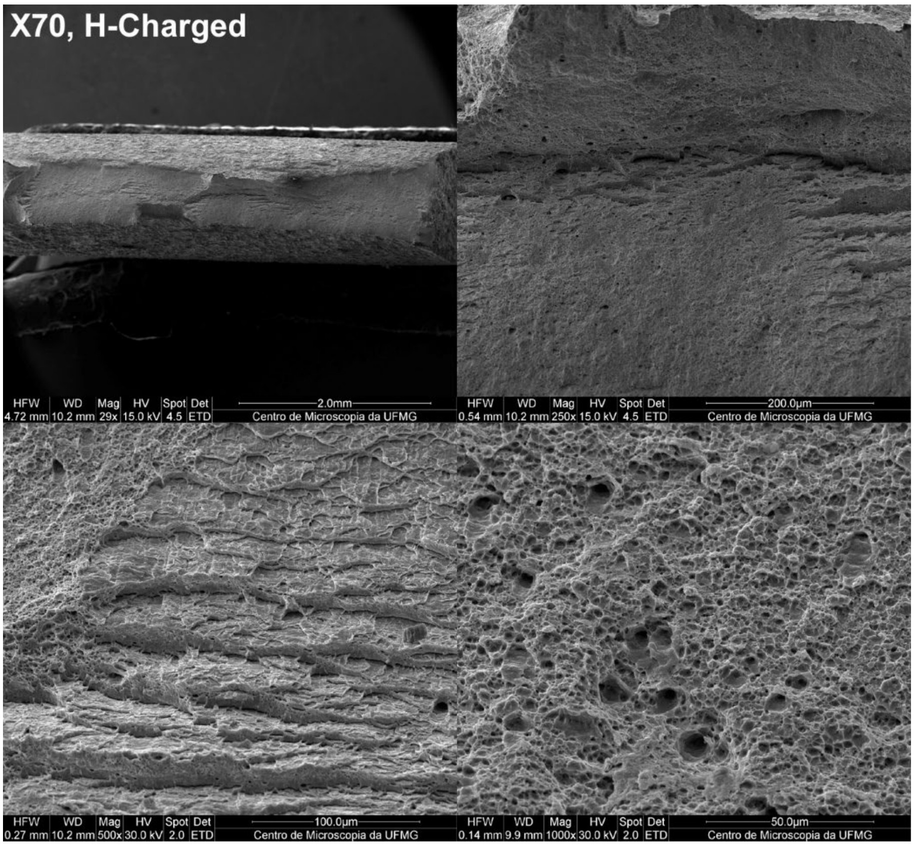

Figure 5.31 – Fracture surface of the X70 steel SSRT specimen in the hydrogen-charged condition. The test conducted on the region of the specimen corresponding to ¼ of the thickness.

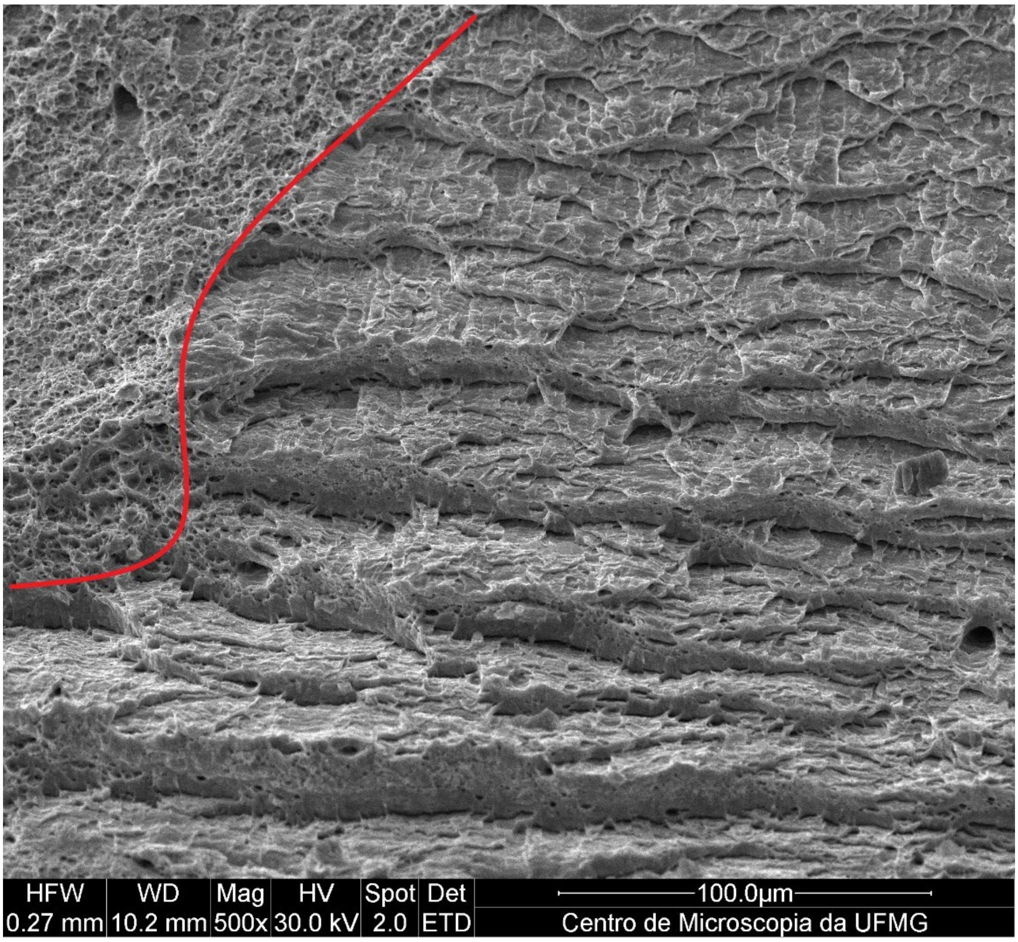

Figure 5.32 – Fracture surface of the X70 steel SSRT specimen in the hydrogen-charged condition showing ductile and brittle fracture modes. Dimples on the upper left part of the image were formed by ductile fracture, and the shear bands were result of t the brittle fracture. The test conducted on the region of the specimen corresponding to ¼ of the thickness.

6. CONCLUSION

This study investigated the through-thickness variation in hydrogen embrittlement susceptibility of three API 5L X65 pipeline steels and one API 5L X70 pipeline steel, establishing clear correlations among microstructural features, hydrogen permeation behavior, mechanical performance, and cracking susceptibility. The results obtained provide direct answers to the research objectives and offer valuable insights for the development of steels with improved resistance to hydrogen-induced degradation in aggressive service environments.

- Microstructural Characterization:

Optical and scanning electron microscopy revealed that X65-1 featured a predominantly quasi-polygonal ferrite (QPF) structure with possible acicular ferrite (AF) at mid-thickness. X65-2 exhibited a mix of polygonal ferrite (PF) and QPF, along with localized upper bainite (UB) and inclusions near mid-thickness. X65-3 showed a more homogeneous PF/QPF structure throughout. In contrast, X70 presented a granular bainite (GB) matrix, pronounced centerline segregation, and martensite-austenite (M/A) constituents at mid-thickness. These microstructural variations were essential in defining the steels' susceptibility to hydrogen embrittlement, although further analyses would be required to confirm the presence of these phases with greater certainty.

- Hydrogen Transport Behavior (D_{eff} and C_0):

Electrochemical permeation tests showed that the homogeneous ferritic microstructures of X65-2 and X65-3 provided stable hydrogen transport across the thickness, with minimal variation in effective diffusivity (D_{eff}) and apparent hydrogen solubility (C_0). In contrast, X70 exhibited a significant reduction in D_{eff} and an increase in C_0 at mid-thickness, attributed to segregation bands and the presence of hydrogen-trapping features such as M/A constituents and second-phase particles.

- Hydrogen-Induced Cracking (HIC):

Standard HIC testing and ultrasonic inspection revealed no signs of cracking in the X65 steels. However, X70 showed severe mid-thickness cracking and subsurface blistering. Cracks propagated in a stepwise manner along Mn-segregated bands, confirming that chemical segregation and hard phases (M/A) act as preferential crack initiation sites. These findings reinforce the importance of controlling compositional segregation and microstructural heterogeneity in pipeline steels.

- Mechanical Response (SSRT with and without hydrogen):

SSRT tests performed at ¼ thickness indicated minimal changes in mechanical properties for the X65 steels after hydrogen charging. A slight increase in yield strength was observed - most notably in X65-2 - suggesting possible hydrogen-induced hardening. The ultimate tensile strength (UTS) remained relatively stable across all steels. However, X70 experienced a notable reduction in total strain (ε_T), indicating higher sensitivity to embrittlement. Fractographic analysis further revealed predominantly ductile fracture surfaces in X65 specimens (both charged and uncharged), whereas the hydrogen-charged X70 specimen exhibited mixed-mode fracture with clear regions of quasi-cleavage and dimples.

- Combined Analysis

The combined analysis demonstrated that steels with homogeneous ferritic microstructures and low segregation exhibit superior resistance to hydrogen embrittlement. The three X65 variants showed more favorable performance compared to X70, especially in the mid-thickness region. These findings underscore the role of microstructure and processing in defining hydrogen embrittlement resistance and provide a solid foundation for the design of safer, more durable pipeline steels for hydrogen-containing environments

By integrating evidence from slow strain rate testing (SSRT), optical microscopy (OM), scanning electron microscopy (SEM) coupled with energy-dispersive X-ray spectroscopy (EDS), ultrasonic testing (UT), electrochemical hydrogen permeation, and hydrogen-induced cracking (HIC) per NACE TM0284, we established a coherent picture of microstructure–property–environment interactions. OM/SEM–EDS were essential to resolve and classify the steel microconstituents and their distribution. Post-TM0284 UT quantified the material's susceptibility to the nucleation and growth of hydrogen blisters, while SSRT provided a direct measure of hydrogen-embrittlement (HE) susceptibility under monotonic loading, consistent with the observed capacity for blister growth. Permeation testing yielded the effective diffusivity (D_{eff}) and lattice solubility (C_0), parameters that sensitively reflect trapping density and microstructural features (e.g., grain-boundary area, dislocation density, and MA fraction). Together, these techniques provide complementary, cross-validated indicators of both the mechanisms and the severity of HE/HIC in the studied steels.

On the basis of the combined evidence, X65-3 emerges as the preferred grade for sour-service: homogeneous microstructure throughout the section, minimal variability in electrochemical metrics, no H_2 cracking observed in HIC, and only slight SSRT deviations between charged and uncharged specimens.

7. REFERENCES

1. NEGI, A et al. Coupled analysis of hydrogen diffusion, deformation, and fracture: a review. International Journal of Hydrogen Energy, v. 82, p. 281-310, 2024. DOI: 10.1016/j.ijhydene.2024.07.348.

2. KROM, et al., A. Hydrogen transport near a blunting crack tip. Journal of the Mechanics and Physics of Solids, Oxford, v. 47, n. 4, p. 971-992, fev. 1999. DOI: 10.1016/S0022-5096(98)00064-7.

3. ORIANI, R. A. Hydrogen embrittlement of steels. *Annual Review of Materials Science*, Palo Alto, v. 8, p. 327-357, 1978. DOI: 10.1146/annurev.ms.08.080178.001551.
4. SOFRONIS, P.; McMEEKING, R. M. Numerical analysis of hydrogen transport near a blunting crack tip. *Journal of the Mechanics and Physics of Solids*, Oxford, v. 37, n. 3, p. 317-350, 1989. DOI: 10.1016/0022-5096(89)90002-1.
5. MARTIN, M. L.; SOFRONIS, P. A. Hydrogen-induced cracking and blistering in steels: a review. Journal of Natural Gas Science and Engineering, Oxford, v. 101, p. 104547, mar. 2022. DOI: 10.1016/j.jngse.2022.104547.

6. INTERNATIONAL ORGANIZATION FOR STANDARDIZATION. ISO 17081:2014 – Method of measurement of hydrogen permeation and determination of hydrogen uptake and transport in metals by an electrochemical technique. Geneva, 2014.

7. ASTM INTERNATIONAL. ASTM G148-97(2018) – Standard practice for evaluation of hydrogen uptake, permeation, and transport in metals by an electrochemical technique. West Conshohocken, 2018. DOI: 10.1520/G0148-97R18.

8. ASTM INTERNATIONAL. ASTM A370-24a: Standard test methods and definitions for mechanical testing of steel products. West Conshohocken: ASTM International, 2024.

9. LI, X et al. Review of the hydrogen embrittlement and interactions between hydrogen and microstructural interfaces in metallic alloys: grain boundary, twin boundary, and nano-precipitate. International Journal of Hydrogen Energy, v. 72, p. 74-109, 2024. DOI: 10.1016/j.ijhydene.2024.05.257.

10. KIM, K. T.; et al. Effects of microstructural inhomogeneity on HIC susceptibility and HIC evaluation methods for linepipe steels for sour service. In: INTERNATIONAL PIPELINE CONFERENCE – IPC, 10., 2014, Calgary. Proceedings… Calgary: ASME, 2014. p. 1-8. Paper IPC2014-33341.

11. NACE INTERNATIONAL. NACE TM0284:2016 – Standard test method – Evaluation of pipeline and pressure vessel steels for resistance to hydrogen-induced cracking. Houston: NACE

International, 2016.

12. AMERICAN PETROLEUM INSTITUTE. API SPEC 5L – Specification for line pipe. 46. ed. Washington, DC, 2018.

13. RAMIREZ, et al. Effects of different cooling rates on the microstructure, crystallographic features, and hydrogen induced cracking of API X80 pipeline steel. Journal of Materials Research and Technology, v. 14, p. 1848-1861, 2021. DOI: 10.1016/j.jmrt.2021.07.060.

14. SHI, L. et al. Development of ferrite/bainite bands and study of bainite transformation retardation in HSLA steel during continuous cooling. Metals and Materials International, Seoul, v. 20, n. 1, p. 19-25, jan. 2014. DOI: 10.1007/s12540-014-1006-0

15. SHABALOV, I. *et al.* Effect of Chemical Composition on the Central Segregation Heterogeneity and HIC Resistance of Rolled Plates. In: SHABALOV, I. *et al. Pipeline Steels for Sour Service*. Cham: Springer, 2019. p. 129-158. DOI: 10.1007/978-3-030-00647-1_5.

16. COLLINS, L. E. *et al.* Effects of segregation on the mechanical performance of X70 line pipe. In: INTERNATIONAL PIPELINE CONFERENCE, 11., 26-30 set. 2016, Calgary. *Proceedings…* New York: American Society of Mechanical Engineers, 2016. 7 p. Paper No. IPC2016-64302. DOI: 10.1115/IPC2016-64302.

17. IRVINE, *et al*. Grain-refined C-Mn steels. Journal of the Iron and Steel Institute, v. 205, p. 161, 1967.

18. BORATTO, F. *et al*.: Effect of chemical composition on critical temperatures of microalloyed steels. In: International Conference on Physical Metallurgy of Thermomechanical Processing of Steels and Other Metals - THERMEC '88. Proceedings. Iron and Steel Institute of Japan, Tokyo, 1988, p. 383-390.

19. BARBOSA, R. The influence of chemical composition on the critical temperatures of microalloyed steels. 1987, Warrendale: TMS-AIME, 1987

20. LOTTER, U. Aufstellung von Regressionsgleichungen zur Beschreibung des Umwandlungsverhaltens beim thermomechanischen Walzen. Technische Bericht, Thyssen Stahl, Duisburg, 1988, 136 p.

21. ZAJAC, S *et al*. Characterisation and quantification of complex bainitic microstructures in high and ultra-high strength linepipe steels. Materials Science Forum, Stafa-Zurich, v. 500-501, p. 387-394, nov. 2005. DOI: 10.4028/www.scientific.net/MSF.500-501.387.

22. KRAUSS, G. *Steels: processing, structure, and performance*. 2. ed. Materials Park, OH: ASM International, 2015.

23. COLLINS, L. E.; *et al*. Effects of segregation on the mechanical performance of X70 line pipe. In:

INTERNATIONAL PIPELINE CONFERENCE, 11., 26-30 set. 2016, Calgary. Proceedings… New York: American Society of Mechanical Engineers, 2016. Paper No. IPC2016-64302, 7 p. DOI: 10.1115/IPC2016-64302.

24. PEMOV, I. F.; NOSOCHENKO, O. V. Improving the mechanical properties of rolled plates and slabs in the thickness direction. *Metallurgist*, New York, v. 47, n. 11-12, p. 460-464, nov./dez. 2003.
25. MATROSOV, Y. I. *et al.* Influence of thermomechanical processing and heat treatment on microstructure formation and HIC resistance of pipe steel. *Problems of Ferrous Metallurgy and Materials Science*, v. 1, p. 98-104, 2014.
26. MATROSOV, Yu. *et al*. Effect of accelerated cooling parameters on microstructure and hydrogen cracking resistance of low-alloy pipe steels. *Metallurgist*, New York, v. 59, n. 1-2, p. 60-68, maio 2015. DOI: 10.1007/s11015-015-0061-1.
27. KHOLODNYI, A. A.; *et al*. Effect of carbon and manganese on low-carbon pipe steel hydrogen-induced cracking resistance. *Metallurgist*, New York, v. 60, n. 1-2, p. 54-60, maio 2016. DOI: 10.1007/s11015-016-0251-5.
28. SHABALOV, I. P. *et al. Steel for gas and oil pipelines resistant to fracture in hydrogen sulphide-containing media*. Moscow: Metallurgizdat, 2017.
29. SHI, L. et al. Development of ferrite/bainite bands and study of bainite transformation retardation in HSLA steel during continuous cooling. Metals and Materials International, v. 20, n. 1, p. 19–25, jan. 2014
30. PELLICCIONE, A. S.; SILVA, P. S. C. P. da. *Análise de falhas: trincas e fraturas em equipamentos metálicos*. Rio de Janeiro: Portal de Publicações Universidade Petrobras, 2024. ISBN 978-65-88763-27-8.
31. GANGLOFF, R. P. Hydrogen-assisted cracking. p. 31–101, 1 jan. 2003.
32. LYNCH, S. P. Environmentally assisted cracking: overview of evidence for an adsorption-induced localized-slip process. *Acta Metallurgica*, Oxford, v. 36, n. 10, p. 2639-2661, out. 1988. DOI: 10.1016/0001-6160(88)90030-1.
33. RAHIMI, S.; *et al*. Hydrogen embrittlement of pipeline steels under gaseous and electrochemical charging: a comparative review on tensile properties. *Engineering Failure Analysis*, Oxford, v. 167, part A, Art. 108956, jan. 2025. DOI: 10.1016/j.engfailanal.2024.108956.
34. DWIVEDI, S. K.; VISHWAKARMA, M. Hydrogen embrittlement in different materials: A review. International Journal of Hydrogen Energy, v. 43, n. 46, p. 21603–21616, nov. 2018
35. PFEIL, L. B. The effect of occluded hydrogen on the tensile strength of iron. *Proceedings of the Royal Society of London. Series A, Containing Papers of a Mathematical and Physical Character*, London, v. 112, n. 760, p. 182-195, ago. 1926. DOI: 10.1098/rspa.1926.0103.
36. VEHOFF, H.; NEUMANN, P. Crack propagation and cleavage initiation in Fe-2.6%-Si single crystals under controlled plastic crack tip opening rate in various gaseous environments. *Acta Metallurgica*, Oxford, v. 28, n. 3, p. 265-272, mar. 1980. DOI: 10.1016/0001-6160(80)90161-3.
37. HOAGLAND, R. G.; HEINISCH, H. L. An atomic simulation of the influence of hydrogen on the fracture behavior of nickel. *Journal of Materials Research*, v. 7, n. 8, p. 2080-2088, ago. 1992. DOI:

10.1557/JMR.1992.2080.

38. MARTIN, M. L.; *et al*. Hydrogen-induced intergranular failure in nickel revisited. *Acta Materialia*, Oxford, v. 60, n. 6-7, p. 2739-2745, abr. 2012. DOI: 10.1016/j.actamat.2012.01.040.
39. BEACHEM, C. D. A new model for hydrogen-assisted cracking (hydrogen "embrittlement"). *Metallurgical Transactions*, v. 3, n. 2, p. 441-455, fev. 1972. DOI: 10.1007/BF02642048.
40. BIRNBAUM, H. K.; SOFRONIS, P. Hydrogen-enhanced localized plasticity — a mechanism for hydrogen-related fracture. *Materials Science and Engineering: A*, Oxford, v. 176, n. 1-2, p. 191-202, mar. 1994. DOI: 10.1016/0921-5093(94)90975-X.
41. SOFRONIS, P.; BIRNBAUM, H. K. Mechanics of the hydrogen-dislocation-impurity interactions— I. Increasing shear modulus. *Journal of the Mechanics and Physics of Solids*, Oxford, v. 43, n. 1, p. 49-90, jan. 1995. DOI: 10.1016/0022-5096(94)00056-B.
42. TABATA, T.; BIRNBAUM, H. K. Direct observations of the effect of hydrogen on the behavior of dislocations in iron. *Scripta Metallurgica*, Oxford, v. 17, n. 7, p. 947-950, jul. 1983. DOI: 10.1016/0036-9748(83)90268-2.
43. SOFRONIS, P.; ROBERTSON, I. M. Transmission electron microscopy observations and micromechanical/continuum models for the effect of hydrogen on the mechanical behaviour of metals. *Philosophical Magazine A*, London, v. 82, n. 17-18, p. 3405-3413, 2002. DOI: 10.1080/01418610210138314.
44. NAGUMO, M.; NAKAMURA, M.; TAKAI, K. Hydrogen thermal desorption relevant to delayed-fracture susceptibility of high-strength steels. *Metallurgical and Materials Transactions A*, Warrendale, PA, v. 32, n. 2, p. 339-347, fev. 2001. DOI: 10.1007/s11661-001-0265-9.
45. NAGUMO, M. Hydrogen related failure of steels – a new aspect. *Materials Science and Technology*, London, v. 20, n. 8, p. 940-950, ago. 2004. DOI: 10.1179/026708304225019687.
46. KIRCHHEIM, R. Reducing grain boundary, dislocation line and vacancy formation energies by solute segregation. I. Theoretical background. *Acta Materialia*, Oxford, v. 55, n. 15, p. 5129-5138, set. 2007. DOI: 10.1016/j.actamat.2007.05.047.
47. DADFARNIA, M.; SOFRONIS, P.; NEERAJ, T. Hydrogen interaction with multiple traps: can it be used to mitigate embrittlement? *International Journal of Hydrogen Energy*, v. 36, n. 16, p. 10141-10148, ago. 2011. DOI: 10.1016/j.ijhydene.2011.05.027.
48. BIRNBAUM, H. K. Hydrogen effects on deformation and fracture: science and sociology. *MRS Bulletin*, Warrendale, v. 28, n. 7, p. 479-485, jul. 2003. DOI: 10.1557/mrs2003.143.
49. GERBERICH, W. W.; STAUFFER, D. D.; SOFRONIS, P. A coexistent view of hydrogen effects on mechanical behavior of crystals: HELP and HEDE. In: INTERNATIONAL HYDROGEN CONFERENCE – EFFECTS OF HYDROGEN ON MATERIALS, 2008, Moran, WY, EUA, 7-10 set. 2008. *Effects of hydrogen on materials: proceedings of the 2008 International Hydrogen Conference*. Org.: SOMERDAY, B.; SOFRONIS, P.; JONES, R. Materials Park, OH: ASM International, 2009. p. 38-45.
50. DJUKIC, M. B.; *et al*. The synergistic action and interplay of hydrogen embrittlement mechanisms in steels and iron: localized plasticity and decohesion. *Engineering Fracture Mechanics*, v. 216, Art.

106528, 2019. DOI: 10.1016/j.engfracmech.2019.106528.

51. BARRERA, O. *et al.* Understanding and mitigating hydrogen embrittlement of steels: a review of experimental, modelling and design progress from atomistic to continuum. *Journal of Materials Science*, Cham, v. 53, n. 9, p. 6251-6290, mai. 2018. DOI: 10.1007/s10853-017-1978-5.
52. NEERAJ, T.; SRINIVASAN, R.; LI, J. Hydrogen embrittlement of ferritic steels: observations on deformation microstructure, nanoscale dimples and failure by nanovoiding. *Acta Materialia*, Oxford, v. 60, n. 13-14, p. 5160-5171, ago. 2012. DOI: 10.1016/j.actamat.2012.05.006.
53. NEGI, A.; *et al.* Coupled analysis of hydrogen diffusion, deformation, and fracture: a review. International Journal of Hydrogen Energy, Oxford, v. 82, n. 3, p. 281-310, 2024. DOI: 10.1016/j.ijhydene.2024.07.348
54. TROIANO, A. R.; HEHEMANN, R. F. A Basic Study of Ferrous Materials for Desalination Equipment. 1970
55. VANDEWALLE, L.; DEPOVER, T.; VERBEKEN, K. Current state-of-the-art of hydrogen trapping by carbides: from theory to experiment. *International Journal of Hydrogen Energy*, Oxford, v. 136, p. 888-901, jun. 2025. DOI: 10.1016/j.ijhydene.2024.03.266.
56. SHEWMON, Paul. *Diffusion in solids*. 2. ed. Cham: Springer, 2016. (The Minerals, Metals & Materials Series). DOI: 10.1007/978-3-319-48206-4.
57. DIETER, G. E. Mechanical metallurgy. 3. ed. Beijing: Tsinghua University Press, 2006. 700 p. ISBN 978-7302141891.
58. HIRTH, J. P. Effects of hydrogen on the properties of iron and steel. *Metallurgical Transactions A*, v. 11, n. 6, p. 861-890, jun. 1980. DOI: 10.1007/BF02654700.
59. CHEN, Y.-S *et al.* Hydrogen trapping and embrittlement in metals – A review. *International Journal of Hydrogen Energy*, Oxford, v. 136, n. 7, p. 789-821, 2025. DOI: 10.1016/j.ijhydene.2024.04.076.
60. SHI, R. et al. Atomic-scale investigation of deep hydrogen trapping in NbC/α-Fe semi-coherent interfaces. Acta Materialia, v. 200, p. 686–698, 1 nov. 2020.
61. Petroleum and Natural Gas Industries — Materials for use in H2S-containing environments in oil and gas production. Standard, International Organization for Standardization, Geneva, CH, 2020
62. ELBOUJDAINI, M.; REVIE, R. W. Metallurgical factors in stress corrosion cracking (SCC) and hydrogen-induced cracking (HIC). Journal of Solid State Electrochemistry, v. 13, n. 7, p. 1091–1099, 25 mar. 2009.
63. KROM, A. H. M.; BAKKER, A.; KOERS, R. W. J. Modelling hydrogen-induced cracking in steel using a coupled diffusion stress finite element analysis. International Journal of Pressure Vessels and Piping, v. 72, n. 2, p. 139–147, 1 jul. 1997.
64. OSSAI, C. I.; BOSWELL, B.; DAVIES, I. J. Pipeline failures in corrosiveenvironments – A conceptual analysis of trends and effects. Engineering Failure Analysis, v. 53, p. 36–58, jul. 2015.
65. VENEGAS, V. et al. On the role of crystallographic texture in mitigating hydrogen-induced cracking in pipeline steels. Corrosion Science, v. 53, n. 12, p. 4204–4212, dez. 2011.
66. MOSTAFIJUR RAHMAN, K. M. et al. Effect of electrochemical hydrogen charging on an API X70 pipeline steel with focus on characterization of inclusions. International Journal of Pressure Vessels

and Piping, v. 173, n. Complete, p.147–155, 2019.

67. SHI, X.; YAN, W.; WANG, W.; SHAN, Y.; YANG, K.
Novel Cu-bearing high-strength pipeline steels with excellent resistance to hydrogen-induced crackin g. *Materials & Design*, Oxford, v. 92, p. 300-305, fev. 2016. DOI: 10.1016/j.matdes.2015.12.029
68. BEIDOKHTI, B.; KOUKABI, A. H.; DOLATI, A. Influences of titanium and manganese on high strength low alloy SAW weld metal properties. *Materials Characterization*, Oxford, v. 60, n. 3, p. 225-233, mar. 2009. DOI: 10.1016/j.matchar.2008.09.005.
69. BEIDOKHTI, B.; DOLATI, A.; KOUKABI, A. H. Effects of alloying elements and microstructure on the susceptibility of the welded HSLA steel to hydrogen-induced cracking and sulfide stress cracking. Materials Science and Engineering: A, Oxford, v. 507, n. 1-2, p. 167-173, mai. 2009. DOI: 10.1016/j.msea.2008.11.064.
70. HEJAZI, D. *et al.*; PERELOMA, E. V. Effect of manganese content and microstructure on the susceptibility of X70 pipeline steel to hydrogen cracking. *Materials Science and Engineering: A*, Oxford, v. 551, p. 40-49, 15 ago. 2012. DOI: 10.1016/j.msea.2012.04.076.
71. MOON, J.; PARK, C.; KIM, S. J. Influence of Ti addition on the hydrogen induced cracking of API 5L X70 hot-rolled pipeline steel in acid sour media. *Metals and Materials International*, Seoul, v. 18, n. 4, p. 613-617, ago. 2012. DOI: 10.1007/s12540-012-4007-x.
72. SINGH, V.; *et al.* Hydrogen induced blister cracking and mechanical failure in X65 pipeline steels. *International Journal of Hydrogen Energy*, Oxford, v. 44, n. 39, p. 22039-22049, **ago. 2019**. DOI: 10.1016/j.ijhydene.2019.06.098.
73. ZHANG, P.; LALEH, M.; HUGHES, A. E.; et al. A systematic study on the influence of electrochemical charging conditions on the hydrogen embrittlement behaviour of a pipeline steel. International Journal of Hydrogen Energy, Oxford, v. 48, n. 43, p. 16501-16516, mai. 2023. DOI: 10.1016/j.ijhydene.2023.01.149.
74. RAHIMI, S.; *et al.* Hydrogen embrittlement of pipeline steels under gaseous and electrochemical charging: a comparative review on tensile properties. Engineering Failure Analysis, Oxford, v. 167, part A, Art. 108956, jan. 2025. DOI: 10.1016/j.engfailanal.2024.108956.
75. DEPOVER, T.; LAUREYS, A.; PEREZ ESCOBAR, D. M.; et al. Understanding the interaction between a steel microstructure and hydrogen. Materials, Basel, v. 11, n. 5, Art. 698, abr. 2018. DOI: 10.3390/ma11050698.
76. DEVANATHAN, M. A. V.; STACHURSKI, Z. The adsorption and diffusion of electrolytic hydrogen in palladium. *Proceedings of the Royal Society of London. Series A, Mathematical and Physical Sciences*, London, v. 270, n. 1340, p. 90-102, out. 1962. DOI: 10.1098/rspa.1962.0205.
77. ZHENG, S.; QIN, Y.; LI, W.; *et al.* Effect of hydrogen traps on hydrogen permeation in X80 pipeline steel — a joint experimental and modelling study. *International Journal of Hydrogen Energy*, Oxford, v. 48, n. 12, p. 4773-4788, 8 fev. 2023. DOI: 10.1016/j.ijhydene.2022.10.038.
78. ZHAO, H.; PALMIERE, E. J. Influence of cooling rate on the grain-refining effect of austenite deformation in a HSLA steel. *Materials Characterization*, Oxford, v. 158, Art. 109990, nov. 2019. DOI: 10.1016/j.matchar.2019.109990.

79. LIESSEM, A. *et al*. Concepts and production results of heavy wall linepipe in grades up to X70 for sour service. In: INTERNATIONAL PIPELINE CONFERENCE (IPC), 4., 29 set.–3 out. 2002, Calgary, AB, Canadá. *Proceedings*... New York: American Society of Mechanical Engineers, 2002. Paper No. IPC2002-27139, p. 1651-1658. DOI: 10.1115/IPC2002-27139.
80. BHADESHIA, H. K. D. H. *Bainite in steels*. 2. ed. London: The Institute of Materials, 2001.
81. SHIM, D. H. *et al*. Increased resistance to hydrogen embrittlement in high-strength steels composed of granular bainite. *Materials Science and Engineering: A*, Oxford, v. 700, p. 473-480, jun. 2017. DOI: 10.1016/j.msea.2017.06.043.
82. COTA, A. B.; SANTOS, D. B. Microstructural characterization of bainitic steel submitted to torsion testing and interrupted accelerated cooling. *Materials Characterization*, Oxford, v. 44, n. 3, p. 291-299, mar. 2000. DOI: 10.1016/S1044-5803(99)00060-1.
83. MOHTADI-BONAB, M. A.; SZPUNAR, J. A.; RAZAVI-TOUSI, S. S. Hydrogen induced cracking susceptibility in different layers of a hot rolled X70 pipeline steel. *International Journal of Hydrogen Energy*, Kidlington, v. 38, n. 25, p. 13831-13841, ago. 2013. DOI: 10.1016/j.ijhydene.2013.08.046.
84. MOHTADI-BONAB, M. A. *et al. The mechanism of failure by hydrogen induced cracking in an acidic environment for API 5L X70 pipeline steel*. International Journal of Hydrogen Energy, Oxford, v. 40, n. 2, p. 1096-1107, jan. 2015. DOI: 10.1016/j.ijhydene.2014.11.057.